Technische Universität München

Max-Planck-Institut für extraterrestrische Physik

Design and Application of an Optical High Time Resolution Instrument for High-Energy Transients

Alexander R. Stefanescu

Vollständiger Abdruck der von der Fakultät für Physik der Technischen Universität München zur Erlangung des akademischen Grades eines

Doktors der Naturwissenschaften (Dr. rer. nat.)

genehmigten Dissertation.

Vorsitzender:		Univ.-Prof. Dr. A.J. Buras
Prüfer der Dissertation:	1.	Priv.-Doz. Dr. J. Greiner
	2.	Univ.-Prof. Dr. L. Oberauer

Die Dissertation wurde am 19.09.2011 bei der Technischen Universität München eingereicht und durch die Fakultät für Physik am 08.12.2011 angenommen.

Physik-Department

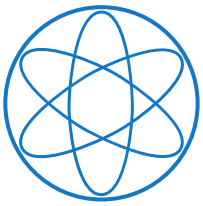

Design and Application of an Optical High Time Resolution Instrument for High-Energy Transients

Dissertation von

Alexander R. Stefanescu

Technische Universität
München

Max-Planck-Institut für
extraterrestrische Physik

Abstract

The processes around compact objects like black holes, neutron stars and white dwarfs frequently result in strong variability on very short timescales, making high time resolution a very important aspect in the study of compact objects. As the emission processes probed by the optical differ from the high-energy bands most often employed in studies of compact objects, optical and high-energy observations complement each other and allow a much more complete picture when used in conjunction. In many classes of compact objects, the activity is highly unpredictable, with long quiescent periods between outbursts, or even with very bright and sudden outbursts that do not recur due to the destruction of the compact object itself. The most extreme example of unpredictable and very strong outbursts are probably γ-ray bursts, which are the most energetic explosions in the observable universe and result in the complete destruction of their progenitor stars.

In the past, the unpredictable occurrence and short duration of γ-ray bursts and similar transients has precluded any successful optical high time resolution observations of their afterglows. In this thesis, I present an instrument specifically designed for the optical observation of high-energy transients with high time resolution. I have developed OPTIMA-Burst, an optical high time resolution photo-polarimeter that automatically reacts to high-energy transients reported by satellite observatories. Using OPTIMA-Burst, I have performed several long-duration observation campaigns in which OPTIMA-Burst had full automatic interrupt rights over the 1.3 m telescope of the Skinakas Observatory and successfully reacted to numerous triggers. The highlight of the OPTIMA-Burst campaigns was the discovery of SWIFT J195509.6+261406, an unknown class of galactic X-ray transient, with unprecedented large amplitude and fast optical variability. The morphology of the variability as well as the low-significance detection of matching periodicity in the optical and in the X-rays have led to the speculation that SWIFT J1955 may be a magnetar showing outbursts in the optical instead of in the X-rays.

Zusammenfassung

Vorgänge in der Umgebung kompakter Objekte wie schwarzer Löcher, Neutronensterne und weißer Zwerge gehen häufig mit starker Variabilität auf sehr kurzen Zeitskalen einher, was hohe Zeitauflösung zu einem wichtigen Aspekt bei der Beobachtung kompakter Objekte macht. Da im optischen andere Emissionsprozesse untersucht werden können als in den Hochenergiebändern, die meist bei der Beobachtung kompakter Objekte eingesetzt werden, ergänzen sich optische Beobachtungen und Beobachtungen bei hohen Energien zu einem vervollständigtem Bild. Die Aktivität vieler Klassen kompakter Objekte ist kaum vorherzusagen. So haben viele Objekte sehr lange ruhige Zeiträume zwischen Ausbrüchen, oder zeigen sogar starke und plötzliche Ausbrüche die das zugrunde liegende Objekt vollständig zerstören, und daher nicht wiederkehren. Das extremste Beispiel für diese Art von Ausbrüchen sind wahrscheinlich γ-Strahlen Ausbrüche, die stärksten Explosionen im beobachtbaren Universum, in denen der aufleuchtende Stern vollständig zerstört wird.

Bislang hat die Unvorhersagbarkeit und kurze Dauer von γ-Strahlen Ausbrüchen eine erfolgreiche optische Beobachtung ihres Nachleuchtens mit hoher Zeitauflösung verhindert. In der vorliegenden Arbeit stelle ich ein Instrument vor, das speziell dafür entworfen wurde, Hochenergietransienten mit hoher Zeitauflösung im Optischen zu beobachten. Hierzu habe ich OPTIMA-Burst entwickelt, ein optisches Photo-Polarimeter mit hoher Zeitauflösung, das automatisch auf Hochenergietransienten reagiert, die von Satellitenobservatorien gemeldet werden. Ich habe mehrere Langzeit-Kampagnen am 1.3 m Teleskop der Skinakas-Sternwarte durchgeführt, in denen OPTIMA-Burst die vielfach genutzte Berechtigung hatte, jederzeit den laufenden Beobachtungsbetrieb zu unterbrechen und autonom die Beobachtung von Transienten zu beginnen. Die Herausragendste Beobachtung, die mit OPTIMA-Burst gelang, war die Entdeckung von SWIFT J195509.6+261406, einem galaktischen Röntgentransienten einer bislang unbekannten Klasse mit außerordentlich starker und schneller optischer Variabilität. Die Morphologie der Variabilität und die Entdeckung einer Periode niedriger Signifikanz aber übereinstimmender Frequenz im Optischen und im Röntgen-Licht, hat zu der Spekulation geführt, SWIFT J1955 könnte ein Magnetar sein, der anstatt im Röntgenbereich Ausbrüche im Optischen zeigt.

Contents

1. Introduction **1**
- 1.1. Early Time-Domain Astronomy . . . 2
- 1.2. Early High Time Resolution Astronomy . . . 2
- 1.3. Current High Time Resolution Astronomy . . . 3
- 1.4. Transient Astronomy . . . 4
- 1.5. An optical HTRA-Transient observatory . . . 6

2. OPTIMA **8**
- 2.1. Telescope . . . 9
- 2.2. Focal Assembly . . . 10
  - 2.2.1. Guider Acquisition Module . . . 10
  - 2.2.2. Field-View Unit . . . 11
  - 2.2.3. Twin Wollaston Polarimeter . . . 13
- 2.3. Detector Unit . . . 17
  - 2.3.1. Fibres . . . 17
  - 2.3.2. APDs . . . 19
- 2.4. Time Base . . . 22
- 2.5. Data Acquisition . . . 24
  - 2.5.1. The Classic OPTIMA DAQ System . . . 24
  - 2.5.2. The Next-Generation OPTIMA DAQ System . . . 28

3. The OPTIMA-Burst Instrument **32**
- 3.1. Telescope Control . . . 32
  - 3.1.1. Skinakas Observatory TCS . . . 33
  - 3.1.2. TCS Connection . . . 33
  - 3.1.3. Tertiary Mirror Control . . . 34
  - 3.1.4. Fine Control . . . 35
  - 3.1.5. Pointing . . . 36
  - 3.1.6. Guiding . . . 37
  - 3.1.7. OPTIMA-Burst Control Center . . . 38
- 3.2. GRB Response Automation . . . 39
  - 3.2.1. GCN Connection . . . 40
  - 3.2.2. Transient Detection . . . 42

4. OPTIMA Data Analysis **43**
- 4.1. Adaptive Data Binning . . . 44
- 4.2. Upper Limits . . . 47
- 4.3. Pile-up Correction . . . 50
  - 4.3.1. Poisson Distribution . . . 51
  - 4.3.2. Pile-up Distribution . . . 52
  - 4.3.3. Discussion . . . 54
- 4.4. Nonlinear Detector Response . . . 56

4.5. Polarimetry Analysis . . . 57
4.5.1. Stokes Parameters . . . 57
4.5.2. Determining the Stokes Parameters . . . 58
4.5.3. The Sparks and Axon Method for N Polarizers . . . 58

5. The OPTIMA-Burst Campaign **61**
5.1. γ-ray Bursts . . . 61
5.2. Successful Observations . . . 62
5.2.1. GRB 070610 a.k.a. SWIFT J195509.6+261406 . . . 63
5.2.2. GRB 090726 . . . 63
5.2.3. GRB 060904B . . . 68
5.2.4. GRB 060926 . . . 69
5.3. Successful Trigger Reactions with Non-Detection . . . 69
5.3.1. GRB 081102 . . . 70
5.3.2. GRB 090621B . . . 71
5.3.3. GRB 090628 . . . 71
5.3.4. GRB 090727 . . . 72
5.3.5. Upper Limit Astrophysical Context . . . 72
5.4. Unsuccessful Triggers . . . 73
5.4.1. GRB 060901 . . . 74
5.4.2. GRB 070724B . . . 74
5.4.3. GRB 081028 . . . 75
5.4.4. GRB 090715B . . . 75

6. Observations of SWIFT J195509.6+261406 **76**
6.1. Discovery . . . 76
6.2. X-ray Analysis and Distance Estimates . . . 77
6.3. Optical Light-Curves . . . 80
6.4. Flux Calibration . . . 80
6.5. Analysis of Individual Flares . . . 83
6.6. Frequency-Domain Analysis . . . 84
6.7. Statistical Analysis . . . 86
6.8. Astrophysical Interpretation . . . 87
6.8.1. Excluding Several Scenarios . . . 87
6.8.2. The J1955 −SGR 1900+14 Connection . . . 88
6.8.3. Magnetars . . . 89
6.8.4. Is J1955 a Magnetar? . . . 90

7. Conclusions **92**
7.1. OPTIMA-Burst Retrospection . . . 92
7.2. The Way Forward . . . 93

A. Table of Individually Fitted Flares of SWIFT J195509.6+261406 **95**

1. Introduction

Bright Star! Would I were steadfast as thou art–
Not in lone splendour hung aloft the night
And watching, with eternal lids apart
Like Nature's patient, sleepless Eremite
The moving waters at their priest-like task
Of pure ablution round Earth's human shores
Or gazing on the new soft fallen mask
Of snow upon the mountains and the moors –

No - yet still steadfast, still unchangeable
Pillowed upon my fair love's ripening breast
To feel for ever its soft fall and swell
Awake for ever in a sweet unrest
Still, still to hear her tender-taken breath
Half-passionless, and so swoon on to death.

John Keats

When lying on the grass during a summer night the stars appear to the star-gazer as stately, unperturbed and eternal. Every night they follow the same path across the sky, every year at the same time they appear at the same location. Of course not quite all stars are *fixed stars*, some of them being in motion with respect to all the rest of the stars like wanderers. These wandering stars, or *planets* from the greek πλανήτης αστήρ (planētēs astēr), "wandering star", seem to be the sole exception in an unchanging night sky.

However, on closer inspection this static image is not actually true. Besides the diurnal and seasonal cycles, and the movement of the planets and their moons, the night sky is indeed constantly full of change. The easiest to observe stellar object that keeps changing is not actually an object of the night sky, but the Sun. The surface of the Sun is mottled with dark spots that can be observed with small telescopes or sometimes even with the naked eye.[1] When observed for several days, the movement of the sunspots across the face of the solar disc is evidence of the rotation of the Sun. Observing sunspots for many years and counting their numbers on the Sun, it quickly becomes apparent that the number of sunspots is not constant but changing periodically, with a maximum appearing every 11 years.

During a solar eclipse, or using more specialized telescope equipment like a coronagraph and/or H_α filters, variable structures on the surface of the Sun can be observed that change on much shorter timescales. Solar prominences and solar flares can erupt on timescales of only minutes, showing that the Sun, which can seem unchanging and benign to the casual observer, is actually a star with strong activity on short timescales.

[1] Care needs to be taken to limit the amount of radiation entering the eye: Never look into the Sun without protection!

1.1. Early Time-Domain Astronomy

Movement of objects and intrinsic changes in the properties of objects not only produce variability on various time-scales in the solar system, but also in objects at much larger distances. The appearance of a new fixed star in the sky as *stella nova* has been recorded as far back as 185 AD by Chinese astronomers,[2] and some fixed stars have been at least suspected of variability since antiquity. Algol (β Per), an eclipsing binary that dips in brightness by a noticeable 1.3 magnitudes every 2.8 days during its 10-hour eclipse, is named after the arabic *ra's al-ghūl*, (literally "head of the ghoul") and is also called *Demon Star* in English. In antiquity, it was associated with the severed head of the gorgon Medusa held in triumph by Perseus, and was considered the most dangerous and unfortunate star by ancient and medieval astrologers [Burnham, 1978]. These connotations with evil and the unnatural may indicate that Algol's peculiar variability was already known in antiquity, but this speculation, while plausible, is not proven by conclusive evidence [Davis, 1957]. The first documented mention of Algol's variability was not until the Italian astronomer Geminiano Montanari of Bologna reported it in 1667 [Montanari, 1671].

In 1782 John Goodricke was the first to establish the periodicity of Algol's variability, and also proposed periodic eclipses of the star by a dark companion as a possible mechanism [Goodricke, 1784]. This was shown to be the correct mechanism using timed spectroscopic observations by Hermann C. Vogel in 1889 [Vogel, 1890]: the spectral lines in Algol's light are red- and blue shifted in phase with the variability, and the minimum of the light-curve coincides with a phase of zero shift of the spectroscopic lines. The discovery and subsequent explanation of the mechanism of Algol's variability can probably be considered the first example for the use of time-domain astronomy to derive new astrophysical insights.

Spurred by the success of his Algol observations, Goodricke continued his observations of variable stars and discovered the variability of δ Cep, now the namesake of the *Cepheid* class of variable stars. He established the variability of δ Cep to be periodic with a periodicity of $5^d8^h45^m$, within 2 minutes of the modern value [Goodricke and Bayer, 1786]. Unlike Algol, δ Cep varies in brightness not because something *moves*, but rather because it intrinsically *changes*; the entire star pulsates, changing both temperature and radius which results in an overall change in brightness.

More than a hundred years later, the period-brightness relation of Cepheids, discovered by Henrietta Swan Leavitt in 1912 [Leavitt and Pickering, 1912], became instrumental when Edwin Hubble discovered that the universe is much larger than the Milky Way [Hubble, 1925], marking Cepheid observation as one of the high points of early time-domain astronomy.

1.2. Early High Time Resolution Astronomy

Astronomy prior to 1910 was performed either by visual observation, or by photographic plates. The introduction of photographic plates as detectors in telescopes had revolutionized astronomy, as it for the first time made possible exposure times longer than that of the human eye, thereby allowing much deeper observations of faint objects. On the other hand, as they also *required* long exposure times to achieve usable sensitivity, time-domain

[2] Early historic Supernovae comprise SN 185 observed by Chinese astronomers, the SNe 1006 and 1054 (which gave rise to the Crab Nebula and Pulsar) that were observed by Chinese and Islamic astronomers, Tycho Brahe's SN 1572 and Johannes Kepler's SN 1604.

astronomy was limited to time resolution measured in hours, or to very bright objects. Astronomy on time resolutions of minutes, seconds, or even faster, also called high-time resolution astronomy (HTRA), has since the early days been driven by developments in instrumentation and detector technology.

In 1910, Joel Stebbins pioneered the use of electric solid-state detectors in HTRA by measuring the light-curve of Algol to unprecedented accuracy using a Selenium cell [Stebbins, 1910]. The advantage of the Selenium cell, which was very difficult to operate reliably, was that it combined objectively measured photometry better than that possible with photographic plates, with good time-resolution (Stebbins used 10 s integrations, binned to about 30 minutes resolution) at almost the same level achievable with the naked eye. By the late 1950s, the finicky Selenium cells had matured into photo-multipliers, robust pieces of standard equipment that were often used for their linear response and the ease of comparing photometric measurements between observations. Their great potential for HTRA was however only tapped in the late 1960s.

In July 1967, Jocelyn Bell and Antony Hewish unexpectedly discovered a pulsating radio source while investigating interstellar scintillation of quasars. Initially baffled by the properties of the source, clearly extrasolar but intragalactic, and showing *very* regular oscillations, they termed the source LGM-1 for "Little Green Man 1". They soon discovered several other similar sources, recognized the similarities of their newly discovered class of object with properties expected for Neutron Stars or White Dwarfs, and published a landmark paper in 1968 [Hewish et al., 1968].

The discovery of pulsars triggered a gold-rush of observations and discoveries. Later in 1968, a radio pulsar was discovered in the Crab Nebula, a supernova-remnant from the supernova observed by Chinese astronomers in AD 1054 [Staelin and Reifenstein, 1968]. Several groups had recognized the suitability of photoelectric detectors to identify optical counterparts to the radio-pulsars, and started systematic observation campaigns. Within days of each other, the groups around John Cocke and Ed Nather detected a strong pulsating optical source in the Crab nebula in January 1969 [Cocke et al., 1969, Nather et al., 1969]. The period of the optical source, roughly 33 ms, was compatible with the published radio period; the Crab pulsar was found in the optical. Optical observations with high time resolution in the coming years and decades allowed insights into pulsar physics not possible with other techniques: the optical band probes different radiation mechanism than the radio bands, and several observation techniques like polarimetry and spectroscopy are only possible or much easier in the optical compared to high-energy observations [Słowikowska et al., 2009].

1.3. Current High Time Resolution Astronomy

When CCD[3] technology was introduced into astronomy in the mid-1970s, it combined good linearity, high quantum efficiency, low read-noise, the potential for long integration times and imaging capabilities into a detector that was cheap to build and easy to operate. Coming closer to the ideal detector than any technology before, the CCD soon replaced photographic plates and photoelectric cells for all but fringe applications.

At the same time, it became clear in the first years after their discovery, that most pulsars were not detectable in the optical, let alone showing variability on short time scales. While some imaging detector technologies especially in the IR[4] had sub-second

[3]Charge-Coupled Device
[4]Infra-Red

read-out capability, the mainstream of the new CCD technology was not well suited for HTRA due to their relatively long read-out times, so interest in HTRA waned and it became an obscure field for several decades. In the last ten to fifteen years, however, new detector developments like frame-store CCDs, electron-multiplying CCDs and APDs[5] have made HTRA detectors with very good performance accessible, and have re-kindled interest in HTRA. Table 1.1 gives an overview over some current HTRA instruments. Today, detection of variability on short time-scales during the observation of compact sources (white dwarfs, neutron stars and black holes) is routine in the X-rays, where many compact sources are very bright. Optical high time resolution observations of these systems probe different emission mechanisms and different regions than X-ray observations, and are therefore an interesting complementary technique.

Many compact objects that are of interest to HTRA observations can be found in binary systems e.g. low and high mass X-ray binaries or cataclysmic variables. The reason for this is that the interaction between a compact object and its companion can become the source of radiation via many different mechanisms. Matter from the companion can flow over to the compact object, forming a hot accretion disk in the process. Matter flowing to the compact object can be caught in strong magnetic fields and flow along the field-lines. Matter impacting on a compact object[6] can generate hot-spots on the surface of the compact object. Matter accreting onto the compact object can accumulate, and ignite in localized thermonuclear explosions – or even create global explosions that completely destroy the compact object. As the systems involved in all these processes are quite small, the orbital timescales of the systems are relatively short, ranging from minutes to days for the companions, and down to sub-second for the inner edges of accretion discs. The emitting regions can be quite small, resulting in light-crossing time-scales down to few milliseconds.

1.4. Transient Astronomy

The processes creating variability on short time-scales in the vicinity of compact objects can create very energetic outbreaks, or transients (from Latin *transire* "to go over, to pass"). During these outbreaks, activity in all energy bands is heightened, making the times of outbreak very interesting for multi-wavelength observations. One interesting example for correlated high time resolution studies of the optical and X-ray emissions of compact objects during a period of outburst are observations of the black-hole candidate XTE J1118+480 (also called KV UMa) done by OPTIMA[7] in the optical and RXTE[8] in the X-ray band in 2000.

XTE J1118+480 is an X-ray transient discovered with the ASM[9] instrument aboard RXTE in January 2000 [Remillard et al., 2000], which was undergoing an unusually long outburst from January until July 2000. Its location far outside the galactic plane and at a distance of only 2 kpc [Wagner et al., 2001, McClintock et al., 2001] result a bright source with low foreground extinction. The compact object has a K-star companion, and its mass function[10] of 6 $M_\odot$ makes it a likely black hole candidate.

[5] Avalanche Photo-Diodes

[6] This implies the compact object is a neutron star or a white dwarf – black holes do not have a surface where matter can impact.

[7] Optical Pulsar Timing Analyzer

[8] Rossi X-ray Timing Explorer

[9] All-Sky Monitor

[10] The mass function $f(m_1, m_2) = \frac{(m_2 \sin i)^3}{(m_1+m_2)^2}$ can be deduced from the orbital motion of a binary system

Instrument	dT	Detector	Note	Reference
OPTIMA	4 µs	SPAD	Focus of this work	[Straubmeier et al., 2001] [Kanbach et al., 2003] [Stefanescu et al., 2008a]
UltraCam	5 ms	CCD	Very successful, frequent guest instrument at VLT and WHT	[Dhillon et al., 2007]
UltraSpec	1 ms	emCCD	Spectrometer version of UltraCam	[Dhillon et al., 2007]
GASP	ms ns	emCCD SPAD	Full-stokes Polarimeter, various detectors	[Kyne et al., 2010]
Iqueye	100 ps	SPAD	Precursor to ELT class instrumentation	[Barbieri et al., 2009]
S-Cam	ns	STJ	Intrinsic energy resolution $E/\Delta E \sim 5$	[Verhoeve et al., 2006]
-	ns	TES	Intrinsic energy resolution $E/\Delta E \sim 15$	[Bay et al., 2006]

Table 1.1.: Overview over some current HTRA instruments. Various older PMT and MAMA based instruments are not included.

Due to the very long duration of the outburst, it was possible to mount an OPTIMA (see Chapter 2) campaign and receive target of opportunity observation time on RXTE for a coordinated X-ray / optical observation campaign. Four consecutive nights in July 2000 resulted in a total of 2.5 hours of simultaneous observations. The results from these observations were quite unexpected: previous cross-correlation studies had either shown clear indication of optical reprocessing of X-rays, e.g. in the case of GRO J1655-40 [Hynes et al., 1998], or a negative "pre-cognition dip" in the X-ray/optical cross-correlation, as seen e.g. in GX 339-4 [Motch et al., 1983]. In XTE J1118+480, both effects were seen at the same time [Kanbach et al., 2001, Spruit and Kanbach, 2002].

X-ray photons being re-processed to optical photons is a very natural scenario in an accreting binary system: X-rays generated in the central region near the compact object illuminate the inner regions of the accretion disc. This deposition of energy raises the temperature of the accretion disc, resulting in an increase of the optical and infrared brightness. Light-delay across the accretion disc creates a positive lag of the optical with respect to the X-rays, just as can be seen at positive lags in Fig. 1.1(b). However, in this scenario the variability of the optical light-curve will be smeared out due to different light-delays to different regions of the accretion disc, implying a broadened optical auto-correlation in comparison to the X-ray autocorrelation. As can be seen in Fig. 1.1(a), this is in clear contrast to the observation in XTE J1118+480.

The "pre-cognition dip" does not result from a very obvious scenario like re-processing. In principle, it could stem from a change in the accretion flow prior to an X-ray event, e.g. when the increase in mass flow (which results in an increase in the X-rays) starts a considerable distance from the black hole. Other possible models interpret the optical radiation as cyclo-synchrotron emission in a strong magnetic field [Fabian et al., 1982].

and can be interpreted as minimum mass of the primary if the system is seen edge-on ($i = \pi/2$), and the secondary mass is negligible. It has the unit of mass and is not to be confused with statistical mass distributions of similar names, e.g. the Initial Mass Function IMF.

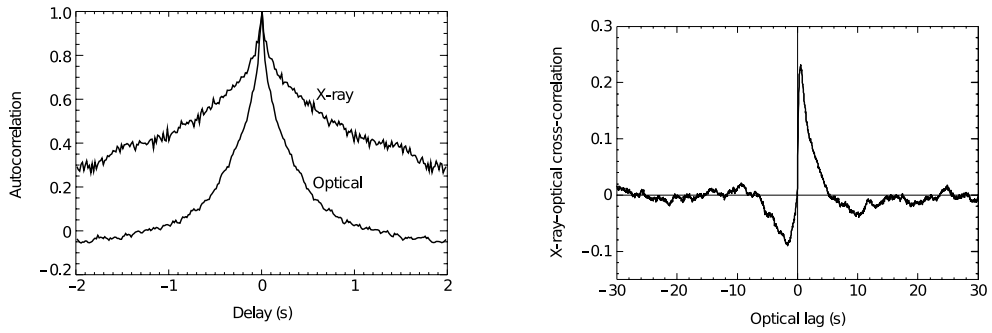

(a) (b)

Figure 1.1.: X-ray/optical auto- (a) and cross-correlation (b) from coordinated observations of an outburst of XTE J1118+480 in 2000. Interesting and unexpected features include the optical auto-correlation being much narrower than the X-ray auto-correlation, and the simultaneous appearance of a negative "precognition" peaking at around -2 s lag before a strong positive correlation at positive times. [Kanbach et al., 2001]

However no models were able to satisfactorily explain all observational facts in the 2000 OPTIMA/ RXTE campaign, making this a very exciting observation.

1.5. An optical HTRA-Transient observatory

The simultaneous optical and X-ray observation of the outburst of XTE J1118+480 in the year 2000 was only possible because the duration of the outburst was unusually long. The next outburst of the source in 2005 lasted only for little more than one month, not leaving enough time to mount an optical campaign with a high-time-resolution photometer like OPTIMA. Many interesting sources undergo very frequent outbursts and can thus be observed in a "monitor" campaign, and other sources are interesting also in quiescence. However the processes for which optical HTRA has the most discovery potential are highly energetic processes very close around compact objects and result in relatively infrequent and sudden outbursts. Here, very large changes of brightness across a wide band of energy are to be expected on very short timescales, making optical HTRA in combination with X-ray observations the ideal diagnostic tool. Of course, the occurrence of such transients cannot usually be predicted.

This is especially true for energetic transients that are formed in a cataclysmic event, and thus light up only a single time. In some of this type of transients, e.g. most supernovae, the transient is observable for relatively long periods (weeks to months), but for many the window for HTRA observations can be very short, of the order of only hours to days.

The prime example for this are γ-ray bursts (GRBs), which are amongst the most energetic events known in the universe with energy releases of 10^{51} erg. GRBs occur isotropically distributed in the sky at (mostly) cosmological distances, with redshifts of up to $z \sim 9.4$ [Cucchiara et al., 2011]. They[11] are thought to be explosions of rapidly rotating massive stars collapsing into black holes, which result in a highly relativistic jet that is viewed directly along the jet axis. As their central engine is very compact, they have

[11]Specifically the sub-class of long GRBs

prompt γ-ray light-curves with strong variability on very short time-scales. The massive amount of energy deposited in a very small volume creates a relativistically expanding fireball, which ploughs through the surrounding medium, and also creates variability on many time-scales.

As interest in GRBs in the last decade was very intense, many satellite missions provide a steady stream of GRB triggers, making GRBs an excellent target for optical HTRA transient studies. While successful simultaneous high-energy and optical observations of energetic transients were performed for some GRBs very early after the initial event [Akerlof et al., 2000, Vestrand et al., 2005, Racusin et al., 2008], no observations with quick reaction time and high time resolution in the optical were ever successfully attempted. The goal of this thesis is to design and operate an instrument capable of exploring this great untapped discovery potential.

2. OPTIMA

OPTIMA, the *Optical Pulsar Timing Analyzer*, is a fast, single-photon sensitive optical photometer [Straubmeier et al., 2001, Kanbach et al., 2003, Stefanescu et al., 2008a]. It uses optical fibres to couple light from fixed apertures in the focal plane to APD detector modules, while the field surrounding the apertures is imaged using a standard CCD detector. The detectors employed in OPTIMA react within 300 ps to incoming photons, and are rated for a sustained count-rate of up to 2 Mct/s (see Chapter 2.3). The DAQ[1] system samples the state of the detectors every 4 µs, thus the effective time-resolution is 4 µs (see Chapter 2.5). The detectors have a very high quantum-efficiency of 70% at 700 nm, and above 25% in the spectral range of $450 - 950$ nm (see Fig. 2.11). The system was designed from the ground up as a guest instrument, easily adapted to different telescopes. It can be reconfigured for photometric, polarimetric or spectroscopic use within one observation run.

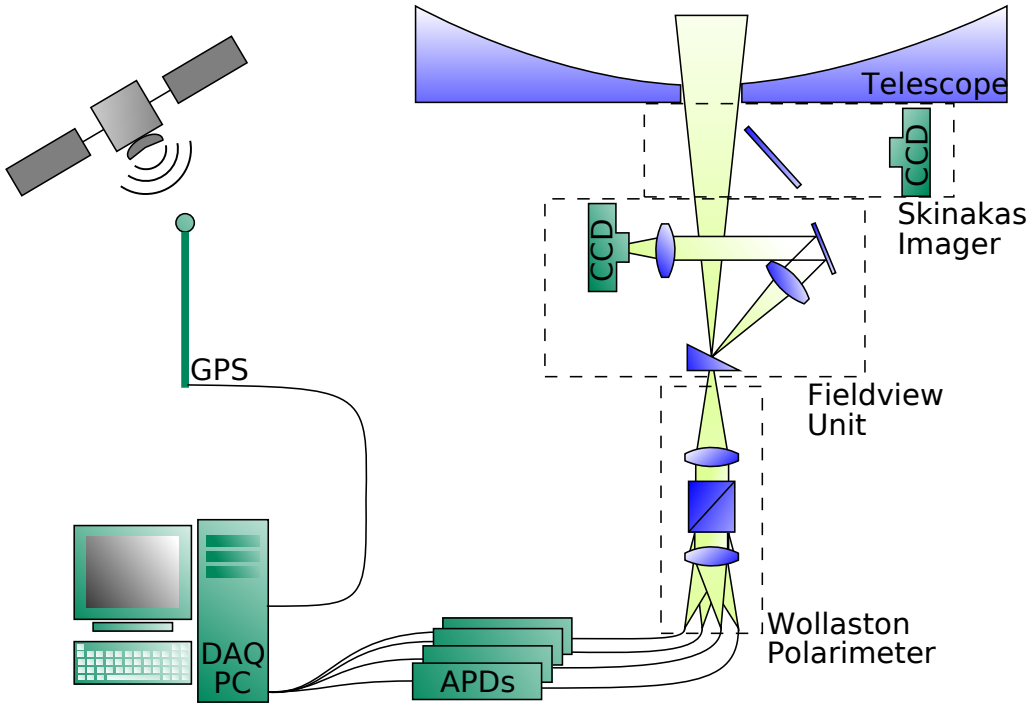

Figure 2.1.: Overview over the OPTIMA instrumental setup as used in this work. For clarity only the four polarimetry channels are shown, an additional photometry channel, six background-channels surrounding the photometry channel and one more distant background channel are also in routine use. See Fig. 2.4 for a close-up image of the fibre apertures.

[1]Data Acquisition System

OPTIMA was successfully used at various observatories, e.g. at the SKO[2] on Crete (1.3 m), the Mt. Stromlo Observatory in Australia (1.88 m), the SAAO[3] in South Africa (1.9 m), the GHO[4] in Mexico (2.15 m), the NOT[5] on La Palma (2.6 m) and the CAHA[6] in Spain (3.5 m).

Although OPTIMA was initially designed for optical pulsar studies (as is implied by the name), and pulsar observations are one area in which OPTIMA excels due to its high time resolution, it is not limited to pulsar studies. In fact, two of the most successful measurements performed by OPTIMA so far were not pulsar related:

In 2001, OPTIMA observed the black-hole candidate XTE J1118+480 simultaneously to observations using RXTE, a X-ray satellite designed for high-time-resolution observations. The autocorrelation of the optical light was narrower than the autocorrelation of the X-ray radiation, indicating an independent origin of the optical radiation. This contrasts with the expectation of reprocessed X-ray radiation as source of the optical emission. Furthermore, the cross-correlation between the optical and the X-rays showed a "pre-cognition dip", i.e. reduced optical emission shortly *before* a rise in the X-rays. [Kanbach et al., 2001]

In 2007, OPTIMA observed the X-ray transient J1955, initially detected by the *Swift* satellite as GRB 070610 (Chapter 6). OPTIMA detected optical flaring activity of a unprecedented intensity. The overall optical light-curve as well as details about the observation gave rise to the speculation that J1955 was actually the first magnetar to have shown optical flaring. [Stefanescu et al., 2008b]

2.1. Telescope

While OPTIMA is a mobile instrument that can be adapted to most medium to large sized telescopes, it can make sense to optimize it towards use at one telescope, if that improves some important aspects of the total system significantly. In the case of OPTIMA-Burst, the observation of GRB afterglows was stated in 2003 as prime objective for the coming years.

GRBs occur isotropically distributed across the sky, and Poisson-distributed[7] in time, i.e. the probability of a GRB occurring is the same for each element of time and each patch of sky. As the rough rate of GRBs to be expected in the *Swift*-era is ~ 100 per year, half of which will light up below the horizon, half of which will occur during the day etc., catching a GRB "on the fly" is not a common event. The driver for choosing a telescope must therefore be availability of large amounts of telescope time – both standby time as well as interrupt time to actually follow up on triggers. On the other hand, the telescope should be as large as possible, so that fainter sources are accessible. Big telescopes obviously are in higher demand than small telescopes, making both goals contradictory.

For OPTIMA, a good trade-off has proven to be the SKO 1.3 m telescope, shown in Fig. 2.2. With 1.3 m aperture diameter it is larger than most robotic GRB follow-up

[2]Skinakas Observatory
[3]South African Astronomical Observatory
[4]Guillermo Haro Observatory
[5]Nordic Optical Telescope
[6]Centro Astronómico Hispano-Alemán
[7]to be precise, the GRBs being counted are actually the outcomes of discrete trials, and would more precisely be modelled using the binomial distribution. However, GRBs are *rare events*, for which the binomial distribution approaches the Poisson distribution.

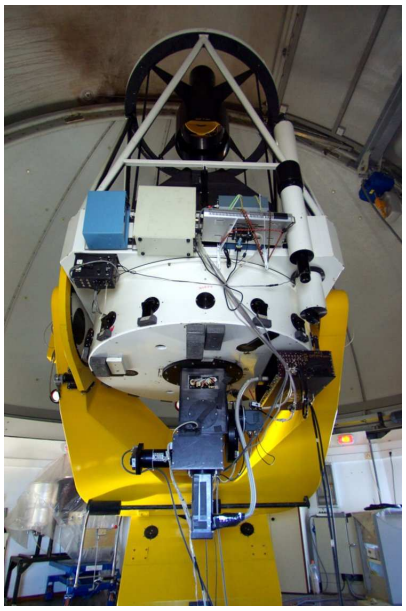

(a)

Skinakas Observatory Technical Parameters	
Type: Modified Ritchey Chrétien	
Aperture of main mirror	129 cm
Aperture of secondary mirror	45 cm
Central hole of main mirror	35 cm
Distance main to secondary	235.34 cm
Focal length	985.7 cm
f-ratio	7.64
slew rate	2.5°/s

(b)

Figure 2.2.: The 1.3 m Telescope of the Skinakas Observatory. Panel (a) shows the telescope with OPTIMA mounted. Panel (b) shows some technical parameters of the telescope.

observatories (ROTSE[8], Super-LOTIS[9], RAPTOR[10] etc.) by about a factor of 2. While slower than the robotic telescopes, it slews faster than the typical $2-3$ m class telescopes by about a factor of 2. Most importantly, SKO is a collaborative project run by the UoC[11], FORTH[12] and MPE[13]. As the telescope is partly run by the MPE, an agreement could be achieved by which OPTIMA remained mounted for a total of more than 300 days in standby mode, having full instant interrupt rights in case of a GRB trigger.

2.2. Focal Assembly

An overview over the focal assembly is shown in Fig. 2.1. The focal assembly consists of the GAM[14], the Field-View Unit and the Wollaston Polarimeter.

2.2.1. Guider Acquisition Module

The GAM is the optical switch box that directs light to the different instruments mounted at the telescope. The GAM houses a moveable mirror that can direct the light to different instruments mounted at different ports of the GAM. In the case of OPTIMA mounted at SKO, The GAM mirror sits at a fixed angle, but can be moved out of the optical path

[8]Robotic Transient Search Experiment
[9]Livermore Optical Transient Imaging System
[10]Rapid Telescopes for Optical Response
[11]University of Crete
[12]Foundation for Research and Technology – Hellas
[13]Max-Planck-Institut für extraterrestrische Physik
[14]Guider Acquisition Module

entirely. The position in the direct, unreflected path is used by OPTIMA to facilitate polarimetric observations. The position at the 90° port is used by the SKO imager. Since the optical distance from the main mirror to the instruments is not necessarily precisely the same, the telescope focus has to be adjusted when switching between instruments.

The telescope is equipped with an autoguider, which is an integral part of the GAM and can be operated independently from the OPTIMA autoguider-mode (Chapter 3.1.6) Some light is permanently directed to the autoguider from the edge of the field. Since spherical aberration has a strong effect at the edge of the field, the autoguider optics includes corrector optics. Because the telescope is focused by moving the secondary mirror (not shown in Fig. 2.1), the focus of the autoguider has to be adjusted as well, when the telescope-focus is adjusted for a switch between instruments (Chapter 3.1.2).

2.2.2. Field-View Unit

The apertures used by the OPTIMA system are smaller than the usual open-loop pointing accuracy of most telescopes. On SKO, the open-loop pointing accuracy is of the order 10″, whereas the aperture diameter is 6″. Therefore, more direct control over the pointing of the telescope is needed to accurately position the source onto an aperture. For this purpose, OPTIMA has a Field-View Unit imaging the current field and the location of the apertures.

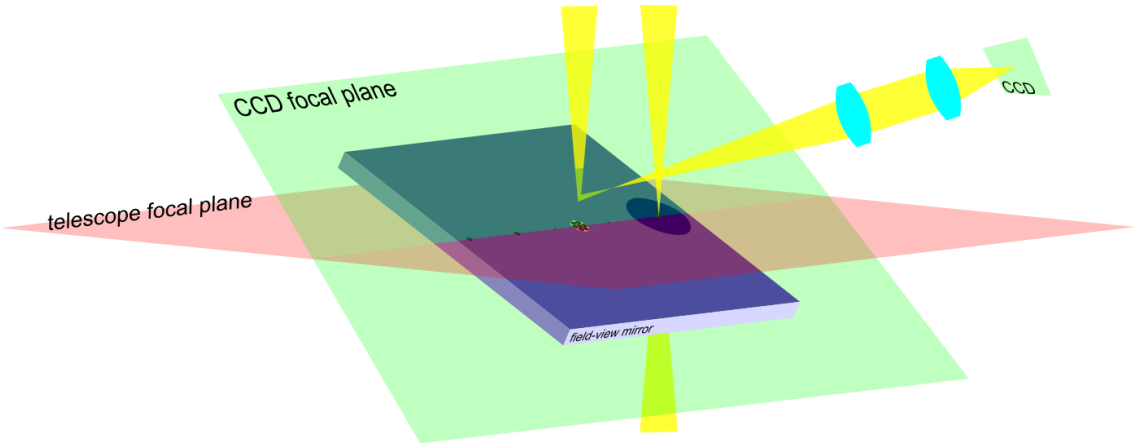

Figure 2.3.: Schematic diagram of the path of light at the slanted mirror. Shown in yellow are one path of light into the CCD on the periphery of the slanted mirror, and the path of light through the polarimetry aperture. To make sure that sources are focused correctly onto the apertures, the three planes of the mirror surface (dark blue) the telescope focal plane (red) and the CCD focal plane (green) have to intersect in the line all apertures are lined up on.

To image the field of view surrounding the apertures, the apertures are implemented as holes in a mirror. The light reflected by the mirror is directed to a CCD camera by a folded, and therefore compact, optical setup. Since optically the CCD sits behind the focal plane of the telescope, the light has to be re-imaged onto the CCD camera. For a maximum achievable FoV[15], this is done using a focal reducer. Fig. 2.3 shows a schematical overview over the optical setup of the mirror. Switching between observation modes is done by positioning the target onto one of several apertures (Fig. 2.4).

[15]Field of View

For photometry observations OPTIMA uses a hexagonal bundle of fibres (Fig. 2.4(b)). The target is positioned onto the central fibre, the surrounding six fibres are used to determine the sky background. Further background measurements are obtained by an additional, more distant background fibre.

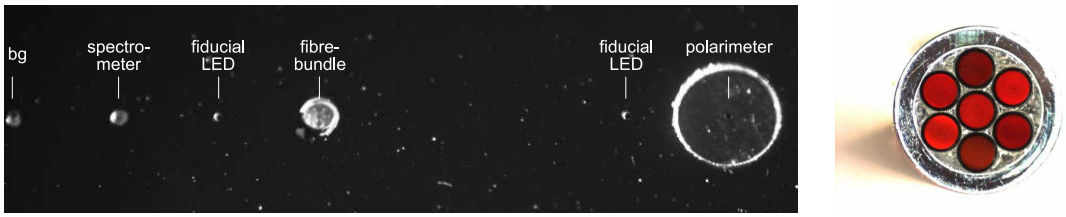

(a) (b)

Figure 2.4.: OPTIMA apertures. In (a), the photometry and polarimetry apertures embedded into the slanted mirror is shown. The hexagonal photometry fibre bundle can be clearly seen as central set of apertures. Figure (b) shows a microphotograph of the fibre bundle.

For polarimetry observations, there is one aperture implemented as diaphragm inset into the mirror. Behind this is a twin-Wollaston prism polarimeter, measuring the full linear Stokes vector simultaneously (Chapter 2.2.3). Optionally, an additional fibre aperture can be used to feed a four-channel low resolution prism-spectrograph. This spectrograph can be used for time-resolved colorimetric observations of bright sources.

In addition to the various OPTIMA apertures, two LEDs[16] are incorporated into the slanted mirror as fiducial lights. These are needed to simplify the identification of the OPTIMA apertures, and to accurately measure the position of each aperture, so that targets can be automatically positioned onto each one (Chapter 3.1.5).

The Field-view Optics

The imaging setup to capture the FoV OPTIMA is pointing at must combine several contradicting design goals, requiring careful trade-offs in its design. The first requirement is a big FoV. The field should measure at least $10' \times 10'$, and be ideally as big as $15' \times 15'$, so that even large error-boxes, e.g. those of source position derived by γ-ray satellites, are fully covered in a single exposure. As large area CCD detectors are very expensive, the FoV should be imaged onto an image size of 2.5×2.5 cm^2 or less. The quality of the image should be sufficiently high for the image to be usable for the identification of the patch of sky and of individual (possibly unexpected) sources. In order to identify transient sources through their variability, lots of images with short exposure times have to be taken in quick succession. The read-out times of the CCD-system used therefore should be as short as possible, to loose as little light between the exposures as possible and offer as much time-resolution as possible for transient identification.

Using $l = f \tan(\alpha)$ and the focal length of the 1.3 m telescope of the Skinakas Observatory, $f = 985.7$ cm, the size of a $15'$ FoV in the focal plane follows as $l = 4.3$ cm. The optics re-imaging the image in the prime focal plane onto the CCD camera therefore must scale the image down by roughly a factor of 2. This is achieved by a *focal reducer*, an

[16]Light Emitting Diodess

optical setup that collimates a divergent beam into a parallel beam, and re-images the beam using a smaller f/D ratio than that of the telescope. The optical path of the focal reducer used in OPTIMA is folded using a mirror in the optical housing. An overview schematic of the optical setup is shown in Fig. 2.3.

The focal reducer used in OPTIMA consists of a Tessar 3.5/250 aerial photography lens as collimator, and a Visionar 1.9/141 medium format photography lens as objective lens. These classic lenses are of very high optical quality, have a very large usable FoV and flat focal plane, while being quite affordable. The ratio of the focal lengths of both lenses, $f_{\text{collimator}}/f_{\text{objective}} = 250\,\text{mm}/141\,\text{mm} = 1.77$ defines the reduction ratio of the focal reducer. A FoV of $15' \times 15'$ is therefore imaged onto a focal plane of $2.4 \times 2.4\,\text{cm}^2$.

The image is recorded by an Apogee AP6 camera. This camera uses the KAF1000E CCD by Kodak, with 1024×1024 pixels of $24.5 \times 24.5\,\mu\text{m}^2$ size, resulting in a CCD chip size of $2.5 \times 2.5\,\text{cm}^2$. The CCD camera is connected to the controlling computer using a proprietary parallel interface which allows to read out a complete frame in slightly more than one second.

Focusing

Since the CCD camera must not obstruct the optical path coming from the telescope, the aperture-mirror must be slanted. This introduces an interesting problem: As all apertures are supposed to be in the focal plane of the telescope simultaneously, the apertures can't be positioned arbitrarily on the slanted mirror, but must be positioned along the intersecting line between the focal plane of the telescope (red surface in Fig. 2.3) and the surface of the mirror. To focus the telescope, the FWHM[17] of stellar images are observed on the CCD camera. It is therefore not possible to *directly* determine whether the apertures are situated correctly in the focal plane of the telescope. Instead, the distance between the CCD camera and the focal plane of the CCD camera (the distance between the two green planes in Fig. 2.3) is adjusted in such a way that they intersect in the line of apertures (i.e. the internal focus is adjusted so that exactly the line in which the apertures are lined up is in focus).
In a second step, the telescope is focused in the usual way, so that the (reflected) CCD focal plane and the telescope focal plane line up. The end result is shown in Fig. 2.3: all three planes intersect in the line of the apertures.

2.2.3. Twin Wollaston Polarimeter

In the optical, the polarization state of a beam of light cannot be easily measured directly, in contrast e.g. to γ-rays or X-rays, where the interaction of the photon in the detector is polarization-dependent. [Costa et al., 2008] Therefore, information about the polarization state is imprinted on a different measurable quantity of the beam of light, e.g. intensity or direction. To modulate the light, two approaches are widespread: polarizing filters and birefringent prisms.

In a previous implementation of the OPTIMA polarimeter, the polarizing filter approach was used. A polarizing filter preferentially absorbs light of a specific polarization direction, i.e. it absorbs a different fraction of incident light depending on the polarization state. The complete polarization state can be deduced by combining measurements taken with different polarization filter positions. The main advantage of this method is that it is easy to build a system that encodes the polarization state of the whole field of view.

[17] Full Width at Half Maximum

As the polarization of the background, which is measured simultaneously to the target, is encoded identically to the source, it is relatively straightforward to subtract. One downside, however, is that due to the filtering nature of the polarization encoding, an ideal polarizer transmits only 50% (unpolarized) light. Usually though, the transmittance of the correct polarization direction does not reach 100%, so the overall throughput of a polarizing filter polarimeter usually is of the order $\approx 30\%$.

In the context of a time-resolved polarimeter, an additional problem occurs with the polarizing filter approach. Usually, the individual polarization state measurements in this approach are separated in *time* by rotating the filter in front of the instrument aperture. As long as the time-scale of the observed variabilities is slow in comparison to the rotation of the polarizer, enough polarization projection measurements can be accumulated to reconstruct the brightness and/or polarization variability. If the source changes as quickly as or quicker than the polarizer rotates, changes in brightness and polarization cannot be distinguished any more. One notable exception to this is if the variability is periodic, with a period non-commensurable to the polarizer rotation period. As the previous implementation of the OPTIMA polarimeter was designed to take polarization measurements of pulsars, this downside did not play a dominating role: the polarization of the Crab pulsar and nebula, which are bright enough for the rotating filter approach, was measured in extreme detail using this approach [Słowikowska et al., 2009].

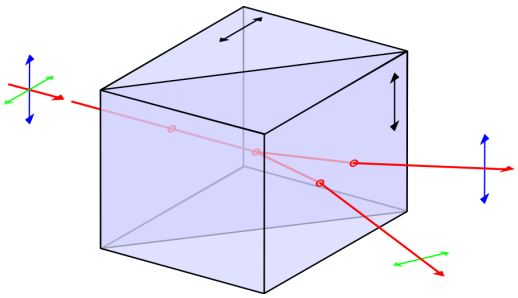

(a) A Wollaston prism separates randomly polarized or unpolarized light into two orthogonal, linearly polarized outgoing beams. Due to the symmetric nature of the outgoing beams, it lends itself to optical setups with a common objective lens. (see e.g. Fig. 2.7)

(b) The twin-Wollaston prism used in the OPTIMA polarimeter. Two Wollaston prisms, separated by an opaque divider, are mounted in a single housing. The polarization projection directions are rotated by 45° (× and + signs), whereas the beam split directions are rotated by 90° (⇔ and ⇕ signs).

Figure 2.5.: Wollaston prism

Since OPTIMA was oriented towards more general astronomical high-time-resolution observations, a new polarimeter based on a different approach was built as a diploma thesis [Mühlegger, 2006], supervised within the scope of this work.

In the new approach, instead of filtering the light according to polarization projection, a Wollaston prism (Fig. 2.5) is used to refract the light into different directions according to polarization projection. To deduce all parameters describing linear polarization (either intensity I, polarization degree p and polarization angle ϕ or the three Stokes parameters I, Q, U), the measurement of at least three linearly independent polarization projections are required. Measuring two projections, as in the case of a single Wollaston prism, results

in an under-determined system of equations, and hence in an ambiguous solution. This is easily seen graphically in Fig. 2.6. Therefore, the new OPTIMA polarimeter was built as a *twin*-Wollaston polarimeter.

Using four projections to determine three values introduces new difficulties. As the system now is over-determined, a naïve geometry-based approach of combining the measurements cannot combine all four measurements. Moreover, this simple approach fails to consider non-ideal orientation of the projection directions, or non-ideal polarizer efficiencies. However, using a matrix-based analysis approach proposed by [Sparks and Axon, 1999] these difficulties can be overcome (See Chapter 4.5).

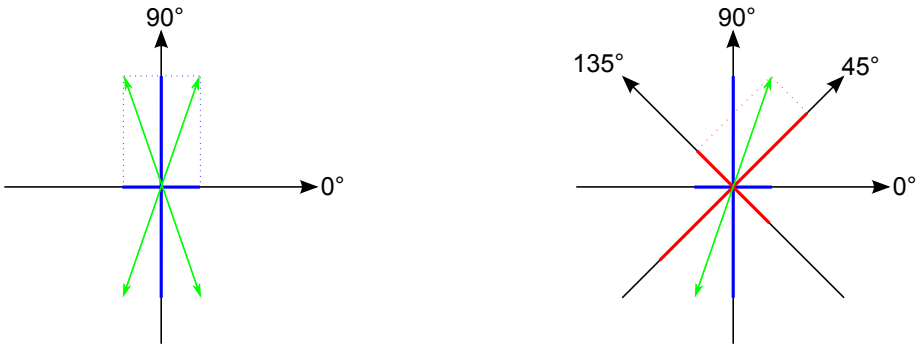

(a) (b)

Figure 2.6.: Basic principle of measurements of linear polarization. One Wollaston prism measures two projections of the polarization state. For all angles but 0° and 90°, this results in an ambiguity (a). At least one more measurement is required to resolve this ambiguity. Two Wollaston prisms measuring four projections allow measurement of the polarisation state without ambiguities (b).

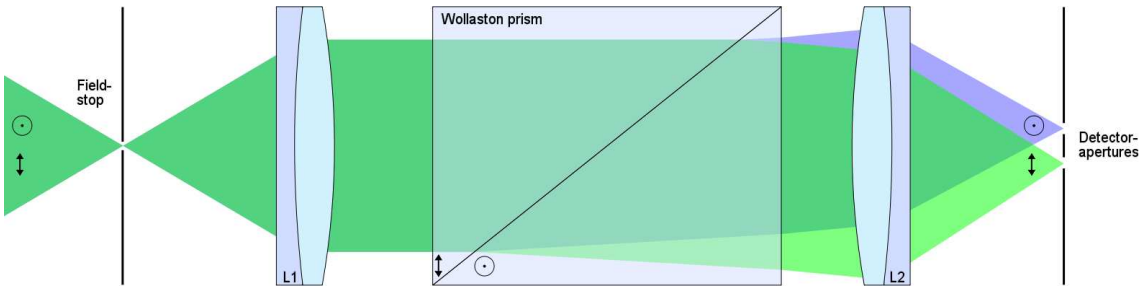

Figure 2.7.: Wollaston polarimeter optical overview schematics. A field stop in the telescope focal plane and a collimator lens (L1) project the light through a Wollaston prism. The prism splits the collimated beam into two collimated beams, separated by $\approx 1°$. These two beams are imaged onto the detector apertures using a single objective lens (L2).

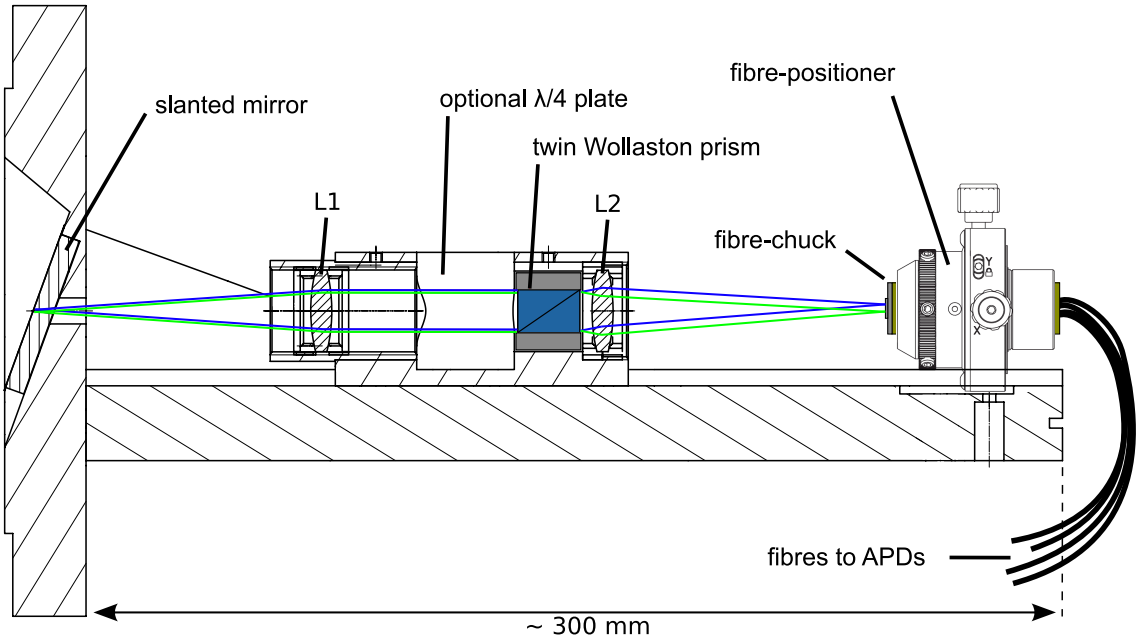

Figure 2.8.: Technical drawing of the OPTIMA Twin-Wollaston Polarimeter. [Mühlegger, 2006]

Implementation of the Twin-Wollaston Polarimeter

In the setup of the new polarimeter for OPTIMA, two Wollaston prisms are mounted within one housing (Fig. 2.5(b)). One of the Wollastons is cut in a slightly different way than shown in Fig. 2.5(a), so that the polarization projections are rotated by 45° with respect to the exit directions. The two Wollastons mounted together are rotated by 90° with respect to each other. When this setup is illuminated across its whole (split) entrance aperture, it splits the light in four directions ("up", "down", "left" and "right") according to four polarization projections (0°, 90°, 45° and 135°).

The twin-Wollaston prism is the centerpiece of the new OPTIMA polarimeter. An overview over the optical concept of the polarimeter is given in Fig. 2.7, and a technical drawing of the actual implementation is given in Fig. 2.8. Light from the source is focused onto a slanted mirror by the telescope (see Chapter 2.2.2), into which an aperture of 300 μm diameter is inset. This aperture works as a field stop with a collimator lens focused onto it. The parallel beam projected by the collimator lens illuminates both halves of the twin-Wollaston prism, and is split up into four beams. A common objective lens images these four beams as four dots in a cross-like pattern onto fibre apertures leading to APD detectors.

The manufacturing process of the Wollaston prisms cannot control the refraction angle to arbitrary precision. Therefore the positions of the four star-images cannot be predicted accurately before actually building the polarimeter. As a system of four fibre pick-ups fully adjustable in x and y directions would be extremely complex in the confined space that is available for the polarimeter, a system of a combined quadruple fibre pick-up was designed.

The quadruple pick-up consists of a fibre-chuck manufactured to duplicate the exact focal pattern produced by the polarimeter optics, and a positioning unit making the fibre-

chuck adjustable in four degrees of freedom (x, y, z and rotation). To copy the exact focal pattern of the polarimeter optics onto the fibre chuck apertures, the fibre-chuck was coated with a photo-sensitive dye and illuminated with the fully finished polarimeter optics. The resulting spots on the surface of the fibre-chuck were used as marks for high-precision drills to produce the apertures in the correct positions. In a last step, optical fibres were inserted into the holes, glued into place and polished together with the fibre-chuck surface [Mühlegger, 2006].

2.3. Detector Unit

OPTIMA uses fibre coupled photon detectors. The main advantage of this setup is the mechanical construction of the focal assembly: the detectors used in OPTIMA are not positionally sensitive, necessitating a field-viewing setup as described in Chapter 2.2, and are not compact enough to be directly incorporated in its design. By using optical fibres to couple light from the telescope focal plane into the detectors, they can be placed at an arbitrary position outside the focal plane. On the other hand, fibre coupling does introduce a number of problems that need to be addressed.

2.3.1. Fibres

OPTIMA uses all-silica multi-mode step-index optical fibres custom built by *fibertech* and *efoquarz*. In multi-mode fibres, the diameter of the core that actually guides the light by total internal reflection is large compared to the wavelength of the light, which makes a description using geometric optics possible (see Fig. 2.9). Using geometric optics, the f-ratio of the acceptance cone of a fibre with a refractive index n_1 in the core and n_2 in the cladding can be estimated as:

$$(f/D)_{max} = \frac{1}{2\sqrt{n_1^2 - n_2^2}}$$

The term *multi-mode* indicates that due to the large diameter of the fibre core, there are many different paths that allow lossless transmission of rays of light through the length of the light guide. The different possible paths are called “modes”, hence the name “multi-mode” fibre. Each mode in a multi-mode fibre corresponds to a specific total internal reflection angle. If the fibre is bent, this angle can change for one path of light, allowing light from one mode to cross into another. If the bending is sufficient, all modes are filled equally with light. This is called “mode scrambling”. As the different paths have different lengths, the propagation time down the fibre depends on the mode. This introduces a broadening of very short pulses of light in a multi-mode fibre called *modal dispersion*.

As optical fibres are often used in communication applications on timescales of nano-seconds and below this is not acceptable for these kind of application: short-duration pulses as needed for high-speed communication would bleed into each other. The remedy in these cases are single-mode fibres, using a light-guide with a diameter comparable to the wavelength of the light. Here, a geometric description of the light propagation fails: the optical fibre works similar to a microwave wave-guide, allowing exactly one propagation mode. As OPTIMA has a time-resolution of 4 µs, the modal dispersion of a multi-mode fibre only starts to play a role for light-guide lengths of hundreds of metres, much longer than used in OPTIMA. Therefore the benefits of multi-mode fibres, especially the much bigger “light-gathering” capacity due to the bigger core, dominate.

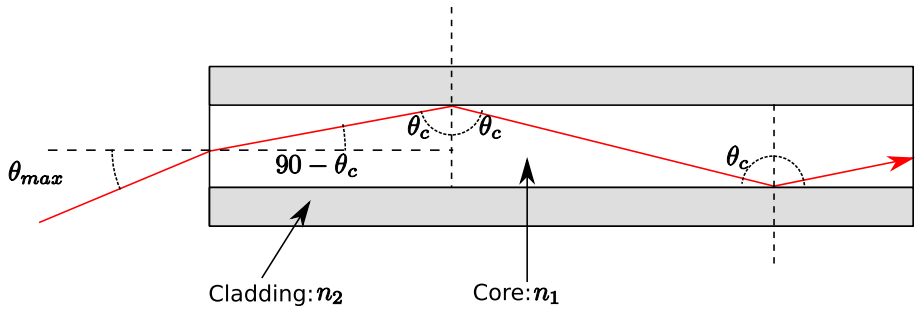

Figure 2.9.: Overview over an optical fibre. Only light illuminating the fibre within the fibre's *acceptance cone* $\theta < \theta_{max}$ will satisfy the total internal reflection condition $\theta < \theta_c$.

As OPTIMA uses the fibre cores directly as photometry apertures[18], the core diameter has to be adapted for the intended observing conditions. The light of a point source is spread out by diffraction at the telescope aperture, optical aberrations and atmospheric conditions ("seeing") to a spot of light with a characteristic profile, the PSF[19]. Typically, the PSF is well described by a Gaussian core and an additional halo. At SKO, typical seeing conditions result in a FWHM of the PSF of 1″-2″. As it is desirable to gather most of the light even under adverse conditions, the aperture should be three times the FWHM, or 6″. At a focal length of 9857 mm, this corresponds to 286.7 µm. As 300 µm (corresponding to 6.3″) is readily obtainable as fibre core, this was chosen as aperture diameter.

Just as the photometry aperture end of the fibre has to allow efficient coupling of light into the fibre, the detector-end of the fibre has to guide as much light as possible into the detector itself. Each detector consists of a cigar-box sized avalanche photo diode module (Chapter 2.3.2), which contains the 100 µm large detector chip along with cooling infrastructure and front-end electronics. Coupling light directly from the 300 µm exit aperture of a fibre into the 100 µm detector, means losing most of the light by missing the detector. There are two possible remedies for this problem, each with it's own advantages and disadvantages.

The first method consists of utilizing a micro-optical lens at the exit aperture of the fibre to focus the 300 µm exit pupil to a spot of 100 µm or less. While the advantage of this approach is that an unmodified fibre can be used, the disadvantage of this method is an additional degree of freedom to be adjusted. Besides the necessary adjustment of the fibre in the x-y plane in front of the detector, the micro-optical array has to be correctly focused as well.

The second approach to couple as much light as possible into an area smaller than the core of the fibre, is to reduce the size of the core. As the entry aperture has to remain large by necessity, this means tapering the fibre core down from a big diameter to a smaller diameter at the exit aperture. The advantage of this method is that the exit aperture can be butted against the entry window of the detector, eliminating one degree of freedom in adjustment. The remaining adjustments can be performed during the manufacturing process, so that the fibre can be simply mounted in an industry standard FC[20] type fibre connector.

[18] except in the case of the polarimeter
[19] Point-Spread Function
[20] Ferrule Connector

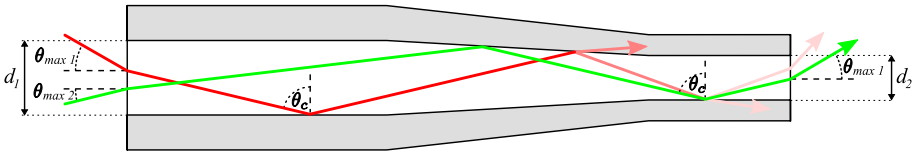

Figure 2.10.: Illustration of a tapered fibre. Light coupled into the wide end of the taper satisfying the launch condition of Fig. 2.9 is lost in part at the taper. Therefore, a tapered fibre has a more narrow effective acceptance cone.

The downside of a tapered fibre is that if light is coupled into the wide end of the fibre taper at the full acceptance cone of the fibre, some light hits the border of the core at an angle steeper than the total internal reflection angle θ_c (see Fig. 2.10). The same can happen if the light coupled into the fibre is guided along a sufficient length to scramble into all modes upstream of the taper. The light hitting the core of the fibre at too steep an angle is partly refracted out of the core into the cladding, and thus lost. To make sure θ_c is not exceeded at (or after) the taper, the acceptance cone has to be reduced accordingly. If $d_1 > d_2$ are the big and small diameters of the taper, the f-ratio of the reduced acceptance cone can be approximated as:

$$(f/D)_{red} = \frac{1}{2\sqrt{n_1^2 - n_2^2}} \cdot \frac{d_1}{d_2}$$

Fibre tapers can be produced by gently stretching the fibre while heating it over a flame, thereby reducing the diameter. As the full mode-space is filled by mode-scrambling after some length of (bent) fibre, it makes sense to incorporate the down-taper closely after the entrance aperture of the fibre. In the case of the fibres used in OPTIMA at SKO, short 300 µm fibres are tapered down to 100 µm and cemented to constant-diameter fibres of 100 µm diameter for the bulk of the length. The broad, tapered fibre and the contact area of the narrow fibre (plus some margin) are encased in a stabilizing metal tube. In the fibre-bundle, all seven fibres are similarity tapered and glued into one common metal tube.

2.3.2. APDs

The central part of any astronomical instrument are the detectors. OPTIMA uses APDs as photon counters. The main advantage of APDs compared to PMTs[21] often used for astronomical photon counting applications is the combination of the much higher quantum efficiency of solid state detectors and the high amplification offered by PMTs (see Fig. 2.11). In a PMT, light hits a photo-cathode, usually implemented as a coating of an alkali metal[22] on a thin electrode. If the absorbed photon is of sufficient energy, an electron is emitted from the photo-cathode. The electron is accelerated with an electric field generated by a series of high-voltage electrodes, called *dynodes*. The energy gained by the electron is high enough for it to release secondary electrons upon hitting the next dynode in its path. As each dynode is on a more positive potential than the previous one, the secondary electrons are in turn accelerated towards the next dynode. This process is

[21] Photo Multiplier Tubes

[22] As alkali metals are in the leftmost column of the periodic table, their *work function*, or electron binding energy, is especially low

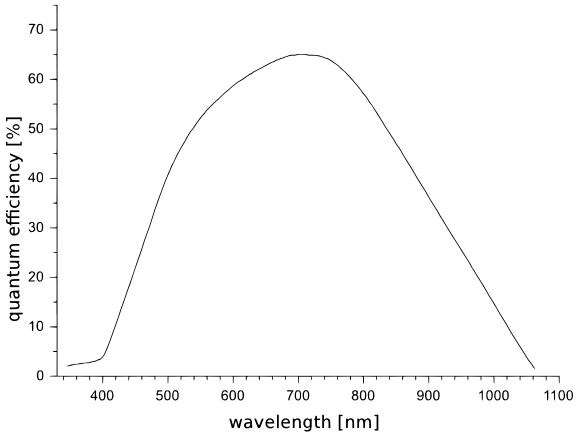

Figure 2.11.: Quantum efficiency of the Perkin-Elmer APD photon counter units [Perkin-Elmer, 1997]

repeated a number of times, so that ever greater number of electrons being produced in each stage. Depending on the number of steps and the voltage across each step, the current amplification can be set from a linear response with relatively moderate amplification to a very steep response[23] with amplifications $> 10^5$, high enough to detect individual photons.

One principal problem designing a PMT is that on the one hand the photo-cathode needs to be as thin as possible, so that light striking the photo-cathode from one side can emit an electron on the other side. On the other hand the sensitive material should be as thick as possible, to maximize absorption of photons. These diametrically opposed design goals limit the quantum efficiency of PMTs to about 40%

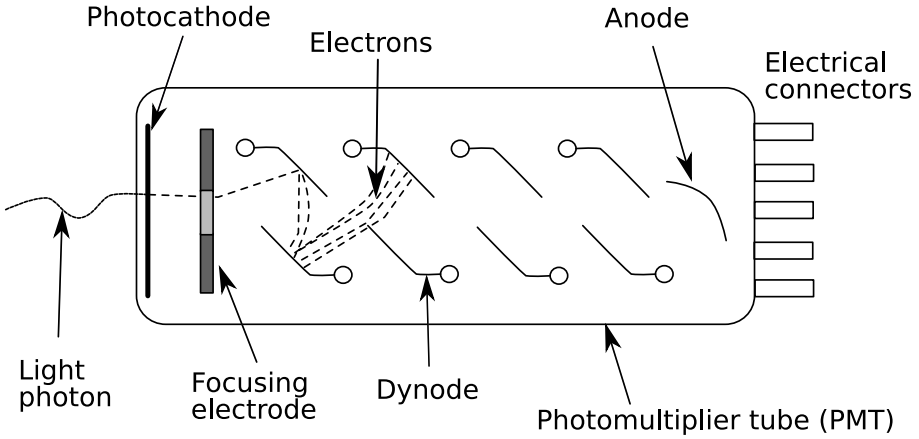

Figure 2.12.: A Photo Multiplier

In a semiconductor-based photo-detector, light is absorbed in the bulk of the material. A common implementation of a solid-state photo detector is the PIN[24]-diode, reverse-biased and in a clear casing.

In a diode, a p-type and an n-type semiconductor are brought into contact (Fig. 2.13(a)). The majority charge carriers of each region drift into the other region, leaving behind a

[23]This regime is called "Geiger mode", as it is similar to the workings of Geiger counters.
[24]p-i-n Diode

net space charge. Once drift and the attraction of the space-charge are in equilibrium a stable zone forms with very little majority charge carriers, the depletion zone. If the diode is forward biased, the external field counteracts the field of the space charge, reducing the size of the depletion zone until current can flow. If the diode is reverse biased, the depletion zone is enlarged and no current can flow.

If however a photon of sufficient energy is absorbed within the depletion zone, an electron-hole pair will be produced, and the electrical field of the space charge at the junction will separate the pair. Thus a photo-current is produced.

In the application of a photo-detector, a large depletion zone is desirable, as the depletion zone forms the active detector volume. To expand the depletion zone, a layer of intrinsic semiconductor, i.e. a semiconductor with no or very low doping concentration, can be inserted between the p-type and n-type layer. This p-i-n structure still functions like a p-n junction and is therefore called PIN-Diode (Fig. 2.13(b)).

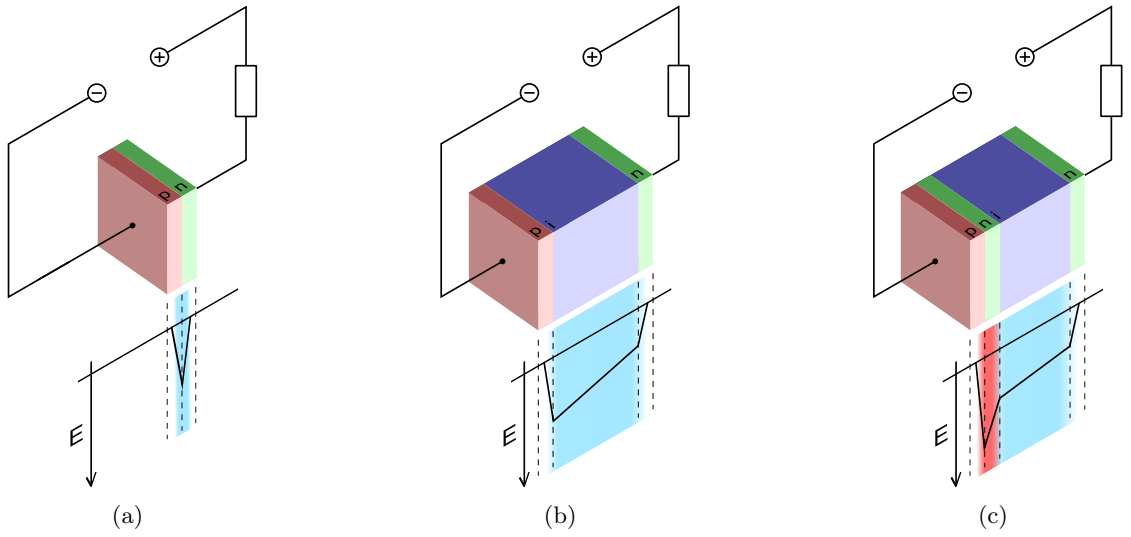

Figure 2.13.: Schematic overview of the APD concept. In the depletion zone (blue shaded area) of a p-n junction (a), charge carriers generated by the absorption of a photon are separated and lead to a photo-current through the reverse-biased diode. To extend the depletion zone, and hence the active detector volume, an intrinsic layer i is added to the p-n junction in the PIN-diode (b). If the reverse bias voltage is very high, avalanche amplification can occur. This results in macroscopic currents even for individual photons, but is not easily controlled across the full depletion zone of a PIN-diode. In an APD (c), a further highly n^+ doped area is added to the p-i-n structure, to introduce an intrinsic high-field region (red shaded area). As the field necessary for avalanche amplification is reached in this region first, the properties of the avalanche can be controlled by controlling the geometry of this region. In this way, both a very high amplification and a very large sensitive volume can be achieved in an APD.

The charge carriers are accelerated by the reverse bias voltage, and will therefore gain energy. If the bias voltage is high enough, they can gain sufficient energy to produce secondary electron-hole pairs through impact ionization. If the free path length of the

accelerated charge carriers becomes short enough, an avalanche process ensues, very similar to the discrete avalanche from dynode to dynode in a PMT. As an uncontrolled avalanche can destroy the device, care needs to be taken to control the exact conditions under which the avalanche can start. In a PIN-diode, the electric field in the intrinsic layer remains relatively constant. Therefore, the exact location where the avalanche starts is strongly influenced by small local variations, making it hard to control the avalanche condition. To better control the onset of the avalanche while keeping the large depletion zone of the PIN-diode, a further highly doped region can be added, which creates a high-field region. The high field region is relatively small and the field configuration can be finely controlled by doping profiles and structure geometry. Therefore, the high-field region can act as an avalanche multiplication region, while the charge carriers in the bulk of the active detector volume still drift below avalanche threshold. The resulting device, shown in Fig. 2.13(c), is thus called an Avalanche Photo-Diode.

Similarly to a PMT, the amplification factor can be chosen in a wide range by the geometry of the device and the applied bias voltage. If the reverse bias voltage is below the breakdown voltage V_B of the APD, the avalanche current remains proportional to the incident illumination. If the bias voltage is higher than V_B, a single charge carrier injected into depletion zone can trigger a *self sustained* avalanche. The current rises swiftly (within < 1 ns of absorption of the initial photon) to a macroscopic steady level in the milliampere range. APDs designed to be run in this Geiger mode regime are called SPADs[25].

Since a single photon is enough to trigger the self-sustaining macroscopic current and the rise-time of the leading edge of the photo current is extremely steep, a SPAD is ideally suited for recording arrival times of incident photons. However, after a photon triggered the SPAD, the photo current needs to be actively stopped, or *quenched*, for the SPAD to be sensitive to the next photon.

As the whole setup of a SPAD including active quenching circuit, high voltage control and thermo-electric cooling is quite complex to setup, adjust and maintain, OPTIMA uses commercially available SPAD modules[26] combining the complete setup of a SPAD into a compact package requiring no external adjustments whatsoever. Essentially this SPAD module can be used as a "black box" that plugs into the FC connector of an optical fibre, and that outputs a TTL[27]-pulse of 20 ns duration within 0.2 ns after detecting a photon.

2.4. Time Base

The arrival time of photon detection pulses produced by the detectors is compared against a known time base by counting the oscillations of an oscillator of well known frequency. As the accuracy of the frequency the oscillator produces determines the accuracy of the timing measurement, this is a critical part of the complete setup. The term "accuracy" of the frequency can be broken down to three different concepts:

- Base frequency
- Frequency drift
- Phase jitter

[25] Single Photon Sensitive APDs
[26] Perkin Elmer SPCM-AQ [Perkin-Elmer, 1997]
[27] Transistor-Transistor Logic

The base frequency can be calibrated by comparison with another source of known frequency. This can e.g. be a calibrated oscillator in the lab, a special time signal transmitted by a national standards body, or even an astrophysical source. An error in the determination of the base frequency will introduce a systematic error into the time-measurement that can be described by a linear term.

The base frequency will generally not be absolutely stable with time, but will be subject to slow changes, or drifts. These can be induced by a variety of processes, the most important of which include temperature and degradation with age of the oscillator. The frequency drift will introduce a quadratic term into the systematic error of the time-measurement.

In addition, individual beats of the oscillator can be very slightly out of sync, i.e. the oscillator shows a phase-modulated error. This is called the phase jitter of the oscillator. The phase jitter will introduce a random-walk of the total phase, and therefore a statistical error.

The simplest implementation of a moderately high precision oscillator is a quartz-based crystal oscillator, like it is found millionfold in watches, computers and consumer electronics. Even simple crystal oscillators (XO[28]) have accuracies of a few tens of ppm[29], which can be improved to almost 1 ppm by simple temperature compensation. This is enough for most astrophysical applications, where the observation time involved is usually not longer than a few hours. For a quartz oscillator of 1 ppm, the phase error after one hour of observation of the Crab pulsar would still be only 0.1.

While enough for short measurements, higher quality oscillators are needed e.g. to compare Crab pulsar observations taken in different nights. Irrespective of the crystal oscillator quality, it will still suffer from temperature-induced drift under changing ambient conditions. By controlling the temperature of the complete oscillator (crystal and oscillator circuit), this problem can largely be circumvented. This will most easily be achieved by heating the oscillator to a pre-determined temperature in a thermostatically controlled oven. Oven-controlled Crystal Oscillators (OCXO) can achieve up to 10^{-12} short term precision and 10^{-8} per year long term drift.

For isolated observations a system like this is fully sufficient. If the observations performed with this setup are to be compared to observations performed separated in time or space, e.g. by folding a pulsar light-curve with a ephemeris determined by a radio telescope, or cross-correlating an optical light-curve with a light-curve obtained in X-rays, a new problem becomes apparent. While the *relative* photon arrival time has been determined with high precision, the *absolute* time has not. Therefore, a common standard zero-time has to be shared between observatories and/or individual observations.

The problem of simultaneity is classically solved by setting a portable clock to the time of one observatory, and then physically moving this clock to a second observatory. Needless to say that this method suffers numerous solvable but non-trivial problems. A more elegant solution is broadcasting a time-signal from one observatory by radio or wire, and subtracting the transit time of the time-signal. This method has two chief technical difficulties. First, the propagation delay is not trivial to determine, as it is not only dependent on the distance between the two stations, but also on the exact conditions along the propagation path. Secondly, clear reception of the time signal has to be ensured even for the most distant stations. The first problem can be calibrated by comparison of known clocks with the time signal – a single time is enough for the determination

[28] Crystal Oscillator (from Xtal)
[29] parts per million

if the exact distance, but continuous monitoring is necessary to calibrate for changing propagation conditions. The second problem can be circumvented by building a network of stations, disseminating the re-calibrated time signal to remote stations.

While not explicitly built for this purpose, a system fulfilling all requirements for global time base dissemination already exists: GPS[30].

The GPS accurately determines the position of a receiver by comparing the propagation delay of a precise timing signal from a network of radio stations. The radio stations are situated on 32 satellites, with each satellite carrying an atomic clock as time-base. The orbits of all satellites are tracked by a network of ground stations, periodically uploaded to the satellites and captiously broadcast by the satellites along with the timing signal. Ionospheric propagation delay corrections are performed by several public (e.g. WAAS[31], EGNOS[32]) or commercial (e.g. OmniSTAR) systems.

Essentially, a GPS receiver can be used as a globally synchronised time-base of excellent long-term stability. The jitter of a GPS receiver's time-signal is relatively high, but disciplining an OCXO or TCXO[33] with a GPS receiver yields a cheap, reliable, and widely accepted globally synchronised time base with excellent ($< 10^{-12}$) short *and* long term stability. OPTIMA uses a commercial setup of this type, a Datum Inc. bc627AT. The next generation data acquisition (chapter 2.5.2) uses a Trimble Thunderbolt.

2.5. Data Acquisition

After the detection of a photon, the fact of the detection needs to be recorded for later analysis. In this process, called *data acquisition* (DAQ), information coming from the GPS-disciplined clock and from the APDs are combined to an event word that is saved to hard-disk. The details of how to determine the exact time of a TTL-pulse marking the detection of a photon can be implemented in a number of different ways. The DAQ used in OPTIMA is implemented in a relatively straightforward way, but has a number of limitations. Therefore, a new DAQ concept was developed. However, the hardware for the new DAQ system is still under development.

2.5.1. The Classic OPTIMA DAQ System

The "old" DAQ system used in OPTIMA was originally developed in the scope of a doctoral thesis [Straubmeier, 2001] at the same time the rest of the original OPTIMA system was implemented. Fig. 2.14 shows a schematical overview over the DAQ. The DAQ system is clock-driven, i.e. for each clock cycle the DAQ samples the status of all photon detectors, filtering time slices with events from those without events at a later stage.

As detailed in chapter 2.4, the clock is implemented as a commercial GPS-disciplined OCXO card[34]. The sampling of the TTL outputs of the SPAD modules is performed using a commercial DIO[35] card[36]. As the logic of the DAQ system is mostly implemented in software on a multi-tasking operating system that cannot guarantee deterministic response

[30] Global Positioning System
[31] Wide Area Augmentation System
[32] European Geostationary Navigation Overlay Service
[33] Temperature Compensated Crystal Oscillator
[34] Datum Inc. bc627AT
[35] Digital Input/Output
[36] National Instruments PCI-DIO-32HS

times, care has to be taken to determine reaction-time critical portions of the logic and implement them in such a way, that reaction-time requirements are limited to what the operating system can provide.

In the case of a clock-driven DAQ, particular care has to be taken that the digital inputs are sampled once for every clock cycle. The clock in OPTIMA typically runs at 250 kHz, requiring a reaction time of just 4 µs after each clock pulse. Even in operating systems optimized for reaction time (RTOS[37]), this short a reaction time cannot be guaranteed. Therefore, a DIO card has been selected that can copy the state of all digital inputs as one data word to an internal buffer autonomously after receiving a trigger signal on one digital input. The internal buffer of the DIO card is then periodically copied into the main memory of the computer, where event selection is performed. The 32 kB of memory built into the DIO card as buffer reduce the response time requirement from 4 µs to $4\ \mu s/sample \cdot 32\ 2^{10}$ samples ≈ 130 ms, a reaction time that can be routinely guaranteed by even an unspecialized operating system, as long as only one user process is requesting a large amount of system resources. As a caveat resulting from this, the DAQ PC cannot be used for activities other than acquiring data during data acquisition.

The data throughput resulting from 250 k samples/s is only ≈ 244 kB/s. Using DMA[38] to copy the data from the internal buffer to the computer's main memory, this poses no difficulty for the bus of a typical PC.

Once the samples are in the computer's main memory, an event selection is run in software. For each data word that does not equal zero (i.e. contains at least one bit 1, therefore at least one hit), the hits are recorded: for each of the bits set to 1, the running index of the data word is written to memory as time-index, along with the position of the bit as channel number. As has been explained above, the DAQ process must not be interrupted by other processes, but since disk access might interrupt the DAQ process, the event data constructed in memory cannot be written to hard-disk directly. Instead, the DAQ is cleanly shut down periodically (e.g. every ten minutes), and is automatically restarted only after the data is safely written to disk.

Besides the problems encountered in the implementation of the DAQ computer hard- and software, also one principal downside of a clock driven system should be kept in mind. As the system polls the state of each input channel once every DAQ clock cycle, the time the state of the input channel reads *"photon arrived"* is important. If the state is reset too soon, the event might be missed if the timing is unfavourable. Conversely, if the state is kept for too long, it might be seen in more than one DAQ cycle, appearing as two (or more) successive events. For this reason the TTL pulses, which are only 20 ns long when they are sent out by the SPAD modules, are electronically stretched to a duration of $\tau = 1/f_{\mathrm{DAQ}}$.

If two (or more) photons are detected within a timespan shorter than τ, the same reason requiring a pulse stretcher can let the DAQ miss all photons but one. The probability for this occurring at a given photon-rate can be derived from Poisson-statistics and be straightforwardly corrected[39] for in a light-curve (see Chapter 4.3). However, as this correction scales the noise as well as the signal, the SNR[40] decreases, compared to the same measurement without pile-up.

[37] Real-Time Operating System
[38] Direct Memory Access
[39] For measured photon rate r and a cycle time τ, the corrected photon rate R is

$$R(r) = -\frac{1}{\tau}\ln(1-\tau r) \qquad (4.3.8)$$

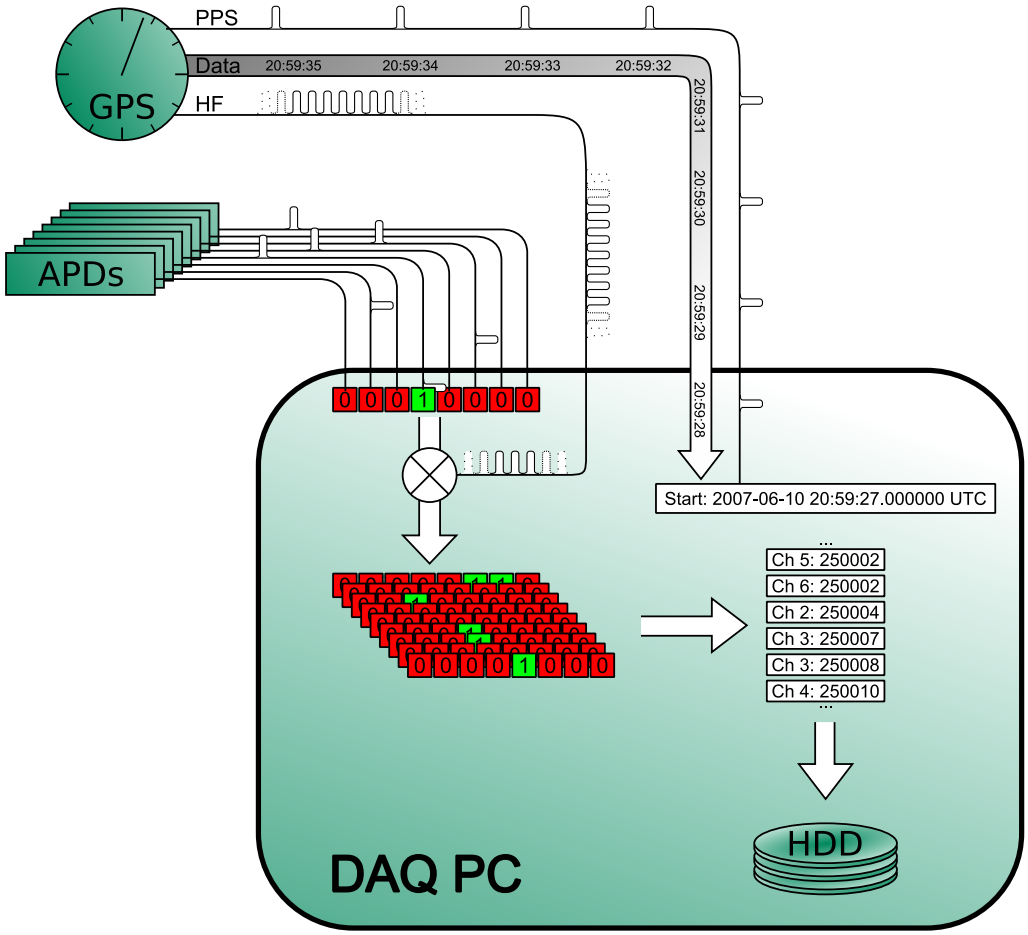

Figure 2.14.: Schematic of the PC-based "old" DAQ system used by OPTIMA. The DAQ is clock driven, i.e. at each clock cycle, the DAQ takes one sample, filtering events out of the time-stream in a later step.

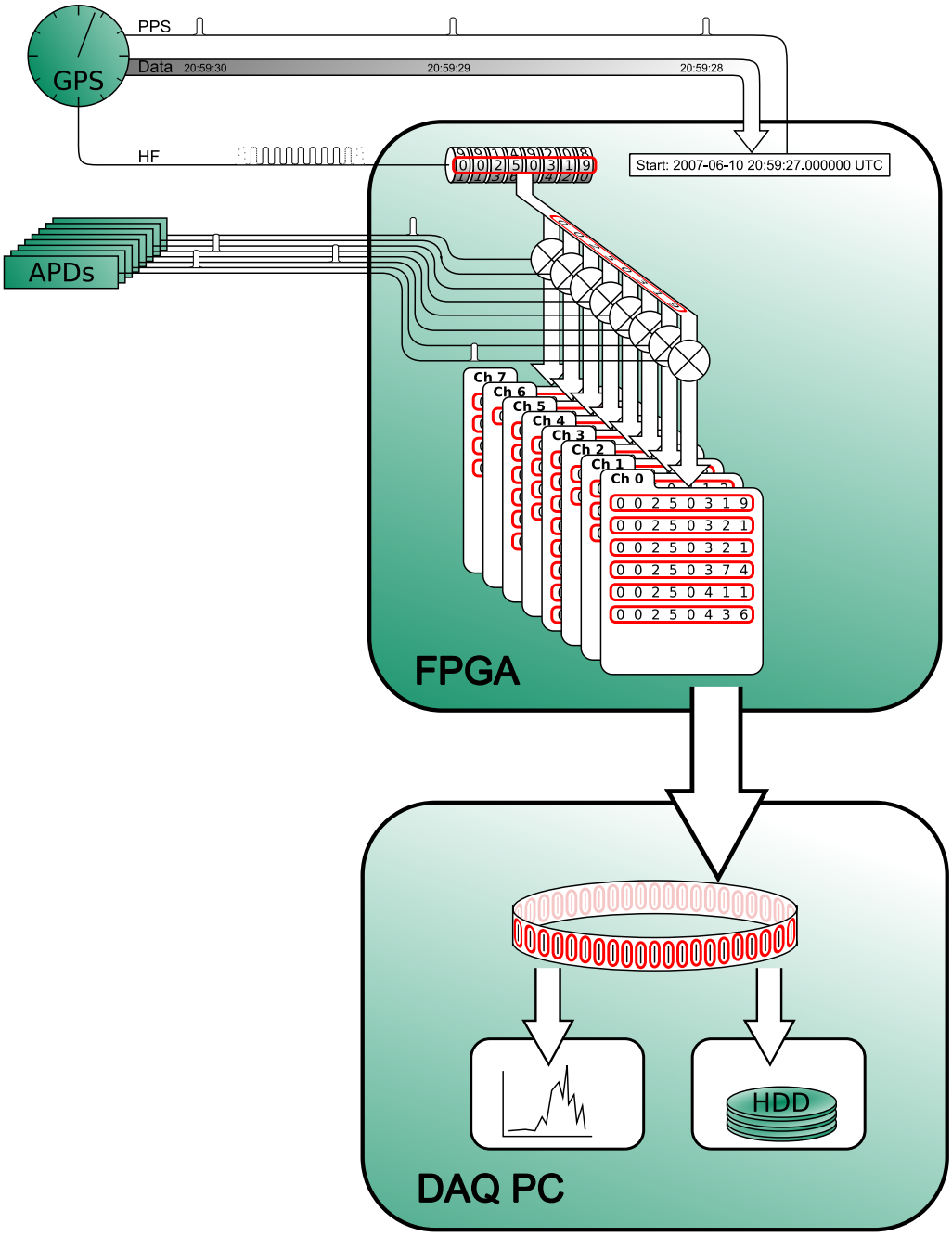

Figure 2.15.: Schematic of the FPGA-based "new" DAQ system used by OPTIMA. The DAQ is event driven, i.e. for each photon event reaching the DAQ, the clock counter is saved. By implementing the time-tagging in hardware (FPGA), reaction time critical tasks are separated from merely throughput critical tasks

2.5.2. The Next-Generation OPTIMA DAQ System

While the system described in section 2.5.1 is an easy and cost-effective solution to the problem of *acquiring data*, it does suffer from several defects, some only slight problems of this implementation, some inherent in the DAQ scheme used.

The first problem is one of lack of stability. The system aggressively manages it's own memory to reduce reaction times. Since the operating system used as a base for the DAQ application, Microsoft Windows 98, has poor memory protection, this can result in data corruption on rare occasions.[41] As the DAQ system relies on the possibility of direct access to the hardware from unprivileged processes, the obvious remedy, using a more modern operating system with effective memory protection as base for the DAQ, is not trivial.

The rather dated architecture of the whole system is posing progressively more problems over time. The old software used by the system is not always adequately compatible with modern hardware, and hardware compatible to some of the integral pieces of the DAQ system is becoming hard to get.

The next major disadvantage of the original OPTIMA DAQ system is a lack of on-line analysis functionality. The only feedback of the running observation provided to the observer is a numerical rate-meter display. However, as the reaction-time limited process of time-tagging is performed on the same system as the only throughput limited process of more sophisticated on-line data analysis, a more sophisticated data analysis is sacrificed for more safety of operation.

It would be highly advantageous if a light-curve of the observation were plotted on the screen while the observation is running. This would enable the observer to quickly assess changes in observational conditions and react correspondingly. Additionally, more sophisticated analysis routines are desirable as well. For example, an on-line FFT[42] power spectral density plot might warn the observer of wind-shake related problems, or an ad-hoc analysis of the polarization state could indicate a thin layer of cirrus clouds.

These reasons led to the development of a completely new DAQ system from scratch. From the lessons learned using the old system, two main design goals were decided upon, around which the new system was developed:

Consistent separation of reaction-time limited tasks from throughput-limited tasks
Shifting reaction-time critical tasks into dedicated hardware allows more sophisticated operations in the part of the system dedicated to throughput-limited operations, as the throughput-related limits imposed by modern computer systems are orders of magnitudes less severe than reaction-time related limits.

Consistently modular software design A separation of the overall DAQ functionality into smaller independent modules with well-defined interaction points facilitates future changes to the DAQ system, since future developers only need to adhere to the correct usage of interaction points when changing or adding a module, instead of requiring in-depth understanding of the inner workings of the whole DAQ software.

The first of the above points mostly influences the design of the new DAQ hardware, while the second point drives the software development paradigms. Fig. 2.15 shows an overview over the workings of the new hard- and software.

---

[40] Signal to Noise Ratio

[41] A data analysis tool to detect the resulting corrupted files has been developed. The corrupted data is either corrected or dropped from the file.

[42] Fast Fourier Transform

Hardware

Assigning the arrival time tag to a detected photon is the most time-critical task to be performed by the DAQ system: each arrival of a new event has to be processed before a new DAQ cycle begins. This requirement of reaction-time is in contrast to the rest of the time critical tasks in later data acquisition or analysis steps, where a backlog of events can be processed after some delay by a spurt of activity. There (within limits), only the *average* processing speed is important. As time-slicing on modern multi-tasking systems imposes frequent delays on user processes which are offset by high computing speed, software running on a multi-tasking OS[43] is not well suited to perform the time-tagging. While a CPU[44] running only the DAQ process is capable of guaranteeing quite short reaction times, modern FPGAs[45] are extremely well suited to simple tasks like time-tagging, offering an advantage in speed of orders of magnitudes at comparable development complexity.

The clock driven approach taken in the PC-based DAQ system is well suited for implementation in a general-purpose CPU. It entails complex processing of structured data ("*If* data is nonzero, *then* select all channels containing a non-zero bit, *loop* over those channels, *copying* the channel data and the running index."). This complex behaviour using loops and data manipulation is inefficient and difficult to implement as logic. However, other operations are very cheap to implement directly as boolean logic: e.g. counting, triggering and blind data copying. With these building blocks, the task of assigning a time tag to an event can be re-formulated in an event-driven way: A counter is continuously incremented by the pulses from the GPS-disciplined oscillator. The arrival of an event triggers a copying of the current counter-value to a memory buffer, effectively saving the time-tag.

Once the event time-tags are buffered, all other tasks remaining to be performed are not reaction-time limited any more. Therefore, the complications arising from housekeeping tasks like managing the fill-level of the individual buffers, or data transmission to a receiving computer do not limit the timing performance of this system. Another advantage of creating the time-tags event-driven is that it is possible to have more than one event with the same time-tag, effectively eliminating the problem of event pile-up discussed in section 2.5.1.

After one failed attempt of developing a DAQ system based on this design, a new hardware setup implementing this DAQ scheme is currently under development.

Software

As mentioned in section 2.5.1, the current DAQ suffers from a number of limitations, some of which stem from the software architecture. In anticipation of a new DAQ hardware, a software framework was developed within the scope of a master's thesis supervised within this work [Duscha, 2007].

To achieve the goal of a modular system as stated above, it was decided to split the functionality into the two distinct domains of data reception from the DAQ hardware, and data processing. While receiving data is a singular task, one can think of a huge variety of useful ways to process the data, besides saving the data to disk. Therefore, the design was based on a client/server architecture: There is one single data server that provides the DAQ hardware's data to an arbitrary number of clients.

[43] Operating System
[44] Central Processing Unit
[45] Field-Programmable Gate Arrays

Continuing the client/server analogy, a point-to-point link from the server to each client would be the obvious solution to transmit the received data to the clients. While this relatively simple implementation is the basis for many client/server systems (e.g. the WWW[46]), it is clear that n point-to-point connections are very inefficient, if each client will receive the same data and the amount of data that is to be transmitted is large.

In this scenario, a solution that works analogously to a broadcast has an obvious advantage. In IPC[47], this can be achieved by using shared memory for communication. However, as shared memory works by disabling memory protection between several processes for specific regions of memory, it becomes the programmer's responsibility to ensure data integrity during concurrent access. This is usually achieved by blocking access for all other processes to the shared memory segment while one process is writing into it, and by blocking writing access for all other process while at least one process is reading from it.

In most applications, this is the best solution. While not trivial to implement – deadlocks have to be carefully avoided – it does guarantee data integrity at the cost of a moderate increase in latency and decrease in throughput. In the case of the OPTIMA DAQ, this solution suffers two major disadvantages, that led to the development of a different, lockless approach.

Firstly, the arrival of photons cannot be blocked. While the arriving events can be buffered in an extra memory until an existing lock is released, this introduces an additional copy-step that further reduces throughput. Secondly, and more importantly, locking is a cooperative process. The lock has to be actively released by the locking process, and a single mis-behaving process can crash the whole DAQ. As one major design goal of the new DAQ was easy extensibility *without* having to fully understand the internal workings of the complete system, fail-safety is of prime importance. In this context, the possibility of a single faulty client stopping the rest of the software from working needs to be minimized.

The solution developed for the next-generation OPTIMA DAQ drops the concept of data integrity guarantee. Instead, a guaranteed detection of corruption is offered. In practice, this amounts to the same thing: If there are not enough resources to achieve the required throughput, the data acquisition will fail at some point, and if the possible throughput is high enough, all data being saved is guaranteed to be correct.

The major difference to the implementation of a client is that the client cannot assume all data it receives to be correct. It must check for a notification of corrupt data, and react accordingly. The correct reaction depends on the kind of client. A hard-disk write client might notify the user of insufficient throughput and either stop the observation, or continue with gaps in the data. A calculation intensive online data-analysis client might warn the user that not enough resources are available for the client to be reliably run. This client might then cease operation, thus freeing resources for the rest of the clients.

Reliable detection of data corruption due to the server process, which writes into shared memory, overtaking a client process (which only reads from memory) is guaranteed by keeping a journal of intended actions alongside the data buffers in shared memory. This journal, called *memory map*, consists of a single integer number per event word. This number is increased by the server for a whole block of memory before beginning to write into this block, and then increased again, after the server is finished writing.

The LSB[48] of the memory map entry can be used as a busy-flag, signifying the memory is

[46] World Wide Web
[47] Inter-Process Communication
[48] Least Significant Bit

not safe to read. Additionally, all higher bits of the memory map entry can be interpreted as a counter of the number of times this data entry was written to. By checking the LSB of the memory map entry corresponding to a data buffer cell before attempting to read, and then comparing the memory map entry before the read and after the read, the client process can reliably detect whether the memory it just read was invalidated by the server process during the read.

As proper shared memory organization and correct usage of the memory map by both the server as well as the clients are not trivial, but essential for the correct workings of the DAQ system, they have been encapsulated in a library that can be used by future programmers working on the OPTIMA DAQ. This framework isolates the programmer from the details of the inner workings of IPC [Duscha, 2007].

The author of a new server is provided with a set of functions to set up and configure the shared memory, and to warn clients of access to a specific range of buffer. To the server-programmer, the functions to warn the clients look very similar to the well known functions for memory allocation – the programmer does not need to know how the memory he requests for writing is organized, it is just memory.

Conversely, the developer of a new client is provided with routines to correctly access the shared memory, read the DAQ configuration, and check whether a segment of buffer is safe to read, or was invalidated while reading. Similarity to the server routines, the functions localizing the next safe buffer segment, and the safety check after reading look like normal memory management routines – the client developer also does not need to know how the memory is organized, he just works with memory.

In addition to the high-throughput IPC organized like a broadcast in form of shared memory, a secondary point-to-point communication channel between the server and each client is established by the framework. Through this channel, the client can access statistics and meta-information from the server, and client and server can exchange commands.

3. The OPTIMA-Burst Instrument

OPTIMA is a very flexible and mobile instrument that can be mounted on a wide variety of telescopes (see chapter 2). In OPTIMA-Burst, some of this flexibility is traded for better performance for one specific application: Observation of transient sources with OPTIMA. To make this possible, OPTIMA was closely tied into the control system of a specific telescope, the 1.3 m SKO telescope. While many of the adaptations are beneficial also when using OPTIMA at other telescopes, OPTIMA-Burst is far more capable at SKO.

3.1. Telescope Control

As described in 2.2.2, OPTIMA is an aperture photometer, i.e. the (photometry or polarimetry) aperture of OPTIMA needs to be positioned onto the target. Considering the diameter of the OPTIMA apertures ($\sim 6''$ on the sky) and typical FWHM of the seeing at SKO ($1''$-$2''$), it is obvious that control over the telescope pointing is needed at the arc-second level or better. However, as most astronomical instruments have imaging capability with at least a few arc-minutes FoV, the *open-loop* pointing accuracy of most telescopes is of the order of tens of arc-seconds. Of course, telescope movement can be controlled much more accurately than this by the TCS[1] when moving the telescope by relative offsets. This fine control using relative movements lends itself to *closed-loop* positioning.

One example of closed-loop positioning used in telescope control is the autoguider: While equatorial mounted telescopes need to be moved in only one axis (aptly called the hour axis) to perform sidereal tracking, slight errors in tracking speed and alignment of the hour axis with the celestial pole lead to accumulation of pointing error. Furthermore, the mechanics of hour axis drive can introduce periodic errors. The situation in telescopes with alt-az mount is even more difficult, as sidereal tracking requires tracking in two axes (altitude and azimuth) for non-imaging instruments, or three axes (altitude, azimuth and field rotation) for imaging instruments. While the mechanical precision of modern telescope mounts is very good and the errors incurred are minimized, they cannot be neglected for long term exposures. In imaging instruments, point-sources are smeared out to lines, while in non-imaging systems like OPTIMA, the source exits the instrument aperture.

An auto-guider is a system to actively compensate the tracking errors. By periodically taking images of (one or more) guide star(s), an auto-guider continually measures the current pointing direction of the telescope to sub arc-second precision. It calculates the movement offset necessary to correct the actual pointing direction to the set-point, generates an appropriate movement command, thereby creating a closed feedback loop.

In OPTIMA-Burst, the closed-loop positioning principle is extended from guiding the telescope during observation to positioning the source automatically.

[1] Telescope Control System

3.1.1. Skinakas Observatory TCS

The 1.3 m telescope of SKO, built by DFM Engineering, is a Ritchey-Chrétien telescope on an equatorial horseshoe mount. The mount is computerized using a TCS by DFM Engineering. The TCS controls all aspects of motorized telescope movement: Automatic slewing to targets, manual slewing at various speeds, sidereal tracking, focusing and ensuring pointing constraints. It is based on a standard PC with several controller cards and external motor controllers. The TCS software runs natively (i.e. without additional OS) on the CPU, in effect working as its own RTOS. This is necessary, as various control tasks operate in parallel and need predictable timing.

The TCS computer is the main user interface. Here, the status of the telescope is displayed and the telescope can be moved to the next target. Both absolute celestial coordinates (*SLEW* command) as well as relative movements (*OFFSET* command) can be entered. The TCS automatically controls the movement speed ramping up to a fast speed for large movements and approaching the target coordinates at slow speed. The TCS gives feed-back when the target pointing is reached and becomes stable.

In addition to the TCS computer interface, the TCS offers two hand-paddles (one in the control room and one at the telescope) for more direct control. Via the hand-paddle, the operator can move the telescope pointing and focus in two pre-set speeds. While the hand-paddle does not directly control the telescope motors, the TCS RTOS provides a negligible latency, and additionally offsets the radial screw clearance.[2]

As performing small pointing offsets with minimal latency is best done via hand-paddle, the SKO autoguider is interfaced to the hand-paddle on the telescope floor.

3.1.2. TCS Connection

In addition to the computer console interface, all functions of the TCS can be controlled remotely via serial interface using the EXCOM protocol. Besides a duplication of the TCS control interface at the OPTIMA-Burst control, software was written to interface the *XEphem* [Downey, 2005] sky atlas software to the telescope (Fig. 3.1).

The close integration of a sky atlas into the operation of the telescope has proven to be much faster and less error-prone in the operation of the telescope. Instead of planning an observation and writing down the coordinates, moving the telescope to the new target by entering the coordinates manually at the TCS keyboard, and then trying to identify the field visible in the first short CCD exposures with the help of printed finding charts (with the associated uncertainty about the actual orientation and scale), now the target is selected from a database and the telescope moved with one mouse-click. The sky-atlas itself serves as finding chart, with the correct orientation and scale. The *XEphem* installation used in OPTIMA-Burst uses the USNO[3] catalogue (limiting magnitude 19 mag) and can download overplot DSS[4] plates directly in the atlas, also at the correct orientation and scale.

Correct focusing is critical for OPTIMA, as de-focussing can lead to light spilling over the fibre or polarimetry aperture. As the image of the target moves in the focal plane with atmospheric seeing, this not only introduces light-loss, but also an additional source of noise. For best results, the telescope focus should be determined at the beginning

[2] The radial screw clearance leads to a smaller movement after a change in the movement direction, due to the play between screw and cog-wheel of the drive.
[3] US Naval Observatory
[4] Digitized Sky Survey

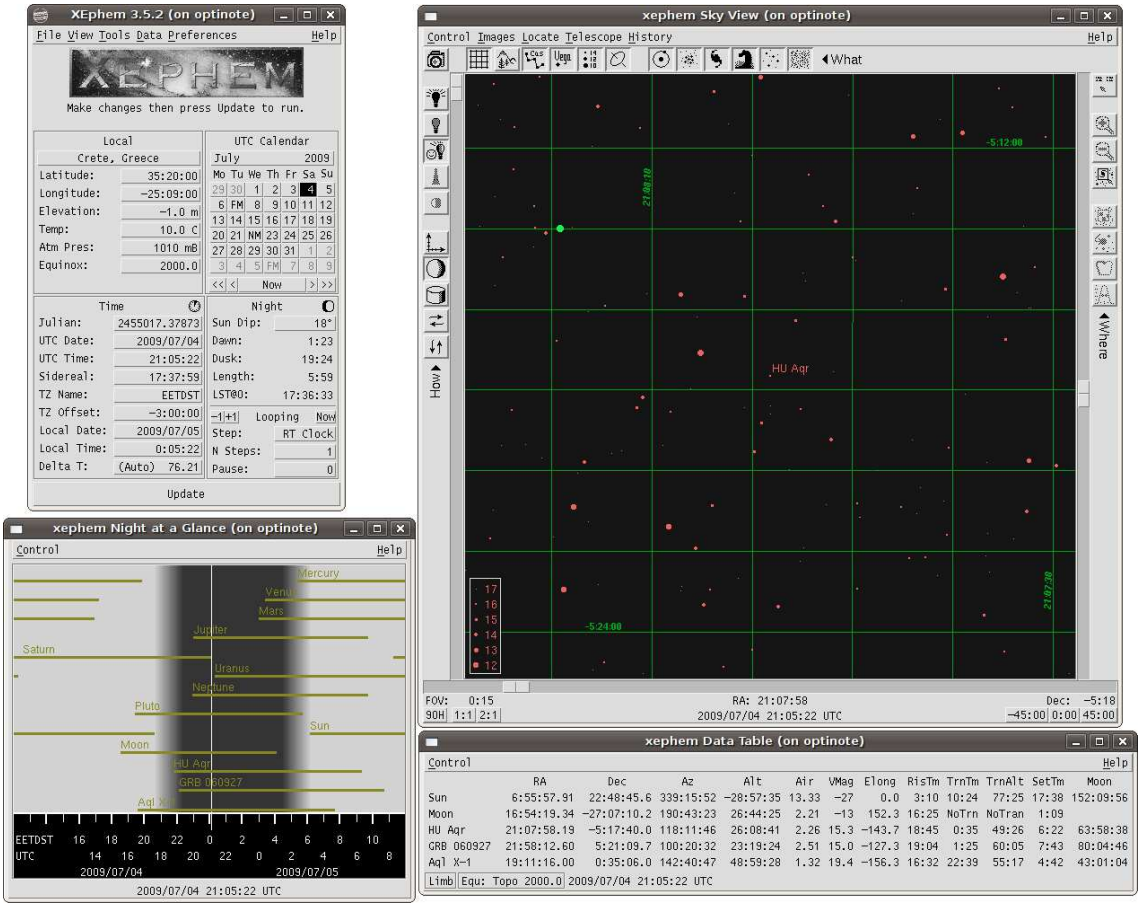

Figure 3.1.: Screenshot of a typical OPTIMA-Burst *XEphem* session

of every night and checked repeatedly during the course of the night, if the observing conditions (especially temperature) change significantly. To make frequent focus checks feasible without a significant loss of observing time, the TCS EXCOM interface was used to implement an auto-focus routine (Fig. 3.2).

The autofocus routine takes exposures at adjustable focus encoder positions. In order to minimize systematic errors introduced by changes in seeing, the order of focus positions is randomized.

The auto-focus software automatically evaluates the FWHM of a suitable star and fits the FWHM with a quadratic regression. The minimum of the fitted function is suggested as new best focus, and the user can interactively add further exposures at more focus positions to improve the fit, or use the fit value. The autofocus-software also allows to save focus values for later use and quickly switch between the correct focus for OPTIMA and for the rest of the SKO instrumentation.

3.1.3. Tertiary Mirror Control

In addition to the telescope functions controlled by the TCS, the telescope is equipped with a moveable tertiary mirror that reflects light to the SKO instrumentation if it is placed in the optical path. As the tertiary mirror was not foreseen in the DFM TCS, an additional motor controller and SKO provided control software exists. This software can be remote-

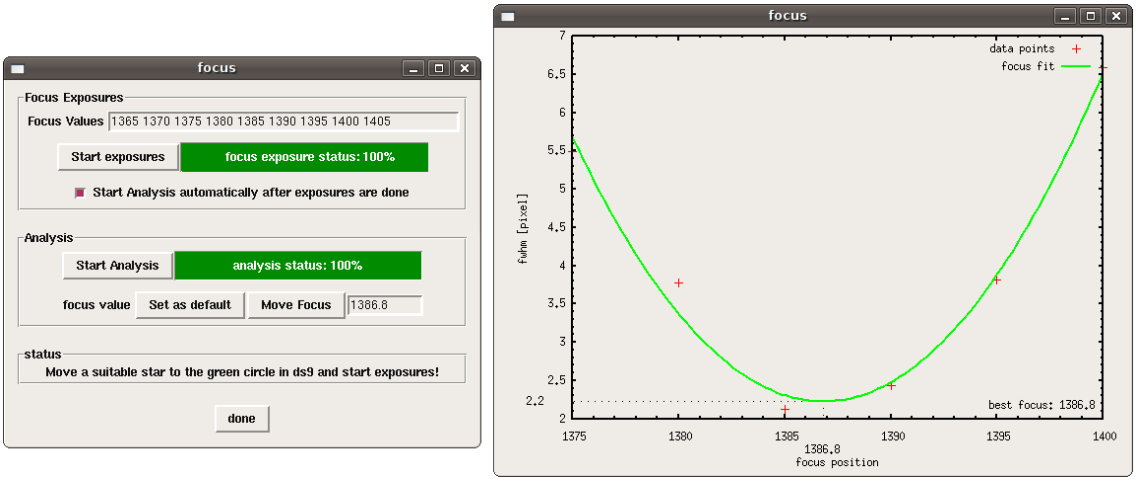

Figure 3.2.: Screenshot of the OPTIMA auto-focus routine.

controlled by network commands from the OPTIMA-Burst software. The tertiary mirror is automatically moved out of the optical path when an automatic OPTIMA observation starts.

3.1.4. Fine Control

In order to build a closed-loop positioning system for OPTIMA, more direct control over the telescope movement than offered by TCS remote control using EXCOM commands is needed. The hand-paddles of the TCS offer an ideal control mechanism for this: When one of the cardinal direction buttons of one of the two hand-paddles is pressed, the TCS disengages its normal sidereal tracking and moves the telescope in the indicated direction. The TCS controls the motor speed of both the right ascension and declination axes in such a way, that apparent slew speed is identical in the four cardinal directions. The actual slew speed is configurable in the TCS software. The TCS also offsets any radial screw clearance of the telescope drive, i.e. when reversing the direction of a slew movement, the TCS moves the drive motor an appropriate additional distance, so that a telescope movement always has the expected distance, regardless of the recent "history" of the drive.

With these prerequisites, telescope movements accurate to the limit of the telescope mechanics can be performed by accurately timing button presses of the hand-paddle. For this purpose, a hardware timer box was developed for OPTIMA-Burst, which receives timing commands via USB[5] from the OPTIMA control PC, and uses a MCS-51 based micro-controller to control solid state relays, which simulate button presses on the hand-paddle. The timer box uses an internal quartz oscillator with 50 ppm stability as clock, thereby providing a time-base with far better accuracy than what could be offered if the relays were controlled directly from the PC software. As the timer box can also operate as simple relays box, it has several additional channels controlling the shutter motors and fiducial lights of the OPTIMA field-view unit.

In order to use timed button-presses on the hand-paddle as accurate movement commands, the movements of the telescope in response to the hand-paddle need to be calibrated. This is performed in the software controlling the timer box. The software can be

[5]Universal Serial Bus

configured by setting the measured distance the telescope pointing moves in arc-seconds in both axes, when one directional button is pressed for a specified amount of time. The software does not assume that both axes are perfectly orthogonal, so any axis misalignment can be calibrated. Radial screw clearance of the telescope drive can also be configured and will be corrected, but in practice the TCS does already adequately compensate for this. Also, several years of experience with this setup have shown that the axis calibration is very stable in time. As long as care is taken to align the OPTIMA CCD rotation so that the declination axis is vertical and north is up, no re-calibration of the drives is necessary.

The pointing accuracy is limited using this set-up by the telescope mount. Movements smaller than $\sim 0.5''$, corresponding to button presses shorter than ~ 100 ms can introduce oscillations in the telescope mount, which dominate the total positioning error for small movements.

3.1.5. Pointing

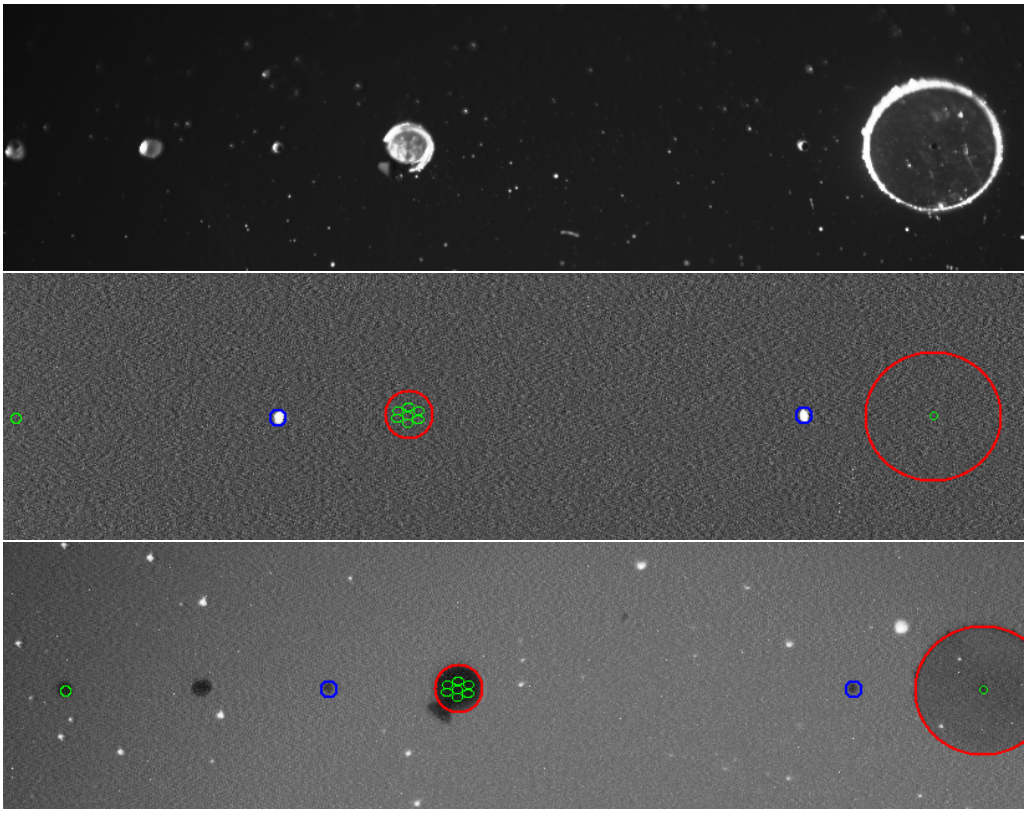

Figure 3.3.: Fiducial lights used to offset internal alignment drifts. At the beginning of a campaign, the slanted mirror is illuminated from the side so that the fibre and polarimeter apertures become visible (top). In the same pointing, the position of the fiducial lights is determined, and all positions are saved (middle). During observations, the fiducial lights can be used to automatically calibrate the current position of all apertures in the field (bottom).

In order to facilitate quick positioning of a target onto the OPTIMA aperture and to avoid operational errors leading to mis-pointing, the OPTIMA-Burst software allows

automatic target positioning. For this, the target and a suitable guide star are chosen interactively with a mouse-click, the software moves the telescope automatically to point the target onto the OPTIMA aperture, tracking the guide star.

In order for this to work, the OPTIMA software needs to know precisely where each OPTIMA aperture is located in respect with the CCD FoV. The various apertures used in OPTIMA (seven photometry apertures in the hexagonal bundle, polarimeter aperture, spectrometer aperture and background fibre) can be seen in CCD images, if the illumination is adjusted accordingly. As the geometry of the apertures is known, their positions in a CCD frame can be recorded. However due to mechanical flex in the optical setup, position shifts of the order of a few tens of μm, i.e. a few pixels can occur, if the mechanical load on OPTIMA changes. While this has been greatly mitigated in the OPTIMA-Burst setup compared to the previous OPTIMA setup, the shift can be non-negligible for slews of more than 30°, depending on the pointing direction.

To measure and compensate the position shift of the CCD, two LEDs have been incorporated into the slanted mirror as fiducial lights (see Chapter 2.2.2). After a large telescope slew, the new position of each aperture is automatically determined by closing the shutter, turning on the fiducial lights, and exposing a short CCD frame, tasks also controlled by the timer-box. Once the current position of the selected aperture has been calibrated, the movement vector to move the target onto the aperture is computed, and applied to the guide star[6]. The correct telescope movement is executed, either via precise timer-box controlled hand-paddle presses for short movements, or using higher speeds under TCS control for larger movements. After the movement, a new CCD exposure is taken, and the movement actually executed by the telescope is evaluated by determining the position new of the guide-star, and a new movement vector is computed. With each iteration, the target is moved closer to the aperture, until it is centered stably on the aperture after a few iterations.

3.1.6. Guiding

After the telescope pointing stabilizes, data taken by OPTIMA is considered reliable (*good-time* start). In order to keep the unavoidable sidereal tracking errors from accumulating and letting the target drift from the OPTIMA aperture, constant closed-loop control of telescope pointing, called *guiding* is required.

Ideally, the time constant of the guiding regulation loop (exposure of an image, position analysis, telescope movement) is as short as possible. Usually, the time constant is limited by the acquisition time of a new image, i.e. the exposure time plus the time required to transfer the image from the guiding sensor to the computer. The exposure time is limited by the necessity to achieve a sufficiently high SNR in the guide star. At a 1.3 m telescope like the SKO, most often there is at least one star in the FoV bright enough to allow exposure times shorter than 5 s, so the regulation time constant is often dominated by the read-out and transfer times. Therefore, reading out only a small window surrounding the guide-star is beneficial.

For a non-imaging instrument like OPTIMA, the data taken by the guider is a valuable diagnostic tool: Sky transparency, cloud cover, seeing conditions and sky background can all vary on time-scales of minutes during an observation night. These changes are not always easy to interpret in the raw OPTIMA data, but are readily identifiable in a CCD image. In order to make the guider images as helpful as possible in assessing the

[6] As the actual target is hidden from the CCD camera by the aperture, the target itself cannot be used for position analysis.

OPTIMA data, it is helpful to analyze a large FoV surrounding the target, and to have a reasonable SNR even for fainter sources. Obviously, this conflicts with the goal of keeping the regulation time-scale as short as possible.

In order to have both a short guider regulation time-scale and as good diagnostic CCD data as possible, OPTIMA-Burst uses two independent systems. After good-time start, guiding control is handed over to the SKO guider that is also used for all other SKO instruments. To avoid telescope drift while the SKO guider is acquiring a suitable guide-star, OPTIMA keeps the pointing loop locked until the SKO guider has locked its guiding loop. After handing guiding control to the SKO guider, OPTIMA continues to take short full-frame exposures (standard exposure time 10 s, typical cadence $11 - 14$ s). The OPTIMA pointing software analyzes the short exposures on the fly, warning the operator about a loss of guider lock, e.g. due to passing clouds. In addition to saving the on-line analysis results, all images are compressed and archived for later analysis at the end of an observation night.

While pointing control is handed over to the SKO guider during a normal observation, the OPTIMA pointing lock is still kept. This allows to re-engage the OPTIMA pointing loop at any time. As the OPTIMA-Burst pointing loop has a larger FoV than the SKO guider, this can make re-acquisition of a lost target (e.g. after a passing cloud) much quicker and less error-prone.

It is also possible to manually tune the locked position by an offset too small for the usual slew precision and re-engage the OPTIMA-Burst pointing loop. While the pointing cannot be kept stable with this accuracy for the aforementioned reasons, the mean of the pointing can be very accurately controlled. This technique can be used to map extended sources with an OPTIMA aperture, e.g. to map the polarized background of the Crab nebula surrounding the Crab pulsar.

3.1.7. OPTIMA-Burst Control Center

The addition of new features and automation in OPTIMA-Burst potentially make OPTIMA operation more complex and hence more error-prone when operated during long night-time shifts. In order to keep operation as simple as possible, a unified "control center" type software was developed. An example session using the OPTIMA-Burst software is shown in Fig. 3.4.

The control software is centered around the *SAOImage ds9* [Joye and Mandel, 2003] fits[7] viewer and a control window for the CCD camera. From the CCD control window, most functions of the SKO TCS and all aspects of CCD operation like thermal control and setting of meta-data can be controlled. In this window also acquisition of new images and automatic displaying of new images in *ds9* is triggered.

Transparently to the operator, the control center queries the current telescope pointing direction from the TCS and writes it into the fits header of the new image. The control software has access to the full USNO-A2.0 catalogue [Zacharias et al., 2004] saved locally on hard-disk. After extraction of point-sources from the image using SExtractor [Bertin and Arnouts, 1996], it uses the TCS pointing direction and USNO catalogue to fit a WCS[8] of the frame with the *WCSTools* software package [Mink, 2002], i.e. the pixel coordinate system of the CCD frame is linked to celestial coordinates.

Using the WCS and the USNO catalogue, the positions of all sources found in the catalogue for the FoV of the image are marked "live" in *ds9*, together with all point sources

[7] Flexible Image Transfer Format
[8] World Coordinate System

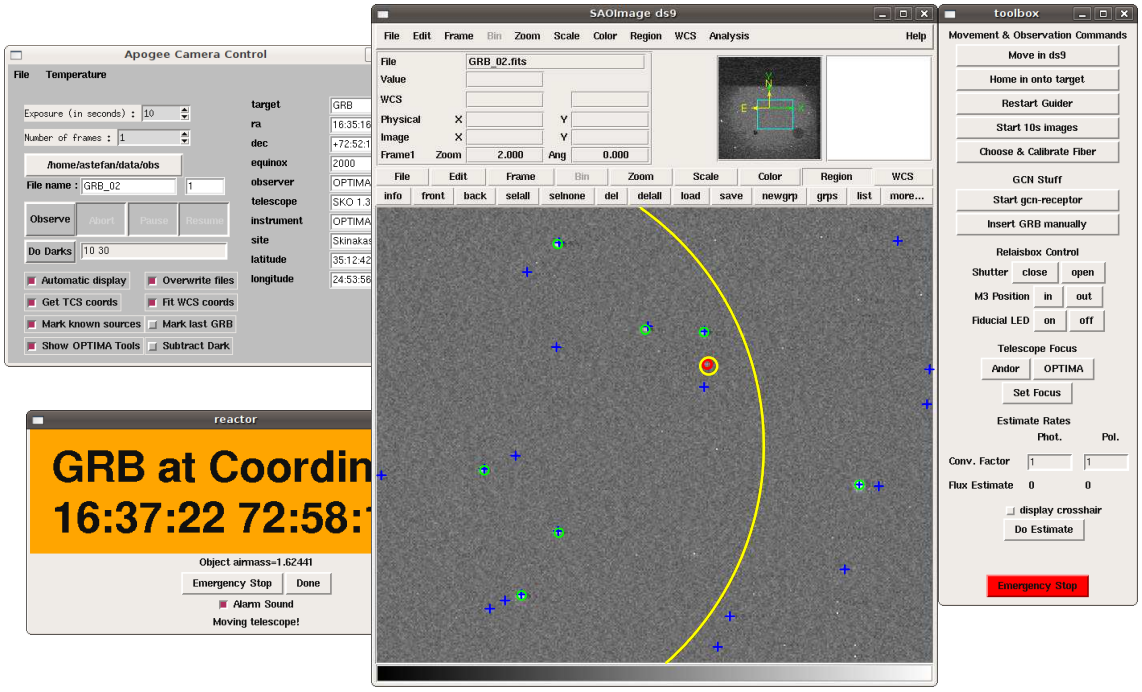

Figure 3.4.: Screenshot of an OPTIMA-Burst observation session, showing a GRB trigger. The categorisation of detected sources can be seen. Blue crosses: catalogue sources. Green circles: Identified sources. Red circles: Unidentified sources. Overplotted as yellow circles, two Swift error-circles can be seen.

extracted from the image. The control center tries to identify sources extracted from the frame by comparison with the catalogue. Sources that can be identified are marked in a different colour (green) than unidentified sources (red). The control center software also tries to identify transient sources, i.e. sources that either changed their brightness with respect to the catalogue or with respect to previous images.

The control center also provides the interface to most aforementioned software functions, e.g. the OPTIMA auto-focus, the guider or the closed-loop positioning software. Target and guide-star can be interactively selected in *ds9* by clicking on a star. This coordinate selection by the operator does not need to be done with great precision, as the software automatically finds the centroid of the selected star. For very dim sources that may not be visible in the CCD frame and can only be identified by their position in relation to nearby brighter stars or by their celestial coordinates, this centroiding feature can also be turned off completely.

3.2. GRB Response Automation

The main goal of the "*OPTIMA-Burst*" additions to OPTIMA is to facilitate observation of GRB afterglows. GRBs are compact objects, hence can be expected to show variability of intrinsically short time-scales[9]. After the explosion of a GRB, an expanding fireball is formed which expands and decays with a power-law in time. As the OT[10] becomes

[9] However, the intrinsic time-scale is slowed by the redshift, which can be quite high for GRBs
[10] Optical Transient

ever harder to observe with diminishing brightness and the expected time-scales become ever slower with the expansion of the fireball, the necessity of as short a reaction time as possible between initial burst and start of OPTIMA observations is obvious.

3.2.1. GCN Connection

In order to receive notifications about current GRBs, OPTIMA-Burst uses the GCN[11]. The GCN [Barthelmy, 2005] consists of two separate systems. One system, the GCN *Notices*, is an automated system to disseminate GRB (and other high-energy transient) detections in a fast and automatic fashion. The other system, GCN *Circulars*, is a mail-exploder system to facilitate communication between world-wide GRB observer groups.

The GCN has its roots in the BACODINE[12] system, which was a system to calculate and distribute burst coordinates of GRBs detected by the BATSE[13] instrument aboard CGRO[14]. BACODINE also distributed GRB coordinates for other satellite missions, and with the de-orbit of CGRO, the name of BACODINE was changed to the more general GCN Notices. Currently, the GCN distributes real-time GRB information from INTEGRAL[15], RXTE, *Wind*[16], *Fermi*-GLAST[17] and *Swift* – with by far the greatest number of triggers supplied by *Swift*.

The GCN *Notices* service collects GRB trigger information from the ground-segment of all connected satellite missions centrally in a computer center at the NASA Goddard Space Flight Center. For some missions, data is downloaded only a few times per day during ground station passes, while some missions (notably *Swift*) are connected continuously via the TDRSS[18] satellite network. GRB trigger information is brought into a standard format, and distributed to all ground stations interested as email or pager message. Using a dedicated protocol, the notices can also be sent directly to computers via internet in a machine-readable way. As the library functions that allow this kind of network connectivity are based on the POSIX[19] `socket()` system-call, this is called the GCN *socket* delivery method. This allows GRB observers to automate afterglow observations.

The GCN *Circulars* email exploder is used by the GRB community as a very fast communication medium, akin to the "*Astronomers Telegram*" of the wider astronomical community. Preliminary results are published without a referee process and sent out per email in order to inform GRB groups worldwide of developments of GRBs as they happen, and trigger further follow-up observations of interesting sources. For some GRBs, a final in-depth Circular with fully analyzed data called a GCN *Report* is sent at a later date. Similar to the Astronomers Telegram, GCN *Circulars* are archived[20] automatically on the internet. A number of OPTIMA-Burst results gave been published as GCN *Circulars*.

During OPTIMA-Burst campaigns, OPTIMA is connected as GCN socket site using the name `OPTIMA_s`. The OPTIMA-Burst GCN receptor software monitors the socket connection, and classifies all incoming GCN Notices according to visibility and source history. Sources that fundamentally cannot be observed, e.g. because they are located at

[11] GRB Coordinate Network
[12] BATSE Coordinate Distribution Network
[13] Burst and Transient Source Experiment
[14] Compton Gamma-ray Observatory
[15] International Gamma-Ray Astrophysics Laboratory
[16] The name of the Wind spacecraft is, like Swift, one of the few non-acronym satellite names
[17] Gamma-Ray Large-Area Space Telescope
[18] Tracking and Data Relay Satellite System
[19] Portable Operating System Interface for Unix
[20] `http://gcn.gsfc.nasa.gov/gcn3_archive.html`

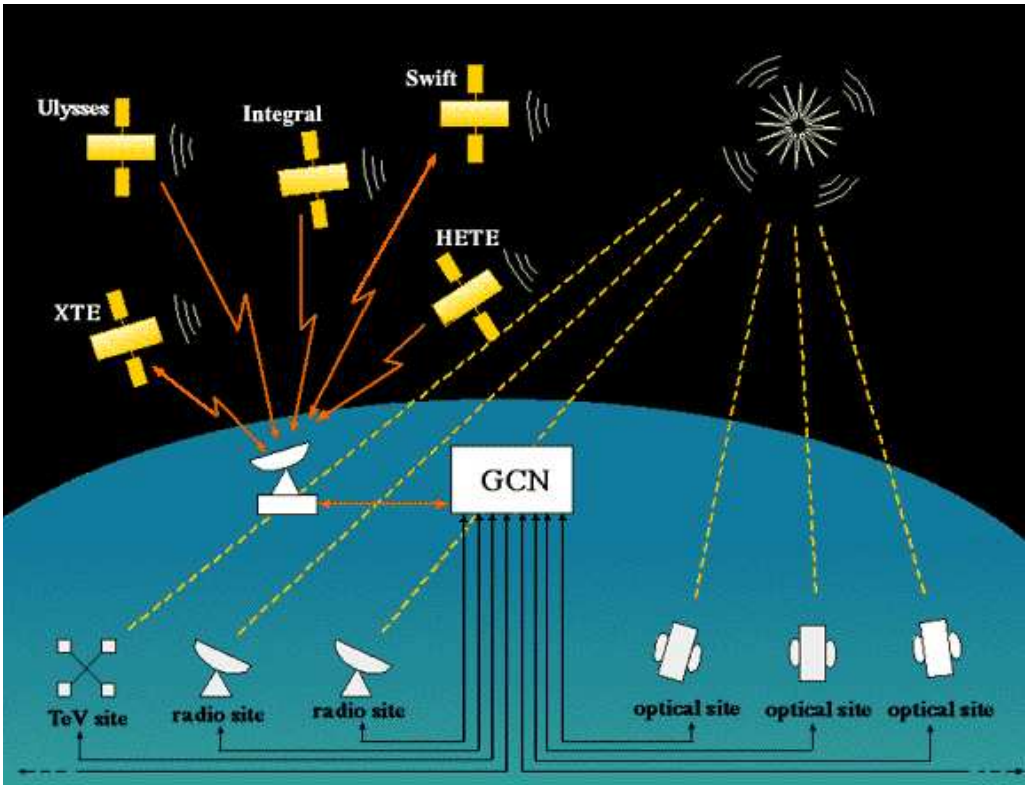

Figure 3.5.: Overview of the GCN. The Ulysses probe shown in the figure is no longer active. On the other hand, Fermi-GLAST is now operational and connected to the GCN. (source: `http://gcn.gsfc.nasa.gov/GCN.gif`)

a declination that never rises above the horizon, are suppressed.

Sources that may be observed at a later time are indicated and saved in a database. As OPTIMA-Burst can move the telescope automatically, potentially disturbing an already-running observation, filtering of unsuitable sources is critical.

For sources that are suitable for immediate observation, the OPTIMA-Burst software checks whether the source is a new trigger, or whether the notice contains position updates to a previous trigger. In the case of a new trigger, it attempts to automatically slew the telescope to the correct pointing, and bring the telescope into the correct configuration for OPTIMA observations (focus, M3 position). The software saves the trigger details into a database for further reference, sounds a loud alarm in order to alert the observer, and displays a large and clear status message. The OPTIMA-Burst session shown in Fig. 3.4 shows a typical scenario. If the notice is merely a position update (possibly with reduced position errors) the software shows a more subdued notice box and sounds a softer short alarm sound. The new coordinates are saved in the database, but the telescope is not moved automatically – if the observer has already identified the OT and started a observation, an automatic movement of the telescope could move the source from the aperture. Thus, the observer must decide to move the telescope to the coordinates saved in the database, if appropriate.

3.2.2. Transient Detection

As previously stated, minimizing the reaction time between reception of a GRB trigger and correct positioning of the OT on the OPTIMA aperture is critical in OPTIMA-Burst. The reaction time can be reduced with reliable automation of as many of the tasks necessary to commence observation as possible. Ideally, the complete observation would be automated.

However, besides speed, reliability is critically important. In contrast to an imaging instrument, where the identification needs only be "good enough" to guarantee the real optical counterpart is contained in the FoV, an aperture instrument like OPTIMA needs precise identification of a point-source before it can begin to take data. Mis-identification thus is very costly, as the most interesting part of the early light-curve plays out unobserved, while OPTIMA would observe the light-curve of a random field star. When – or indeed if – the error is noticed some time later, e.g. due to a GCN position update, it is too late – the data is already lost. Therefore, while speed is of the essence, the trade-off between speed and reliability needs to be biased towards reliability in OPTIMA-Burst.

Incoming GRB triggers are categorized as described in the previous section, and saved into an internal database. Uncatalogued and variable or transient sources can be readily identified and thus marked by software with data-base comparisons. Avoiding spurious detections is much harder, though. In order to highlight also very faint candidates, the detection threshold has to be set near the background noise-limit, spurious detections need to be traded off against detection sensitivity.

The situation is further complicated by idiosyncrasies of the USNO catalogue used in OPTIMA-Burst. Near the limiting magnitude, the catalogue is not complete (with a lower completeness in more crowded fields) and it frequently misidentifies several close sources as a single, brighter source, even though the sources are clearly separated in the underlying DSS plates. Furthermore, the catalogue has a brighter limiting magnitude and spurious sources in the vicinity of very bright stars. All of this can be readily demonstrated in *XEphem*, as *XEphem* can automatically overplot the USNO catalogue on top of the DSS-plates underlying the catalogue.

While these problems are extremely hard to identify in an algorithmic fashion, they are usually immediately obvious to a human observer. In OPTIMA-Burst, therefore a semi-automatic approach was preferred over the theoretical ideal of a fully automatic approach. The software matches detected sources, catalogue and GCN error-circles, and overplots these onto the incoming CCD frames in a visually descriptive fashion (Fig. 3.4). Most often, the observer can identify the GRB counterpart at a glance, and use the automatic pointing routine to start the observation with minimal reaction time, and maximum reliability.

4. OPTIMA Data Analysis

OPTIMA is a single-photon sensitive aperture photometer that records the arrival time of each photon individually. As the underlying operating principle of integrating and photon-counting detectors and of imaging and fixed aperture detectors are quite similar (photons are collected in a focal plane, photons are converted to charge, charge is amplified, and the amplified signal is digitized), also the data analysis steps for a system like OPTIMA shares the same concepts as for e.g. CCDs. The data analysis of imaging and integrating detectors is comparably wide-spread, and will therefore be summarized briefly to show the analogous analysis of OPTIMA data:

Bias subtraction The read-out electronics of a detector typically adds a bias onto the measured signal charge. This bias can be constant, but can also have a non-negligible time dependence. A constant bias can be estimated by taking a 0 s exposure, time dependent bias (often called *common mode*) can be estimated by analysing non-illuminated parts of pixels at the edge of the detector.

Dark subtraction During integration, sensors accumulate leakage current, which shows as a signal even in the absence of light. The dark current can be estimated by taking a non-illuminated exposure of the same length as the science exposure, or by modelling the dark current in dependence of exposure length and detector temperature. Dark current and bias subtraction can be combined into one step, as the dark-frame also contains bias.

Flat fielding The illumination of the focal plane is not necessarily homogeneous, but can be position dependent. Also, the sensitivity of the detector can be inhomogeneous. By measuring the signal of a known-homogeneous light source (e.g. the twilight sky, or an artificial illuminated screen), this inhomogeneity can be measured and corrected.

Flux estimation The target flux can be estimated by selecting an appropriate aperture around the target, which can be optimised for the conditions during the integration time. As a more sophisticated method of flux estimation, a model can be fitted to the measured image of the PSF. The flux can then be determined by an integral over the model PSF.

Background estimation Using an imaging detector, the background can be estimated by choosing an appropriate aperture, i.e. a region of the detector not contaminated by either the target or a random field source.

Additionally, the choice of a suitable integration time is implicitly done before the actual measurement and cannot be changed later.

While the OPTIMA data analysis is similar, it does differ from the aforementioned procedure in the order in which the steps are applied, and in some details of how the steps are performed.

Binning For most methods of event data analysis, the event data is binned up to event rates as a first step by defining time segments, counting the number of events falling into each time segment, and normalizing with the length of the segment. This is analogous to the implicit selection of integration time in the integrating detector case.

Dark rate subtraction Similar to integrating detectors, photon counters suffer from dark current. This results in a low but non-zero trigger rate of the detector even in the absence of illumination. Like in the integrating detector case, it is estimated by closing a shutter and measuring the dark count-rate. This rate is subtracted from the measured count-rate to determine the measured photon count-rate.

Flat fielding The apertures of of an aperture photometer can be inhomogeneously illuminated and can differ in sensitivity in a similar way as the individual pixels of an imaging detector, necessitating a similar flat-field correction. However, obtaining the flat-field correction factors is simpler for aperture photometers, as the sky background in the vicinity of the target can be used. For this reason, OPTIMA observations usually begin and end with some data taken on a nearby clear patch of sky.

Background selection In an aperture photometer, at least one aperture must be is dedicated to background estimation. If the position of the background fibre cannot be modified, usually there are multiple background fibres to avoid contamination by field-sources. In a crowded field, selection of uncontaminated background channels can be critical.

Background estimation The non-contaminated background channels are used to estimate and subtract the background light from the source count-rate.

As in the case of the integrating imaging detector, there is one implicit step performed before data acquisition: aperture selection. In contrast to an imaging detector, the apertures of target and background regions cannot be adjusted to changing observing conditions after the fact. As one cannot *see* what is happening on the sky during data analysis, data interpretation can be difficult in unfavourable observing conditions like bad seeing, thin clouds or during wind-shake.

The benefit of choosing the time-resolution of the measurement during data-analysis can outweigh these difficulties for many sources, though. Instead of assuming how a target *will* behave during an observation and setting the integration time accordingly, one can observe how the target *actually* behaved during the observation, and choose an optimal trade-off of time-resolution versus signal-to-noise ratio. In some cases, it can also be beneficial to not choose a constant time-resolution, but choose a different binning during different phases of the observation, e.g. very long bins during the eclipse of a cataclysmic variable, and very short bins during a flare.

4.1. Adaptive Data Binning

In order to fully utilize the variable time-resolution of OPTIMA, it is advantageous to not only choose the time resolution for specific observations or parts of observations, but to choose the optimum binning for each instant of an observation. For this to be feasible, the process of choosing a near-optimal time resolution needs to be automated. In the scope of

this work, a simple algorithm was developed that implements automated adaptive event data binning.

The general idea of the algorithm is to keep the significance of the detection contained in each bin roughly constant, i.e. the fraction of source counts with respect to the error of total measured counts shall remain constant within each time bin. Assuming Poisson statistics, for a measurement of C counts, which contain B background counts and S source counts, the threshold T for $n\,\sigma$ significance is[1]

$$T = n\,\frac{S}{\sigma} = n\,\frac{C-B}{\sqrt{C}} \tag{4.1.1}$$

The most direct way to implement an algorithm to ensure this behaviour is to start with a light-curve with constant binning, and iteratively evaluate the light-curve, increasing bin-size where there are insufficient counts in one bin to satisfy the significance criterion, or reduce bin-size where the significance of detection is larger than requested. While conceptually very simple (this is what a human would do by hand), this iterative process is computationally expensive.

Another simple implementation can be achieved by working through the list of events one-by-one, keeping tally of the significance of the detection after each event, and creating a bin-boundary as soon as the significance threshold is reached. This method has the advantage of scaling only linearly with the number of events, and not with the number of events times the number of iterations. However, in order to implement this more efficient algorithm, the canonical OPTIMA data analysis procedure as described in the previous section, binning – dark subtraction – flat fielding – background subtraction, must be modified: all steps must be implemented in such a way that they can work on event data instead of binned data, as the significance of the bin needs to be estimated before the binning is completed. For the purpose of adaptive binning, the data-analysis steps are thus modified in the following fashion:

Flat-fielding Instead of normalizing the count-rate in each bin using a normalization factor for each fibre, the normalization factor is applied on a per-event base. In effect, each photon is weighted with a factor depending on which fibre it was detected with.

Background subtraction Background subtraction is performed by incrementing two "photon counter" variables, C for the target fibre (incremented when a photon is detected in the target fibre), and B for the background (incremented when a photon is detected in a background fibre). The increment used for the background counter is based on the flat-field normalization factors, divided by the number of background channels selected. Therefore, the counts contained in both counters can be directly compared, and the source count is simply the difference of the two counters.

Binning After each event, the significance threshold T of the detection is tested by comparing the difference of the two counters to the square root of the target counter (4.1.1). If T is larger than a pre-set value, the end of a bin is triggered. If the trigger threshold is not met, the next event is processed. In this step, also alternative trigger conditions like minimum or maximum bin lengths can be defined. The length of the bin is computed as the difference between the last time-code of the preceding bin and the last time-codes used in the current bin.

[1] This assumes the background estimate is free of error. As multiple channels are used for background estimation, and the threshold is used only to achieve roughly constant significance in each bin, this simplification is valid.

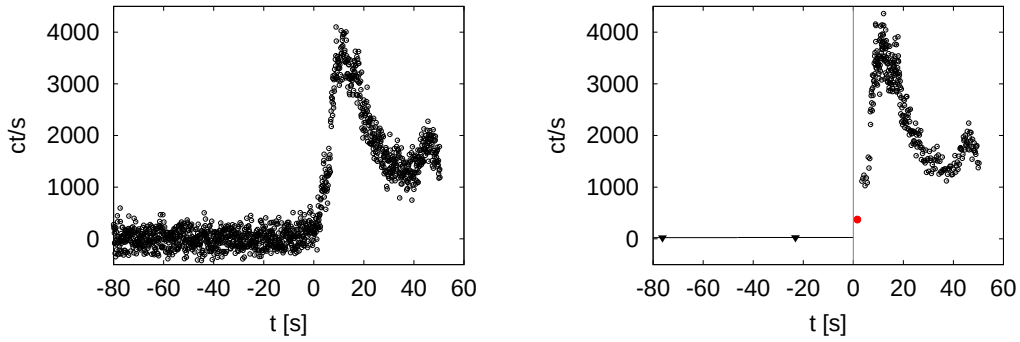

Figure 4.1.: Adaptive binning technique compared to constant binning. Panel (a) shows the onset of a flare of J1955 (Chapter 6) at 0.1 s binning, a time-resolution good enough to resolve structure in the high SNR parts near the maximum of the flare. However, it is obvious that in the quiescent phase before the onset of the flare at $t < 0$ s, as well as after the first peak of the flare, the SNR is insufficient to support this time-resolution. Also, it is clear that by not deriving proper upper limits but simply subtracting the background from the measured photons, non-physical results (negative count-rates) are produced. Panel (b) shows the same flare with adaptive binning. While the first peak has similar time-resolution as manually selected in the constant binning case, the time-resolution in the second peak is reduced to ~ 0.3 s, leading to a much better SNR. In the quiescent phase at $t < 0$ s, the maximum bin size 60 s was chosen, and upper limits were produced (Chapter 4.2). However, without setting a manual trigger for the start of a bin (vertical line), the onset of the flare (red data-point) would have been lost.

Dark subtraction After the end of a bin is triggered, the number of dark counts contained in the bin is estimated from the bin-time and the average dark count-rate for both C and B. For B, this is adjusted by the fibre normalization factors and number of channels. After this step, the final source count-rate for this bin is calculated and saved.

The method outlined here has great advantages at extracting most features from a light-curve, as shown in Fig. 4.1 However, the method has several disadvantages as well, that need to be traded off against its advantages.

Firstly, a source count-rate of zero, i.e. equal background and target fibre count-rates result in infinitely long time-bins, as the significance threshold is never exceeded. This effect can become more dramatic if during a period of very low or zero source count-rate if the fibre normalization factors are slightly mis-adjusted, resulting in systematically higher background count-rates than target-fibre count-rates.

By introducing a maximum bin-length after which the end of a bin is triggered regardless of the significance reached, a more sensible behaviour for zero count-rate sources can be introduced. However, a slight negative bias by faulty normalization factors still has a more severe impact than using standard binning. Using standard binning, it is only

a slight nuisance that shifts the baseline, whereas using adaptive binning, it changes the time-resolution. Therefore, more care needs to be taken to properly adjust the fibre normalization factors.

Secondly, the adaptive binning technique by definition results in non-equal bin spacing. If the light-curve is to be analyzed in the frequency domain e.g. by creating a PSD[2], methods based on Fourier transformation cannot be used at all, and methods based on correlation become very cumbersome. However, alternative methods for frequency-domain analysis of non-equally spaced sampled data exist, e.g. the Lomb-Scargle Periodogram [Lomb, 1976] [Scargle, 1982], a member of the LSSA[3] family of analysis methods. In this, the data is approximated by a weighted sum of sinusoidal curves of increasing frequency, which is found using least-squares fitting.

Lastly, the adaptive binning method proposed here can miss the sudden onset of a bright flare in some cases: If a long period of very low or zero source count-rate precedes a sharp rise in source count-rate, both the background as well as the target photon counters B and C contain a large number of photons. As the significance of detection is computed using the full number of photons in the current bin, a high photon rate for a short period of time is seen as less significant at the end of a long low count-rate bin, than when it is observed in isolation. To work around this property of the proposed algorithm, a burst-detection algorithm can be employed e.g. by comparing a running average with the content of the current bin. However, as this effect does not occur very frequently, manual trigger points can simply be set shortly before the onset of flares.

4.2. Upper Limits

In the analysis as described above, one critical step always is background subtraction. In the scope of this work, a superior background subtraction method based on Bayesian statistics was implemented. This allows deduction of meaningful upper limits and facilitates logarithmic scaling of light-curves as in the frequently used astronomical magnitude scale.

In OPTIMA, as indeed in most counting experiments, this is usually done in a straightforward way: For measured counts C and an estimated background B, the source count is derived by subtracting the background estimate from the measured count: $S = C - B$. For large numbers of counts, the Poisson statistics underlying the photon arrival times can be approximated by a Gaussian distribution, and the error of C can be simply estimated by $\sigma_C = \sqrt{C}$. If the background estimate contains an error σ_B, the error of the resulting source count can be estimated as $\sigma_S = \sqrt{\sigma_C^2 + \sigma_B^2}$.

While these source count and error estimates are valid for detections with large number of counts in C, B, *and* S, i.e. observing conditions which are not photon starved and in which the source can be well distinguished from the background, the case in which a source is undetected in the measured background cannot be treated properly using this method. Fig. 4.1(a) (at $t < 0$ s) shows an example which demonstrates what happens: within the variance of the source-count estimate σ_S, the source-count estimate fluctuates around zero. While it is clear to the observer that this simply means the source is not

[2]Power Spectral Density
[3]Least-squares spectral analysis

detected, the actual result is non-physical. The source cannot emit "minus S counts per second", yet half the values are negative.

Furthermore, it is difficult to extract meaningful upper limits out of this. Often a simple upper limit U is estimated using the fluctuation of the measurement σ_S: It is argued that since the fluctuation of the number of source counts S is σ_S, and $S = 0$ counts were observed, a source with $S \geq 2\,\sigma_S$ counts *would have* been observable with 95.4% probability, hence the 95% upper limit is $U = 2\,\sigma_S$. This reasoning confuses an argument for the measurement of the intensity of a source with a criterion for the existence of a source. While it does give a detection threshold, it is incorrect for the intensity of the source, as it does not consider the fluctuations of the source. Also, it does not handle negative computed values of $S = C - B$ gracefully: the upper limit $U = S + n \cdot \sigma$ can still be negative.

A correct and elegant way of computing upper limits is offered by the Bayesian formalism. A very good and complete introduction into the Bayesian formalism as applied to astrophysics can be found in [Loredo, 1990]. Here, the briefer formalism as proposed by [Helene, 1983, Helene, 1984, Kraft et al., 1991] will be followed.

An upper limit of U with a confidence α simply means that the probability of having a value larger than U is $1 - \alpha$. Therefore, the upper limit can be determined using an appropriate PDF[4], by solving for U:

$$\int_0^U P_{C,B}\,(S)\;\mathrm{d}S = 1 - \alpha \tag{4.2.1}$$

The caveat is, however, the selection of the appropriate PDF. $P_{C,B}\,(S)$ is the probability P of a source to have a brightness S in the presence of a background-contaminated measured value C and a background estimate B. This PDF is not immediately obvious from the statistical values of the measured C and estimated B, as the underlying Poisson distribution gives us only the probability P to measure C counts in the presence of S counts from the source, and B counts from the background:

$$P_{S,B}\,(C) = \frac{e^{-(S+B)}\,(S+B)^C}{C!} \tag{4.2.2}$$

However, both PDFs are linked by Bayes' theorem[5] [Loredo, 1990]:

$$P_{C,B}\,(S) \propto p(S) \cdot P_{S,B}\,(C) \tag{4.2.3}$$

Here, $p(S)$ is called the *prior* and contains additional information about the behaviour of the source, which is known prior to the measurement. In the case presented here, a very conservative prior is used:

$$p(S) = \begin{cases} 0 & S < 0 \\ \text{const} > 0 & S \geq 0 \end{cases} \tag{4.2.4}$$

This ensures positive values for S, without imposing any other properties. In particular, the prior (4.2.4) not even attempts to limit arbitrarily high fluxes, let alone any specific

[4] Probability Density Function

[5] The proportionality instead of equality sign in (4.2.2) stems from the fact that in contrast to the usual expression of Bayes' theorem, the normalization is not implicitly performed by a factor of $\frac{1}{p(C)}$, but will be numerically be computed at the end.

source behaviour. It can be demonstrated that the precise choice of prior has only negligible impact on the final results [Kraft et al., 1991].

Using $P_{S,B}(C)$ and the prior in (4.2.3), $P_{C,B}(S)$ can be expressed as:

$$P_{C,B}(S) = a_1 \cdot \frac{e^{-(S+B)}(S+B)^C}{C!} \tag{4.2.5}$$

With a_1 a normalization constant chosen such that $\int_0^\infty P_{C,B}(S)\,\mathrm{d}S = 1$. In the case presented in (4.2.5), this means:

$$a_1 = \sum_{n=0}^{C} \left(\frac{e^{-B} B^n}{n!} \right)^{-1} \tag{4.2.6}$$

It is worthwhile to note that while in the case presented here, $P_{C,B}(S)$ and $P_{S,B}(C)$ look almost identical, their interpretation in the Bayesian formalism is very different. $P_{S,B}(C)$ is the usual Poisson distribution, which gives the probability of measuring C counts from a source S and background B. $P_{C,B}(S)$ on the other hand reverses the roles of C and S: now C is only a parameter similar to B, which gives the probability in dependence of S. This can be interpreted as probability with which the observed C and estimated B *could have come* from a source S. $P_{C,B}(S)$ therefore does not describe a population of possible measurements (as $P_{S,B}(C)$ does in the "frequentist approach"), but describes a population of possible sources, which could explain the observation. This is the crucial difference between the Bayesian and the frequentist formalism in statistics.

While this seems unusual at first, the Bayesian interpretation is actually very similar to what the astrophysicist intuitively interprets. In astronomy, measurements cannot be repeated arbitrarily, therefore a population of hypothetical measurements is not a good description of the analysis process. On the other hand, the comparison of many different models that could possibly explain an existing observation is at the core of astrophysics.

On a more practical note, in OPTIMA, binning is usually chosen such that $C \gg 1$. Therefore, (4.2.5) can be simplified by approximating the Poisson distribution with a Gaussian distribution:

$$P_{C,B}(S) = a_2 \cdot \frac{e^{-(S-\overline{S})^2}/2C}{\sqrt{2\pi C}} \tag{4.2.7}$$

with $\overline{S} = C - B$. In other words, $\overline{S}$ is the naïve estimate for S mentioned at the beginning of this section, which makes sense in the case $C \gg 1$. Again, a_2 is chosen such that $\int_0^\infty P_{C,B}(S)\,\mathrm{d}S = 1$.

Strictly speaking, (4.2.5) and (4.2.7) are only valid as long as the background B is precisely known or its standard deviation is negligible. In OPTIMA, numerous background fibres are used, making the error of the background estimate smaller than the error of the measured counts. However, the error of B is not always small enough, e.g. if not all background fibres can be used for background estimation, due to field-source contamination. If the error of the background estimate is not negligible but $B \gg 1$ in addition to $C \gg 1$ (which in OPTIMA usually can be ensured by proper binning), the PDF of B can be approximated by a Gaussian distribution with a mean of $\overline{B}$ and a standard deviation

σ_B, and (4.2.7) can be generalized to:

$$P_{C,B}(S) = a_3 \cdot \frac{e^{-(S-\widetilde{S})^2}/2\sigma^2}{\sqrt{2\pi}\sigma} \tag{4.2.8}$$

with a_3 the normalization, $\widetilde{S} = C - \overline{B}$, and $\sigma^2 = \sigma_B^2 + C$. In both (4.2.7) and (4.2.8), the normalization constant a is easiest determined numerically.

All upper limits plotted in this work are calculated by numerically solving (4.2.1) with a *Matlab/Octave* code using a confidence value of $\alpha = 95\%$, and with (4.2.8) used for $P_{C,B}(S)$.

4.3. Pile-up Correction

Using the classic OPTIMA DAQ system, only one event per DAQ read-out cycle time τ can be recorded (see Chapter 2.5.1). For every read-out-cycle during which at least one photon arrives, OPTIMA counts a single event. Obviously, the missed events cannot be individually recovered. After data binning, their loss can however be treated statistically. In the scope of this work, an analytical formula for correcting the pile-up both in count-rate as well in the error of the count-rate has been derived.

Usually in astronomy, Poisson statistics can be assumed for the photon arrival events underlying an astronomical observation. The properties of the Poisson distribution are very benign, easing data analysis to a large degree. The fact that not all photons arriving at the detector are treated equally, but that the detection of one photon becomes dependent of the detection of other photons, means that one basic prerequisite needed for the assumption of Poisson statistics ceases to apply: events can only be considered Poisson-distributed if they are both rare and *independent*.

Pile-up becomes non-negligible already at moderate count-rates, but is only a real problem at very high count-rates. Figure 4.4 shows a synthetic light-curve demonstrating severe pile-up. As the pile-up effect stems from a change in the statistics underlying the events, the correction cannot be performed by a simple correction factor: Scaling does not change the event distribution.

In order to understand the effect of the changed photon distribution on OPTIMA data, the expectation value and variance of the distribution need to be evaluated. This results in the possibility of correcting for the lost events, and understanding the impact on the uncertainty of the count-rate.

To facilitate the usage of this section as reference for OPTIMA data reduction, the pile-up correction formulae shall be briefly summarized at this point, before progressing to their detailed derivation.

$$R(r) = -\frac{1}{\tau}\ln(1-\tau r)$$

Corrected rate R for measured rate r
See (4.3.8)

$$\sigma_R = \sqrt{\frac{r}{\Delta t}\cdot\frac{1}{(1-\tau r)}}$$

Uncertainty σ_R of corrected rate R
See (4.3.10)

Here, τ is the DAQ read-out cycle time, Δt is the binning time used during analysis.

4.3.1. Poisson Distribution

To better understand the differences between the pile-up distribution and the properties of a Poisson distribution, a brief recapitulation of the Poisson distribution is helpful.

The Poisson distribution is defined by random events arriving in such a manner, that the probability p_k to observe k events in one trial is given by:

$$p_k = \frac{\lambda^k}{k!} e^{-\lambda} \tag{4.3.1}$$

With λ the mean number of events observed in previous trials. In the context of light-curves, k is the number of photons observed in an interval τ, and λ can be expressed in terms of the mean count-rate R as $\lambda = \tau \cdot R$. Figure 4.2(a) shows an example for typical OPTIMA operational parameters.

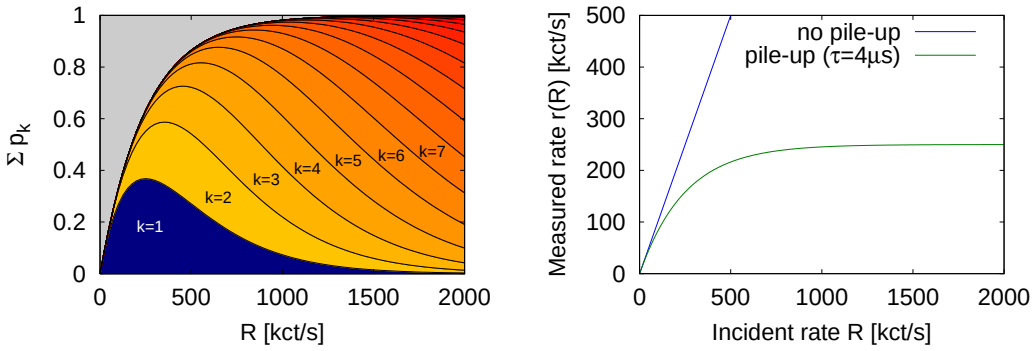

(a) (b)

Figure 4.2.: The effects of the classic OPTIMA DAQ on count-rate limitations. Shown in (a) are the probabilities p_k of k photons arriving in an interval $\tau = 4$ µs stacked on top of each other. The probabilities $p_{k>1}$ are shown in shades of orange. The more area is shaded orange, the larger the probability for pile-up becomes, the redder an area is shaded, the more photons are lost in one pile-up event. It becomes clear that for large count-rates pile-up is dominating. Shown in (b) is the effect of pile-up. While an ideal DAQ continues to count incoming events linearly (blue curve), pile-up causes the detected rate to approach $1/\tau$ asymptotically.

The *expectation value* E(X), i.e. the mean of all events x for many trials, is defined by

$$\mathrm{E(X)} = \sum_{i=0}^{\infty} x_i \cdot p(x_i)$$

In the case of photon arrival rates, it can be interpreted as the mean number of photons C_τ in an interval τ. For Poisson-distributed events, this becomes[6]:

$$\begin{aligned} \mathrm{E}(\mathrm{C}_\tau) &= \sum_{k=0}^{\infty} k \cdot p_k \\ &= \ldots = \tau \cdot R \end{aligned}$$

[6]Some intermediate steps of some derivations will be omitted, as they only consist of standard but long-winded simplifications and do not help better understand the Poisson distribution

As the number of photons in one time-interval is independent from the number of photons in a different time interval, $\mathrm{E}(\mathrm{C}_\tau)$ is additive and multiplicative. Therefore, we can easily scale $\mathrm{E}(\mathrm{C}_\tau)$ to another time interval Δt:

$$\mathrm{E}(\mathrm{C}_{\Delta \mathrm{t}}) = \tau \cdot R \cdot \frac{\Delta t}{\tau} = \Delta t \cdot R \tag{4.3.2}$$

The *variance*, i.e. the mean quadratic distance of all events x from the expectation value $\mathrm{E(X)}$ is defined by:

$$\mathrm{var}(X) = \sum_{i=0}^{\infty} \left(x_i - \mathrm{E(X)}\right)^2 \cdot p(x_i)$$

In the case of Poisson-distributed photon arrival events, this becomes:

$$\begin{aligned} \mathrm{var}(C_\tau) &= \sum_{k=0}^{\infty} \left(k - \mathrm{E}(\mathrm{C}_\tau)\right)^2 \cdot p_k \\ &= \ldots = \tau \cdot R \end{aligned}$$

The statistical parameters $\mathrm{E}(C_\tau)$ and $\mathrm{var}(C_\tau)$ can be interpreted physically. As the expectation value corresponds to the mean number of photons expected in a time interval τ, it is associated with the event rate:

$$R = \frac{1}{\tau} \cdot \mathrm{E}(\mathrm{C}_\tau) \tag{4.3.3}$$

Similarly, the variance is connected to the standard deviation σ of the photon rate:

$$\begin{aligned} \sigma_{C_\tau}^2 &= \mathrm{var}(C_\tau) \\ \sigma_{C_\tau} &= \sqrt{\tau \cdot R} \\ \sigma_{C_{\Delta t}} &= \sqrt{\Delta t \cdot R} \end{aligned}$$

Where the last line uses the same scaling applied in (4.3.2). This standard deviation is expressed in units of counts in an individual bin. Usually, the standard deviation in units of count-rate, i.e. counts per time, is more relevant. This can be achieved by scaling the standard deviation $\sigma_{\Delta t}$ with the bin-time Δt:

$$\sigma_R = \frac{\sigma_{C_{\Delta t}}}{\Delta t} = \sqrt{\frac{R}{\Delta t}} \tag{4.3.4}$$

4.3.2. Pile-up Distribution

In the same way that the physical properties R and σ_R have now been derived from the probability distribution defined by p_k, similar properties from the probability distribution affected by pile-up can be derived.

To understand the probability distribution of the pile-up affected observed photon rate, it is helpful to describe the scenario first: If one or more photons hit the sensor in a time interval τ, it detects a single event. If no photons hit the sensor, it detects zero events. It cannot detect multiple events, no matter how many photons hit the detector. Therefore, just two relevant cases exist: No detected events, with the identical probability as in the not pile-up affected Poisson distributed case, and one event, with the reciprocal probability of no events.

Expressing this in equations, the probability distribution of the pile-up affected observed photon rate can be described as:

$$p_k^* = \begin{cases} p_0^* = p_0 = e^{-\tau R} \\ p_1^* = 1 - p_0 = 1 - e^{-\tau R} \\ p_{>1}^* = 0 \end{cases} \tag{4.3.5}$$

As p_1^* is the only non-nil probability for an event $k > 0$, the expectation value is easy to calculate:

$$\mathrm{E}(\mathrm{c}_\tau) = \sum_{k=0}^{\infty} k \cdot p_k^* = p_1^* = 1 - e^{-\tau R} \tag{4.3.6}$$

Using the identities $p_1^* = \mathrm{E}(\mathrm{c}_\tau)$ and $p_0^* = (1 - \mathrm{E}(\mathrm{c}_\tau))$, the variance of the pile-up distribution is:

$$\begin{aligned} \mathrm{var}(c_\tau) &= \sum_{k=0}^{\infty} \left(k - \mathrm{E}(\mathrm{c}_\tau)\right)^2 \cdot p_k^* \\ &= \mathrm{E}(\mathrm{c}_\tau)^2 p_0^* + \left(1 - \mathrm{E}(\mathrm{c}_\tau)\right)^2 p_1^* \\ &= \mathrm{E}(\mathrm{c}_\tau)\left(1 - \mathrm{E}(\mathrm{c}_\tau)\right) \\ &= \left(1 - e^{-\tau R}\right) e^{-\tau R} \end{aligned}$$

With the statistical properties $\mathrm{E}(\mathrm{c}_\tau)$ and $\mathrm{var}(c_\tau)$ determined, the physical properties r and σ_r can be derived similar to the simple case of Poisson distribution. Furthermore, the function $R(r)$, which allows to estimate the incident photon rate prior to pile-up R from the pile-up affected measured rates r, can be deduced by inverting $r(R)$.

The measured event rate r is for a given incident rate R:

$$r(R) = \frac{1}{\tau}\,\mathrm{E}(\mathrm{c}_\tau) = \frac{1}{\tau}\left(1 - e^{-\tau R}\right) \tag{4.3.7}$$

Inverting this results in the formula for pile-up correction:

$$R(r) = -\frac{1}{\tau}\ln\left(1 - \tau r\right) \tag{4.3.8}$$

To determine the measurement uncertainty of the corrected incident count-rate, the standard deviation σ_R has to be derived from the properties of the observed pile-up affected count-rate $r(R)$. The standard deviation for the number of counts in an observed bin τ is

$$\sigma_{c_\tau} = \sqrt{\mathrm{var}(c_\tau)} = \sqrt{e^{-\tau R}\left(1 - e^{-\tau R}\right)}$$

This gives σ_{c_τ} expressed in dependence of R; inserting (4.3.8) gives σ_{c_τ} in terms of r:

$$\sigma_{c_\tau} = \sqrt{\tau r\left(1 - \tau r\right)}$$

By applying the same scalings as in (4.3.2) and (4.3.1), the standard deviation can be given in units of count-rate instead of counts:

$$\sigma_r = \sqrt{\frac{r}{\Delta t}\left(1 - \tau r\right)} \tag{4.3.9}$$

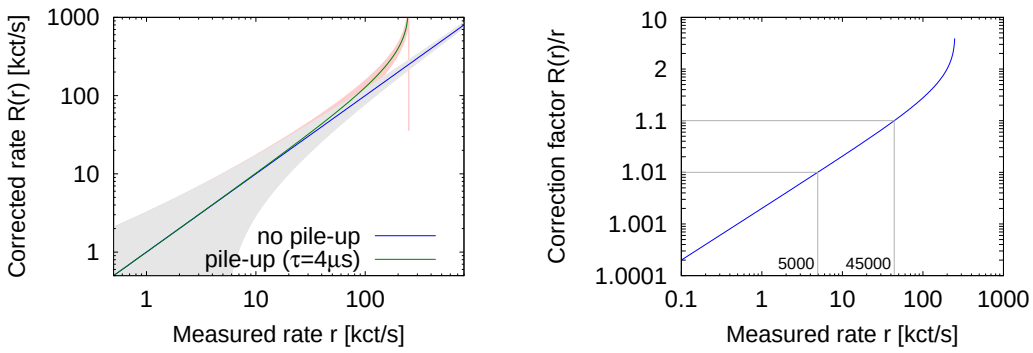

(a) (b)

Figure 4.3.: Correction to compensate pile-up effects. Plotted in (a) is the corrected count-rate against measured count-rate. An ideal pile-up free system is shown as comparison. The shaded areas correspond to the standard deviation at 20 ms binning. As this is a log-log plot, the width of the shaded band directly represents the SNR. While the SNR of the curve with no pile-up continues to improve at high count-rates, the pile-up correction causes the SNR to sharply degrade at very high count-rates. Plot (b) visualizes the magnitude of the correction. At around 5000 ct/s, the correction reaches the 1 % level, at 45000 ct/s, it reaches the 10 % level,

From σ_r, the uncertainty of R can be calculated by error propagation:

$$\sigma_R = \frac{dR}{dr} \cdot \sigma_r$$

With the derivative $dR/dr = 1/(1 - \tau r)$, this becomes:

$$\sigma_R = \sqrt{\frac{r}{\Delta t} \cdot \frac{1}{(1 - \tau r)}} \tag{4.3.10}$$

4.3.3. Discussion

The correction (4.3.8) becomes $R(r) \approx r$ for small r, since $\ln(1 + x) \approx x$. It is only defined for values of $r \in [0, 1/\tau]$, because its inverse (4.3.8) asymptotically approaches $r(R) \approx 1/\tau$ for large values of R (see Fig. 4.2). Similar limits also apply for σ_R in (4.3.10). The results of these extreme-value considerations are expected for this correction, adding credibility to the deduction of the correction. The correctness of (4.3.8) is also intuitively understandable from a simple probabilistic approach. For (4.3.10) though, this is not so easy.

Therefore, Fig. 4.4 shows the results of a Monte-Carlo simulation modelling the pile-up behaviour of OPTIMA, and the correct treatment thereof by (4.3.8) - (4.3.10). For a simulated source, a FRED[7]-like outburst was modeled. The source rises with a rise-time of 50 ms from a baseline level of 10^4 ct/s to a peak of 10^6 ct/s, and drops back to the baseline with a time constant of 150 ms. Poisson distributed photons have been generated with a mean following this source behaviour. The photons have been subjected to

[7]Fast Rise, Exponential Decay

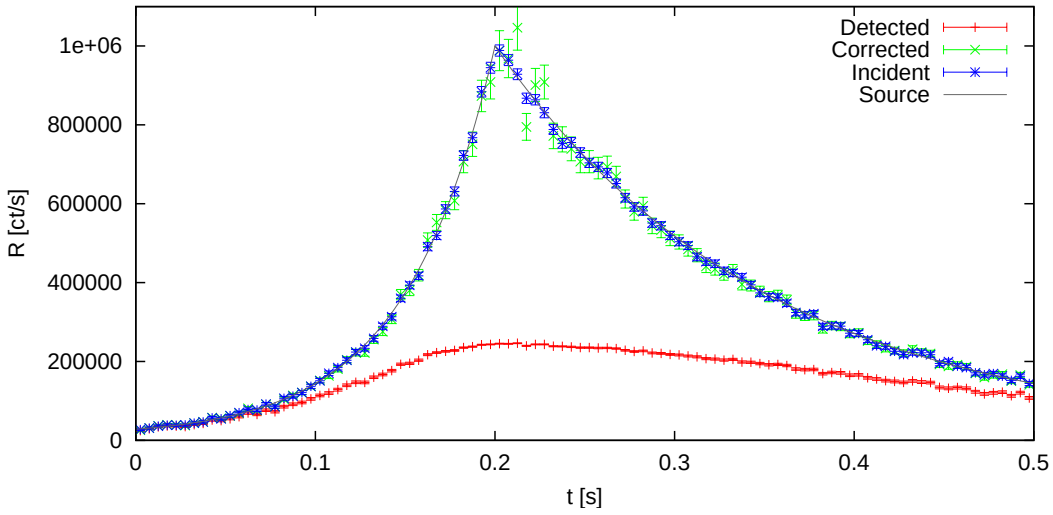

Figure 4.4.: Results of a Monte-Carlo experiment to validate (4.3.8), (4.3.9) and (4.3.10). Shown in black is the behaviour of a simulated source. A pile-up affected measurement has been simulated (red dots) and corrected (green dots). Comparison with a simulated pile-up free measurement (blue dots) shows good agreement. The calculated uncertainty of the measurements are in good agreement with the variance of the simulated data.

pile-up by directly assessing the number of simulated photons arriving in $\tau = 4$ µs DAQ time bins. For bins containing more than one photon, only one photon was propagated. The propagated photons have been binned up with an analysis bin-time $\Delta t = 5$ ms. The error-bars of this simulated measurement were determined using (4.3.9). The simulated measured light-curve was then corrected using (4.3.8), and the uncertainty of the corrected light-curve determined using (4.3.10). The pile-up affected and corrected light-curves have been compared with a light-curve measured by a simulated pile-up free system using the same binning. The error-bars of this light-curve were determined using normal Poisson statistics, i.e. (4.3.4). The results of this experiment, using intentionally extreme observational parameters to achieve strong effects, show that both the amount of correction as well as the deduced uncertainty are in good agreement with simulation results.

The last question left open is when the application of the pile-up correction becomes strictly necessary, and when is it negligible. Figure 4.3(b) shows that the correction reaches non-negligible levels at surprisingly low count-rates. At roughly 5000 ct/s, the correction reaches the 1 % level, at 45000 ct/s it already reaches 10 %. What level of pile-up effect is tolerable before correction is strictly necessary will always depend on the observation. In a non-photometric timing observation, an effect of a few percent might be tolerable, as the arrival time of the photons is not affected and the pulse-shape of light-curves is not yet strongly degraded. In a polarimetric observation on the other hand, the same level of pile-up might already be critical, as the polarization degree depends on differences and ratios between count-rates, and the effect of non-corrected pile up is not easy to asses. As the correction does not adversely influence the observation in any way, the best practice is to apply the correction per default to any observation before further data analysis.

4.4. Nonlinear Detector Response

After detecting a photon, the SPADs used in OPTIMA are insensitive for new photons for a brief period of time. The duration of the detector intrinsic dead-time depends on the detailed setup of each detector and its accompanying quenching circuit. This dead-time effect is aggravated by the data acquisition system used in OPTIMA, which can only record one event per 4 µs time-bin.

On the other hand, deep levels in the band structure of the depletion layer of a SPAD can act as traps for minority charge carriers. These levels trap some of the charge of each avalanche pulse, and release the carriers after a statistical delay. If the delay is longer than the dead-time of the SPAD, i.e. the quenching circuit has re-armed the SPAD, a new avalanche can be triggered by the delayed release of charge from the trap. If the delay is longer than the dead-time of the DAQ system (i.e. longer than the 4 µs sample time of OPTIMA), two photons instead of one are detected. For the Perkin-Elmer SPCM-AQ [Perkin-Elmer, 1997] modules used in OPTIMA, after-pulse probabilities in excess of 1 % and delay spectra extending to longer than 10 µs have been reported [Gösch et al., 2004].

Together, these effects introduce a non-linear dependence of count-rate on the incident illumination. As the effects are strongly dependent on the details of the SPAD geometry, quenching electronics, data acquisition electronics, optical coupling etc., the exact nonlinear behaviour varies from detector to detector.

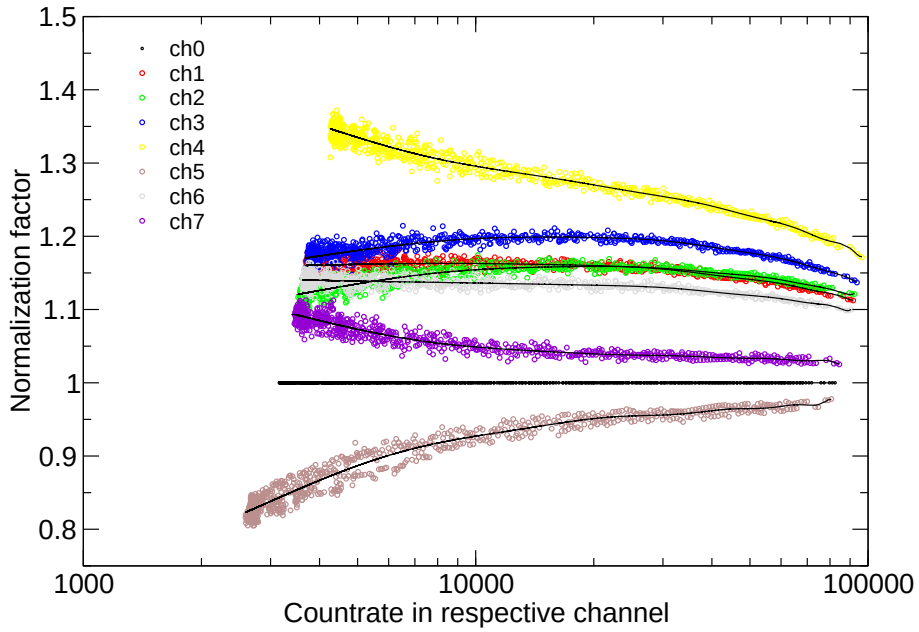

Figure 4.5.: Normalization factors of the seven bundle-fibres, plotted against count-rate. Data from a number of nights and different fields is combined in this plot. The normalization is computed against channel 0. The characteristics of the normalization curves is strongly dependent on the individual detector.

In order to compare the count-rates of different detectors, the count-rates have to be normalized to a common standard. Because of the non-linear behaviour, this needs to be done count-rate dependent, e.g. by measuring the count-rate in all channels for flat-field illuminations of varying brightness. This data is normalized to one channel, which can be

arbitrarily chosen, but is customarily selected as channel 0 for photometry mode, and as average of all four polarimetry channels for polarimetry mode. The normalization factor is plotted against pre-normalization count-rate. This is shown in Fig. 4.5. As an arbitrary DAQ channel was selected for normalization, the curvature of the normalization relation is rising for some channels, and falling for others. For some channels it is even both rising *and* falling, depending on the count-rate regime.

Fig. 4.5 can be used to deduce a conversion to express each channel in units of "channel-0 counts per second". For this purpose, a polynomial fit to the normalization factors can be made. The binned OPTIMA data are then scaled according to the resulting polynomial function.

4.5. Polarimetry Analysis

While no polarimetry data was used in this work, the implementation of the twin-Wollaston polarimeter was part of the development of OPTIMA-Burst. Therefore, a brief introduction into polarimetry analysis will be given here for completeness, but no further discussion of this topic will be given.

4.5.1. Stokes Parameters

The (linear) polarization state of a beam of light can be parametrized in several different ways. The most intuitive parametrization follows a physical description of the polarization state: Intensity I, degree of polarization p and angle of polarization θ. This parametrization is convenient for describing the physical properties of the observed system, and hence is often the intended end-result of a polarimetric analysis.

Mathematically, however, I, p and θ have the downside, that they are not *additive*, making e.g. subtraction of polarized background light tedious. Therefore, a different parametrization is usually used for the intermediate steps between input data and the final solution of the polarimetric quantities, the so called *Stokes parameters* (I[8],Q,U):

$$Q = Ip\cos 2\theta, \quad U = Ip\sin 2\theta \tag{4.5.1}$$

And the inversion thereof:

$$p = \frac{\sqrt{Q^2+U^2}}{I}, \quad \theta = \frac{1}{2}\tan^{-1}\left(\frac{U}{Q}\right) \tag{4.5.2}$$

The Stokes parameters can be understood as a polarization state *vector* $\vec{P} = (I, Q, U)$. With this, operations like background subtraction are trivial:

$$\vec{P}_{\text{src}} = \vec{P}_{\text{measure}} - \vec{P}_{\text{bg}} \tag{4.5.3}$$

[8]The Stokes parameter I is simply the total intensity I of the physical parameters.

4.5.2. Determining the Stokes Parameters

The OPTIMA twin-Wollaston polarimeter determines the intensity of four polarization projections simultaneously:

$$\begin{aligned} I_{0^\circ} &= Ip\,\sin^2(\theta - 90^\circ) \\ I_{45^\circ} &= Ip\,\sin^2(\theta - 135^\circ) \\ I_{90^\circ} &= Ip\,\sin^2(\theta) \\ I_{135^\circ} &= Ip\,\sin^2(\theta - 45^\circ) \end{aligned} \tag{4.5.4}$$

This overdetermined system of equations can be transformed to:

$$\begin{aligned} I &= I_{0^\circ} + I_{90^\circ} \\ Q &= I_{0^\circ} - I_{90^\circ} \\ U &= I_{45^\circ} - I_{135^\circ} \end{aligned} \tag{4.5.5}$$

While this deduction of the Stokes parameters is convenient since it is easily done, it does suffer from a number of downsides. Since the set of equations (4.5.4) is over-determined, the information contained in the additional equation could be used to minimize statistical errors. The determination of errors is non-trivial in this set of equations. Furthermore, the naïve approach assumes ideal polarizers in perfect alignment. Although the real Wollaston prisms are excellent polarizers and the twin-Wollaston setup was custom built to ensure correct and lasting alignment, the assumption of the ideal case is not strictly correct.

4.5.3. The Sparks and Axon Method for N Polarizers

In [Sparks and Axon, 1999], a matrix oriented analysis scheme for the case of N arbitrary polarizers is proposed. This method, although more complicated than the approach in (4.5.4) and (4.5.5), does not suffer from the aforementioned downsides.

Let the four paths through the twin-Wollaston prism be described as four individual polarizers with indices $k = 1 \ldots 4$. These polarizers can be described by the following properties:

$$\begin{aligned} t_k &: \text{transmission coefficient of polarizer } k \\ \epsilon_k &: \text{polarizing efficiency of polarizer } k \\ \phi_k &: \text{position angle of polarizer } k \end{aligned}$$

The transmission coefficient is defined as the fraction of unpolarized light transmitted by a polarizer. A perfect polarizer has $t = 0.5$, whereas a perfectly transparent plate of glass has $t = 1$. The polarization efficiency is defined by

$$\epsilon = \frac{S_\parallel - S_\perp}{S_\parallel + S_\perp}$$

where $S_\parallel$ is the transmittance for light polarized parallel to the polarizer, $S_\perp$ for light polarized perpendicular to the polarizer. With these parameters, the transmitted light in a channel of the OPTIMA twin-Wollaston polarimeter can be described as:

$$I_k = t_k \cdot \left[I + \epsilon_k \left(Q\,\cos 2\phi_k + U\,\sin 2\phi_k\right)\right] \tag{4.5.6}$$

Following [Sparks and Axon, 1999], we will formulate an inversion of equation (4.5.6) for N polarizers, by formulating (4.5.6) in matrix notation for three polarizers, inverting the matrix and then extending the result to the case of N polarizers.

$$(I_1, I_2, I_3) = \begin{pmatrix} t_1 & t_1\epsilon_1 \cos 2\phi_1 & t_1\epsilon_1 \sin 2\phi_1 \\ t_2 & t_2\epsilon_2 \cos 2\phi_2 & t_2\epsilon_2 \sin 2\phi_2 \\ t_3 & t_3\epsilon_3 \cos 2\phi_3 & t_3\epsilon_3 \sin 2\phi_3 \end{pmatrix} \begin{pmatrix} I \\ Q \\ U \end{pmatrix} \tag{4.5.7}$$

Inverting this matrix results in

$$(I, Q, U) = B \begin{pmatrix} I_1/t_1 \\ I_2/t_2 \\ I_3/t_3 \end{pmatrix} \tag{4.5.8}$$

Where

$$B = \begin{pmatrix} \epsilon_2\epsilon_3 \sin(2\phi_3 - 2\phi_2) & \epsilon_1\epsilon_3 \sin(2\phi_1 - 2\phi_3) & \epsilon_1\epsilon_2 \sin(2\phi_2 - 2\phi_1) \\ \epsilon_2 \sin 2\phi_2 - \epsilon_3 \sin 2\phi_3 & \epsilon_3 \sin 2\phi_3 - \epsilon_1 \sin 2\phi_1 & \epsilon_1 \sin 2\phi_1 - \epsilon_2 \sin 2\phi_2 \\ \epsilon_3 \cos 2\phi_3 - \epsilon_2 \cos 2\phi_2 & \epsilon_1 \cos 2\phi_1 - \epsilon_3 \cos 2\phi_3 & \epsilon_2 \cos 2\phi_2 - \epsilon_1 \cos 2\phi_1 \end{pmatrix} / \Omega$$

and

$$\Omega = \epsilon_1\epsilon_2 \sin(2\phi_2 - 2\phi_1) + \epsilon_2\epsilon_3 \sin(2\phi_3 - 2\phi_2) + \epsilon_1\epsilon_3 \sin(2\phi_1 - 2\phi_3)$$

If each of the I_k measurements has an associated variance of σ_k^2, the covariance matrix for the vector (I, Q, U) is given by

$$\sigma_{ij}^2 = \sum_k 1/t_k^2 \; B_{ik} B_{jk} \sigma_k^2 \tag{4.5.9}$$

Therefore, the variances of I, Q, and U are respectively

$$\sigma_I^2 = \left(\frac{B_{11}}{t_1}\right)^2 \sigma_1^2 + \left(\frac{B_{12}}{t_2}\right)^2 \sigma_2^2 + \left(\frac{B_{13}}{t_3}\right)^2 \sigma_3^2$$
$$\sigma_Q^2 = \left(\frac{B_{21}}{t_1}\right)^2 \sigma_1^2 + \left(\frac{B_{22}}{t_2}\right)^2 \sigma_2^2 + \left(\frac{B_{23}}{t_3}\right)^2 \sigma_3^2$$
$$\sigma_U^2 = \left(\frac{B_{31}}{t_1}\right)^2 \sigma_1^2 + \left(\frac{B_{32}}{t_2}\right)^2 \sigma_2^2 + \left(\frac{B_{33}}{t_3}\right)^2 \sigma_3^2$$

This result for $N = 3$ can now be extended for arbitrary N by reducing a set of N polarizers to 3 *effective* polarizers, described by equation (4.5.7) (see [Sparks and Axon, 1999] for derivation).

The intensities I_1'', I_2'', I_3'' measured with the effective polarizers can be described as:

$$I_1'' = \sum_k \frac{t_k I_k}{\sigma_k^2} \qquad I_2'' = \sum_k \frac{\epsilon_k t_k \cos 2\phi_k I_k}{\sigma_k^2} \qquad I_3'' = \sum_k \frac{\epsilon_k t_k \sin 2\phi_k I_k}{\sigma_k^2} \tag{4.5.10}$$

The transmission coefficients can be described as

$$t_1'' = \sum_k \frac{t_k^2}{\sigma_k^2} \qquad t_2'' = \sum_k \frac{\epsilon_k t_k^2 \cos 2\phi_k}{\sigma_k^2} \qquad t_3'' = \sum_k \frac{\epsilon_k t_k^2 \sin 2\phi_k}{\sigma_k^2} \tag{4.5.11}$$

$$\epsilon_1'' = \frac{1}{\sum_k t_k^2/\sigma_k^2}\sqrt{\left(\sum_k \frac{t_k^2}{\sigma_k^2}\,\epsilon_k\,\cos 2\phi_k\right)^2 + \left(\sum_k \frac{t_k^2}{\sigma_k^2}\,\epsilon_k\,\sin 2\phi_k\right)^2}$$
$$\epsilon_2'' = \frac{1}{\sum_k \epsilon_k t_k^2\,\cos 2\phi_k/\sigma_k^2}\sqrt{\left(\sum_k \frac{t_k^2}{\sigma_k^2}\,\epsilon_k^2\,\cos^2 2\phi_k\right)^2 + \left(\sum_k \frac{t_k^2}{\sigma_k^2}\,\epsilon_k^2\,\cos 2\phi_k\,\cos 2\phi_k\right)^2}$$
$$\epsilon_2'' = \frac{1}{\sum_k \epsilon_k t_k^2\,\cos 2\phi_k/\sigma_k^2}\sqrt{\left(\sum_k \frac{t_k^2}{\sigma_k^2}\,\epsilon_k^2\,\cos^2 2\phi_k\right)^2 + \left(\sum_k \frac{t_k^2}{\sigma_k^2}\,\epsilon_k^2\,\cos 2\phi_k\,\cos 2\phi_k\right)^2} \tag{4.5.12}$$

And the effective position angles

$$\phi_1'' = \frac{1}{2}\tan^{-1}\left(\sum_k \frac{t_k^2}{\sigma_k^2}\,\epsilon_k\,\sin 2\phi_k \Big/ \sum_k \frac{t_k^2}{\sigma_k^2}\,\epsilon_k\,\cos 2\phi_k\right)$$
$$\phi_2'' = \frac{1}{2}\tan^{-1}\left(\sum_k \frac{t_k^2}{\sigma_k^2}\,\epsilon_k^2\,\sin 2\phi_k\,\cos 2\phi_k \Big/ \sum_k \frac{t_k^2}{\sigma_k^2}\,\epsilon_k^2\,\cos^2 2\phi_k\right) \tag{4.5.13}$$
$$\phi_3'' = \frac{1}{2}\tan^{-1}\left(\sum_k \frac{t_k^2}{\sigma_k^2}\,\epsilon_k^2\,\sin^2 2\phi_k \Big/ \sum_k \frac{t_k^2}{\sigma_k^2}\,\epsilon_k^2\,\sin 2\phi_k\,\cos 2\phi_k\right)$$

The covariance matrix of equations (4.5.10)- (4.5.13) can be described as inverse of the curvature matrix of the least-square formalism used in [Sparks and Axon, 1999]. The curvature matrix is given by

$$C = \begin{pmatrix} \frac{\partial^2\chi^2}{\partial I^2} & \frac{\partial^2\chi^2}{\partial I\partial Q} & \frac{\partial^2\chi^2}{\partial I\partial U} \\ \frac{\partial^2\chi^2}{\partial Q\partial I} & \frac{\partial^2\chi^2}{\partial Q^2} & \frac{\partial^2\chi^2}{\partial Q\partial U} \\ \frac{\partial^2\chi^2}{\partial U\partial I} & \frac{\partial^2\chi^2}{\partial U\partial Q} & \frac{\partial^2\chi^2}{\partial U^2} \end{pmatrix} \tag{4.5.14}$$

with

$$\frac{\partial^2\chi^2}{\partial I^2} = \sum \frac{t_k^2}{4\sigma_k^2} \qquad \frac{\partial^2\chi^2}{\partial Q^2} = \sum \frac{t_k^2}{4\sigma_k^2}\epsilon_k^2\,\cos^2 2\phi_k \qquad \frac{\partial^2\chi^2}{\partial U^2} = \sum \frac{t_k^2}{4\sigma_k^2}\epsilon_k^2\,\sin^2 2\phi_k$$
$$\frac{\partial^2\chi^2}{\partial I\partial Q} = \frac{\partial^2\chi^2}{\partial Q\partial I} = \sum \frac{t_k^2}{4\sigma_k^2}\epsilon_k\,\cos 2\phi_k \qquad \frac{\partial^2\chi^2}{\partial I\partial U} = \frac{\partial^2\chi^2}{\partial U\partial I} = \sum \frac{t_k^2}{4\sigma_k^2}\epsilon_k\,\sin 2\phi_k$$
$$\frac{\partial^2\chi^2}{\partial Q\partial U} = \frac{\partial^2\chi^2}{\partial U\partial Q} = \sum \frac{t_k^2}{4\sigma_k^2}\epsilon_k\,\sin 2\phi_k, \cos 2\phi_k$$

While in principle the inversion of this matrix can be calculated analytically, it is probably easier to carry out the matrix inversion numerically, having first evaluated the various sums of terms required.

5. The OPTIMA-Burst Campaign

5.1. γ-ray Bursts

The goal of the OPTIMA-Burst project is to measure optical GRB-afterglow light-curves with high time-resolution quickly after the burst. For this purpose, OPTIMA was mounted at the 1.3 m-telescope of the Skinakas observatory for a total duration of 313 nights over four campaigns. In the *Swift* era, well-localized GRBs are detected at a rate of roughly one GRB every 3.4 days. During the 313 nights of OPTIMA-Burst campaigns, a total of 98 GRBs were detected and promptly localized by *Swift* and various other satellites, an average of one prompt GRB trigger every 3.2 days.

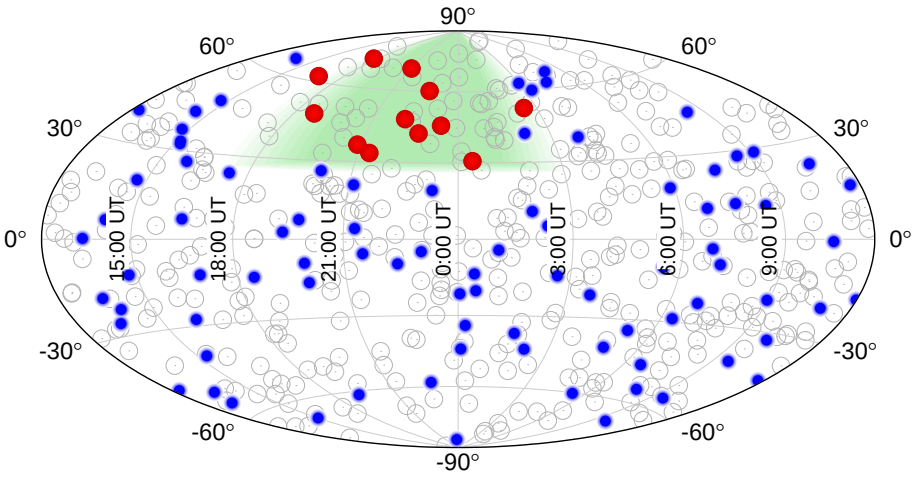

Figure 5.1.: Observatory-local all-sky map of *Swift* GRBs. In this map, the UTC time of a burst is plotted against its altitude in the sky at the time of burst for a specific location. Shown in green is the approximate region of sky promptly accessible from SKO. Shown in blue are all *Swift* GRBs that occurred during an OPTIMA-Burst campaign. Shown in red are the GRBs that were promptly reachable. For reference, all *Swift* GRBs that did not occur during an OPTIMA-Burst campaign are added to the plot in light grey. It is obvious that only a small fraction of GRBs can be promptly reached.

For a ground-based observatory, not all of these triggers are promptly observable, as the Sun needs to be below the horizon and the burst above the horizon at the location of the observatory. In reality, the actual limits are even more strict: Due to the earth's atmosphere, the sky is only sufficiently dark for astronomical observations once the Sun is more than 12°-18° below the horizon. Furthermore, the earth's atmosphere degrades observing conditions. The larger the airmass X the light from an object has to pass through before reaching the observatory, the worse the degradation is. The airmass can

be parametrized[1] using the altitude *alt* of an object by $X = 1/\sin(alt)$. At an airmass of more than ≈ 2, i.e. an altitude below 30°, the degradation of observing conditions very quickly reaches critical levels.

Both factors severely limit the number of GRBs promptly observable by an earth-bound observatory. To visualize this restriction, it is instructive to map the reachable sky on a suitably parametrized all-sky map of all GRBs. One suitable mapping is plotting the UTC[2]-time of a burst against the local altitude of the burst at the time it occurred. By choosing this parametrisation, an observatory-local all sky map can be achieved. In this plot, shown in Fig. 5.1, the local-time limits imposed by dusk and dawn[3], and the altitude limits imposed by the airmass can be plotted over the set of GRBs. A GRB falling within the area thus marked, can in principle be reached at the time of the burst.

Choosing an area-preserving projection like the Hammer-Aitoff-Projection[4], the observatory-local all-sky map can be used to intuitively assess the probability of an arbitrary GRB being promptly observable. It becomes immediately obvious that the number of bursts promptly observable from a ground-based observatory must always be severely limited. Also, it can be seen that the sample of GRB triggers produced by *Swift* during the OPTIMA-Burst campaigns has no strong bias with respect to trigger time and burst position.

In the course of 313 nights of OPTIMA-Burst campaign, a total of 12 GRB triggers were promptly reachable, slightly more than one trigger per month. Not all of these triggers were observed with equal success. While some triggers occurred during periods of bad weather or technical difficulties, and some could be reacted to but did not result in successful observations, several triggers were successfully observed.

In the following, the twelve GRBs promptly reachable by OPTIMA-Burst at SKO are discussed in detail.

5.2. Successful Observations

Of the twelve promptly reachable GRB triggers, four resulted in successful observations. Two of these were successful observations in photon counting mode, two were CCD-based observations. The two CCD-based observations can be considered successful not only because of the intrinsic value of the CCD-based light-curves, but also because APD-based observations were only precluded by bad luck. The data taken by OPTIMA-burst and other observatories for these bursts demonstrated the feasibility of the OPTIMA-Burst project in the first-year campaign.

In the following, the four triggers successfully observed will be reported in order of importance of their results.

[1] This simple parametrization of the airmass assumes a plane-parallel atmosphere. For altitudes below $5° - 10°$, more sophisticated approaches need to be taken. See e.g. [Young, 1994]

[2] Coordinated Universal Time

[3] As the four OPTIMA-Burst campaigns spanned months between May and November, the times of dawn and dusk are not constant over the whole OPTIMA-Burst dataset. This is indicated by lighter shades of green towards the dawn and dusk lines.

[4] The Hammer-Aitoff Projection is defined by:

$$x = \frac{2 \cdot \sqrt{2} \cdot \cos(\phi) \cdot \sin\left(\frac{\lambda}{2}\right)}{\sqrt{1 + \cos(\phi) \cdot \cos\left(\frac{\lambda}{2}\right)}} \qquad y = \frac{\sqrt{2} \cdot \sin(\phi)}{\sqrt{1 + \cos\phi \cdot \cos\left(\frac{\lambda}{2}\right)}}$$

with ϕ the longitude (here: UT trigger time) and λ the latitude (here: altitude at trigger time). It is an equal-area projection like the Mollweide projection, but produces less distortions.

5.2.1. GRB 070610 a.k.a. SWIFT J195509.6+261406

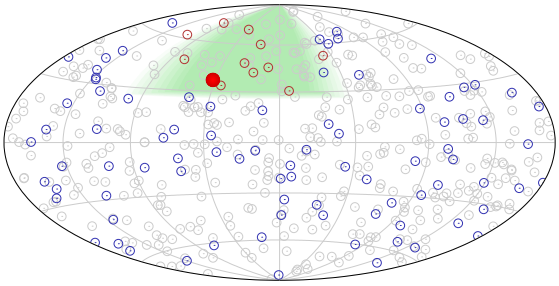

GRB parameters	
Burst time (t_0)	2007-06-10 UT 20:52:26
Burst coordinates	$19^h55^m10^s$ $+26°14'06''$
XRT start	t_0+3.2 ks

Observing conditions at t_0			
Airmass	1.66	Sun distance	117°
Moon distance	76°	Moon phase	24%

The detection of GRB 070610 by the BAT[5] instrument aboard *Swift* at 20:52:26 occurred during good observing conditions at SKO. OPTIMA-Burst promptly reacted and slewed the telescope onto the field of the burst 57 s after the burst. An optical transient was identified and positioned onto the photometry fibre bundle 421 s after the burst. After the early afterglow behaviour was uncharacteristic for a GRB, it was soon speculated that GRB 070610 was not a γ-Ray Burst, but a galactic transient [Kann et al., 2007]. Later refined analysis of the behaviour of the X-ray counterpart confirmed this [Pagani et al., 2007b] [Markwardt et al., 2007]. The source was therefore officially designated the name SWIFT J195509.6+261406 (hereafter shortened to J1955).

The OPTIMA-Burst observations of this source have revealed a very unusual optical source showing very short and extremely bright flares. The unique capability of OPTIMA-Burst to let the observer choose the integration time of an observation post-facto during data analysis proved to be essential in the observation of J1955, as this allowed to probe and resolve the variability of the target. A full description of the observation, data-analysis and interpretation of J1955 is given in Chapter 6.

5.2.2. GRB 090726

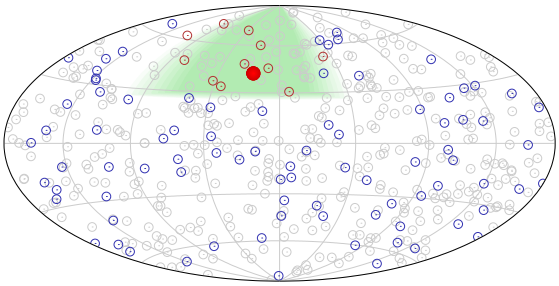

GRB parameters	
Burst time (t_0)	2009-07-26 UT 22:42:27
Burst coordinates	$16^h35^m16^s$ $+72°52'15''$
XRT start	t_0+49 min

Observing conditions at t_0			
Airmass	1.50	Sun distance	80°
Moon distance	91°	Moon phase	30%

GRB 090726 was a long GRB localized by *Swift*/BAT with a gamma-ray light-curve that shows a single weak peak with a maximum at $t - t_0 \sim 5$ s and $T_{90} = 67 \pm 15.2$ s $(15 - 350$ keV). The time-averaged spectrum of the prompt emission can be fit by a simple power-law of index 2.25 ± 0.19, and a fluence of $8.6 \cdot 10^{-7}$ erg/cm^2 $(15 - 150$ keV) [Krimm et al., 2009]. The redshift of GRB 090726 was deduced as $z = 2.71$ by optical spectroscopy using the 6 m SAORAS[6] telescope [Fatkhullin et al., 2009].

At SKO, GRB 090726 occurred roughly three hours before the onset of dawn twilight under favourable weather conditions. Due to an Earth limb constraint, Swift could not

[5] Burst Alert Telescope
[6] Special Astrophysical Observatory of the Russian Academy of Science

promptly slew to GRB 090726 until 49 minutes after the burst, therefore the position uncertainty of the trigger was 3′. OPTIMA reacted promptly to the trigger, and automatically slewed to the BAT position. CCD-based observations commenced at UT[7] 22:44:53, 146 s after the burst. Due to the initial lack of XRT[8] position, identification and final acquisition of the optical counterpart took until UT 22:56:37, 14 minutes after the burst.

A brief interruption occurred at the reception of the *Swift* XRT position update, as the OPTIMA-Burst operator moved the telescope pointing to the XRT position, away from the actual OT. Therefore, the OPTIMA light-curve shown in Fig. 5.2 is split into two epochs, the first beginning ~ 980 s after the burst and lasting 2.2 ks, the second beginning 6.4 ks after the burst an lasting 4.4 ks.

In order to have constant bin sizes in a log-log plot as shown in Fig. 5.2 the raw data was time-binned with bin sizes scaling with t. The time of the total data-set (roughly 12.7 ks) was divided into 500 time-bins, ranging from ~ 1.25 s to ~ 116 s in length, a relative time resolution of $\Delta t/t \sim 10^{-3}$. Of these 500 bins, 134 bins lie in the good-time intervals of one of the two epochs. Using this technique, the power-law decay apparent in the optical light-curve can be reliably traced down to count-rates of only a few tens of ct/s, making this the faintest successful OPTIMA detection at fainter than 21 mag, despite the encroaching dawn rising to a background of ~ 3800 ct/s

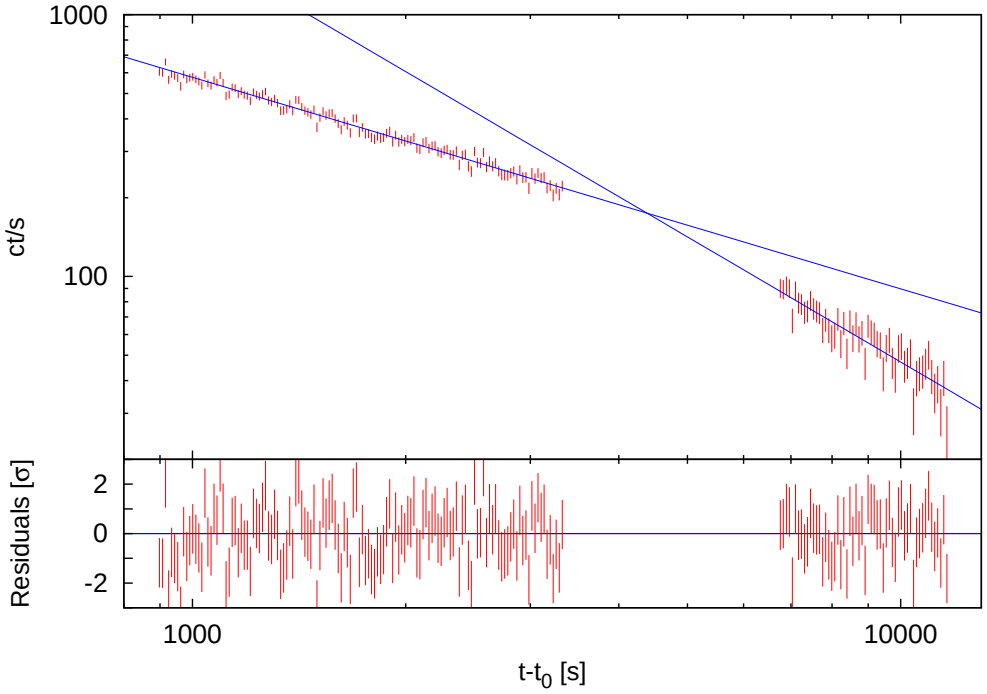

Figure 5.2.: OPTIMA light-curve of GRB 090726. Shown in red are OPTIMA data-points, shown in blue are two independent power-law fits. The decay indices of the two fits are $\alpha_1 = 0.81 \pm 0.01$ and $\alpha_2 = 1.5 \pm 0.1$. The resulting break time calculated from the fits is $t_{\mathrm{break}} = 4200 \pm 400$ s.

The two epochs of optical high-time-resolution data binned up in this way can be well

[7]Universal Time
[8]X-Ray Telescope

fit individually by one simple power-law for each epoch defined as $F \propto t^{-\alpha}$. There is no statistical indication for more variability, with $\chi^2/\text{d.o.f.}_1 = 0.99$ and $\chi^2/\text{d.o.f.}_2 = 0.97$ respectively. The time-indices of the power-law decays are $\alpha_1 = 0.81 \pm 0.01$ and $\alpha_2 = 1.5 \pm 0.1$. The resulting break time calculated from the two fits is $t_{\text{break}} = 4200 \pm 400$ s, however the break itself is not covered by the OPTIMA light-curve.

Comparison to other Observations

The afterglow of GRB 090726 was observed by several other observatories, ranging from very early data-points capturing the initial brightening [Maticic and Skvarc, 2009] of the afterglow and a plateau phase during which strong variability and flares have been claimed [Šimon et al., 2010], covering the break-time as estimated from OPTIMA data to a late-time data-point [Moskvitin et al., 2009a] [Volnova et al., 2009]. Fig. 5.3 shows a combined light-curve from all available optical and X-ray data. The flux-calibration of the OPTIMA count-rate light-curve was performed using data from the SAORAS data-set, as this data-set overlaps both OPTIMA epochs. It becomes apparent that the OPTIMA light-curve is in good agreement with the overall optical light-curve. Notably, the power-law decay fitted to the second epoch of OPTIMA data connects very well to the late-time data-point by CrAO[9] (which was not included in the fit).

However, while the OPTIMA light-curve overall agrees quite well with the other observations, there are some important differences.

As can be seen in Fig. 5.3, the slope of the power-law decay of the X-ray light-curve as observed by XRT ($\alpha_{\text{XRT}} = 1.29$) is incompatible with the slope of the simultaneous optical OPTIMA light-curve, and hence also would also not connect the bulk of the optical observations with the late-time data-point from CrAO. Also, the XRT light-curve shows no evidence of a break at the break-time deduced from the OPTIMA data ($t_{\text{break}} = 4200 \pm 400$ s) or later. While a break in the X-ray light-curve at earlier times can't be excluded, the observed X-ray – optical behaviour cannot, as reported in the literature [Šimon et al., 2010], be described as achromatic, hence the break observed in the optical cannot be a jet-break.

Fig. 5.4 shows a detail of the light-curve shown in Fig. 5.3, in which the transition from the plateau phase to the power-law decay phase of the afterglow of GRB 090726 can be seen. The OPTIMA light-curve shows a smooth power-law decay that agrees well with the light-curve from the RAS SAO 1 m telescope. For the Ondrejov 0.5 m light-curve, data-points taken after about 1300 s after the burst agree quite well with the OPTIMA power-law decay, besides one small dip in the Ondrejov light-curve. The Crni Vrh data and the Ondrejov data before ~ 1300 s strongly diverge from the smooth power-law seen in the OPTIMA data, showing dips in the light-curve and a general variability not seen in the OPTIMA data. As the Crni Vrh and Ondrejov light-curves do not agree with each other and dips can be explained more easily due to atmospheric variability than the emergence of a smooth powerlaw, it is very probable that the Crni Vrh and Ondrejov light-curves are unreliable during the plateau phase.

Astrophysical Interpretation

Since the full dataset including the OPTIMA-Burst data clearly shows a break in the optical at a time incompatible with the break time of the X-ray light-curve (Fig. 5.3), the

[9] Crimean Astrophysical Observatory

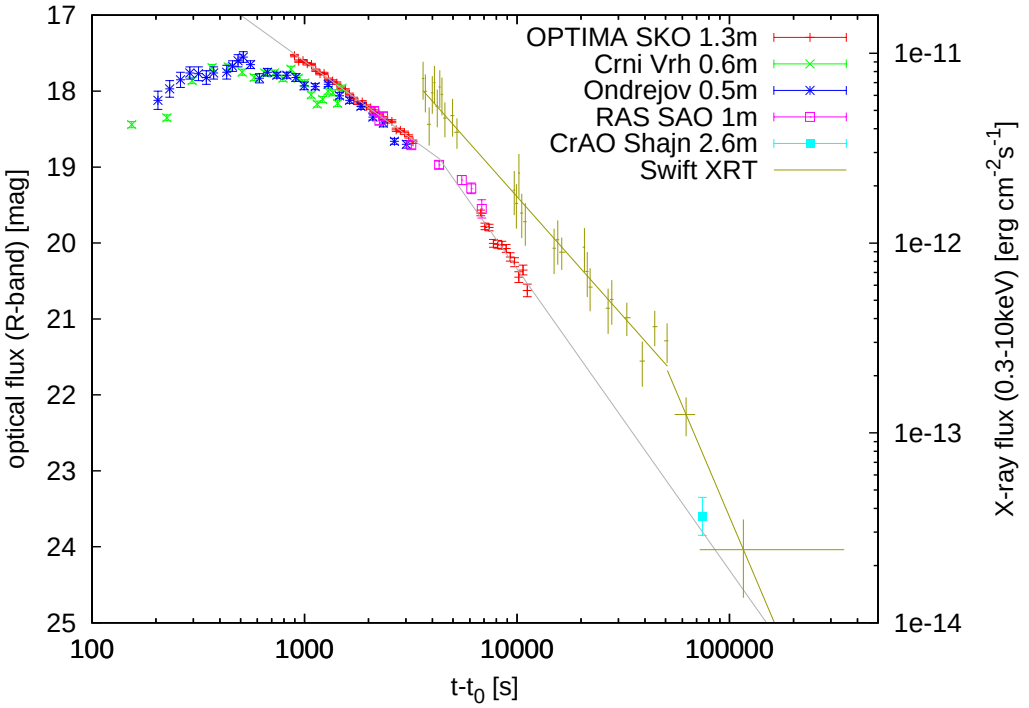

Figure 5.3.: Overview over all optical and X-ray observations of the afterglow of GRB 090726, comparing the OPTIMA data to data from the Crni Vrh 0.6 m telescope [Maticic and Skvarc, 2009], from the D50 telescope in Ondrejov [Šimon et al., 2010], the 1 m RAS SAO telescope [Moskvitin et al., 2009a], the CrAO 2.6 m Shajn telescope [Volnova et al., 2009] and XRT (automatically generated light-curve for trigger 358422 [Evans et al., 2007, Evans et al., 2009]). Galactic extinction of $A_R = 0.12$ mag [Schlegel et al., 1998] is not corrected.

canonical interpretation of the break as jet-break with a corresponding Lorentz-factor at break time of $\Gamma_{break} \sim 20$ [Šimon et al., 2010] is problematic.

In the *Swift*-era confusing non-canonical multi-wavelength GRB afterglow light-curves such as the one of GRB 090726 have become the norm. Often, a "steep – flat – steep" behaviour is observed, with a rapid decline in the initial X-ray light-curve, followed by a flatter or plateau phase, and a second steep decline. Additionally, X-ray flares of relatively short duration ($\Delta t/t \sim 0.1$) are observed up to several hours after the burst in almost half the afterglows observed. The optical light-curves frequently are also complex, but often do not track the X-rays, suggesting a different origin [Panaitescu et al., 2006, Panaitescu, 2007a, Panaitescu, 2007b]

In recent years, approaches to unify the description of complicated light-curves have been proposed. One such description parametrizes the combined IR/optical and X-ray afterglow as sum of two components: the canonical afterglow emission from the forward shock [Panaitescu and Kumar, 2000] due to the interaction of a fireball with the circumburst medium, plus an additional "late prompt" component [Ghisellini et al., 2009]. In this model no attempt is made to physically explain the late prompt component, but in order to make a full theoretical description easier to achieve later on it is still parametrized

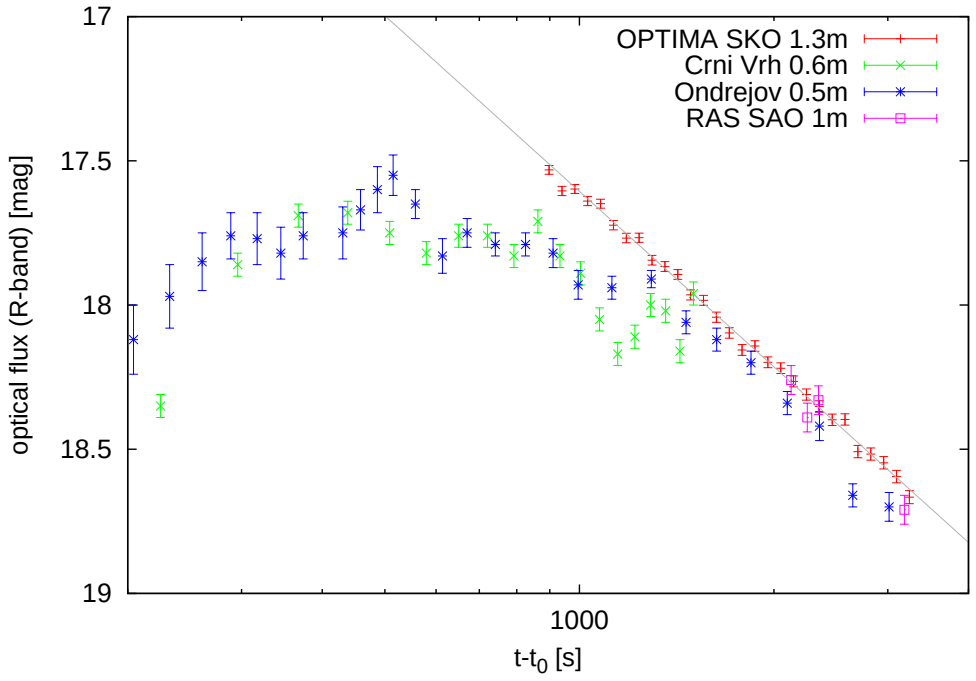

Figure 5.4.: Light-curve of transition from plateau phase to power-law decay of GRB 090726. It is apparent that during the decay phase, all observations are consistent with OPTIMA-data, but diverge at the plateau-decay transition.

in a purely phenomenological fashion: The spectral shape is described by a broken power-law with no temporal evolution, while the temporal evolution is achromatically described using a broken power-law. It should be noted, that the temporal break in the late prompt component is not necessarily the same as any breaks observed in the X-ray and/or optical light-curves.

Depending on the parametrization, the X-ray and optical regimes can independently be dominated by either the canonical afterglow component, or the late prompt component. Using these two components, a wide variety of optical and X-ray light-curves can be modeled. In particular, it is easy to create achromatic breaks in the afterglow light-curve with this model. While not enough multi-wavelength data is available to fully analyze GRB 090726 with this model (there is not enough information available on host absorption), it can be speculated that the shallower X-ray light-curve and later break-time in the X-ray regime are due to a dominating late prompt component in the X-rays.

5.2.3. GRB 060904B

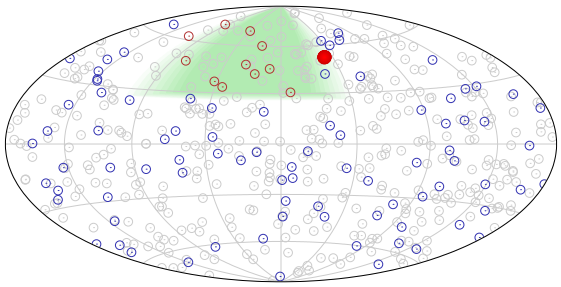

GRB parameters	
Burst time (t_0)	2006-09-04 UT 02:31:03
Burst coordinates	$03^h52^m51^s$ $-25°09'00''$
XRT start	t_0+69 s

Observing conditions at t_0			
Airmass	1.27	Sun distance	105°
Moon distance	121°	Moon phase	82%

GRB 060904b was detected by *Swift* BAT as a double-peaked event, consisting of one 9 s long FRED pulse 2 s before t_0, followed by a weaker 100 s long flare starting at $t_0 + 120$ s. [Grupe et al., 2006] [Markwardt et al., 2006]. Optical afterglow observations commenced very early on, with ROTSE, TAROT[10] and the Crni Vrh observatory catching the afterglow before the end of the prompt γ-ray emission.

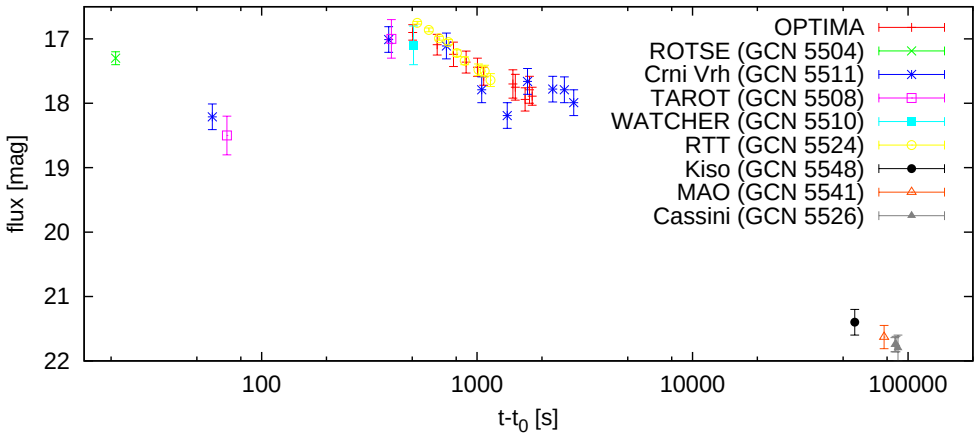

Figure 5.5.: Light-curve of GRB 060904b. Many data-points from the literature are shown here alongside the OPTIMA CCD light-curve. Although OPTIMA could not take a light-curve with high time resolution, the excellent sampling of the GRB 060904b dataset made this the most successful GRB observation of the 2006 OPTIMA-Burst campaign.

On SKO, GRB 060904b occurred shortly before dawn, when the Sun was already 17° below the horizon. Because of a severed submarine cable, UoC (and with it also SKO) was disconnected from the internet at the time. The trigger notification for GRB 060904b was therefore only received by text message on a mobile phone, and had to be entered into the OPTIMA-Burst system manually. The position updates from XRT were not received on the mobile phone. Due to this, the start of CCD observations was delayed by several minutes, the OT could not be promptly identified, and only CCD observations were performed.

[10]Télescopes à Action Rapide pour les Objets Transitoires

Fig. 5.5 shows a combined light-curve of the OPTIMA CCD data and literature data from several other observatories. The afterglow light-curve is very well sampled, and shows a bright early optical flash observed by ROTSE, followed by a drop in magnitude and a gradual brightening in the prompt phase of the burst, followed by a power-law decay. At approximately $t - t_0 = 2000$ s, a strong optical plateau is apparent, which can be interpreted as indication of late energy injection[Klotz et al., 2008].

Even though GRB 060904b could not be observed with high time resolution with OPTIMA-Burst due to the aforementioned internet outage, much of the complex variability shown by the early light-curve was in principle accessible to OPTIMA-Burst, proving the feasibility of OPTIMA-Burst. The CCD dataset taken by OPTIMA was the most significant GRB related result of the 2006 OPTIMA-Burst campaign.

5.2.4. GRB 060926

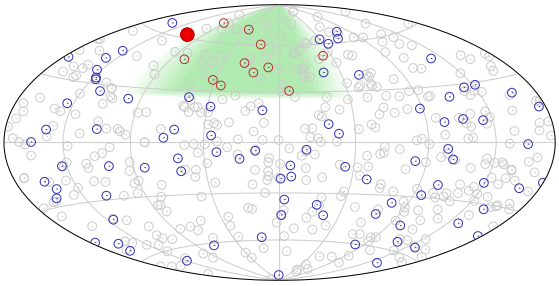

GRB parameters	
Burst time (t_0)	2006-09-26 UT 16:48:41
Burst coordinates	$17^h35^m49^s$ $+13°02'29''$
XRT start	t_0+60 s

Observing conditions at t_0			
Airmass	1.13	Sun distance	81°
Moon distance	52°	Moon phase	15%

GRB 060926 was a GRB detected by *Swift* BAT as a FRED shaped peak of $T_{90} = 8$ s duration [Holland et al., 2006] [Cummings et al., 2006]. At SKO, it occurred during evening twilight: At the time of the burst, the Sun was only 8.5° below the horizon. OPTIMA started observations as soon as the sky brightness was low enough to not damage the APD detectors – 36 minutes after the burst, when the Sun had reached 17° below the horizon. As an XRT error-circle was available, the afterglow was quickly identified, however since the OT had decayed to > 20 mag by that time, it was deemed to dim for high-time-resolution observations, and only a CCD light-curve was taken.

At the site of the MASTER[11] observatory 18° east of Crete near Kislovodsk, Russia, astronomical dusk had already ended at the time of the GRB, with the Sun 20° below the horizon. MASTER began observations 91 s after the burst, and observed a flare of about 18 mag brightness several hundred seconds after the burst [Lipunov et al., 2008c] – easily reachable by OPTIMA-Burst but for the dusk time.

5.3. Successful Trigger Reactions with Non-Detection

Four of the twelve promptly reachable GRB triggers during all OPTIMA-Burst campaigns were successfully observed, but their observation resulted in non-detections. Three of these upper limits were confirmed or later improved upon by other observatories, indicating that most probably these burst did not actually show an optical transient. One of the non-detections was however only due to bad sky conditions.

The four observations will be described in chronological order below.

[11] Mobile Astronomical System of the TElescope-Robots

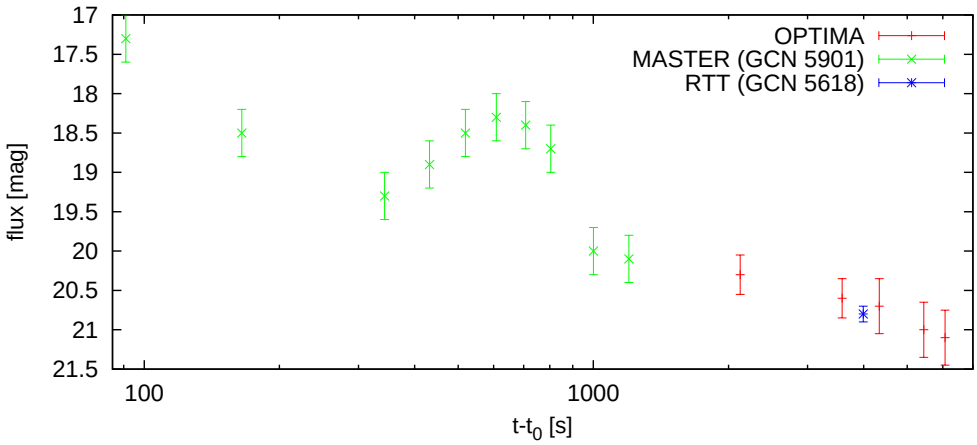

Figure 5.6.: Light-curve of GRB 060926. Literature data from MASTER and RTT are shown besides OPTIMA CCD data points. Because of evening twilight, OPTIMA could not promptly observe the GRB afterglow. The MASTER data shows a prominent optical flare, well within reach for OPTIMA but for the dusk time.

5.3.1. GRB 081102

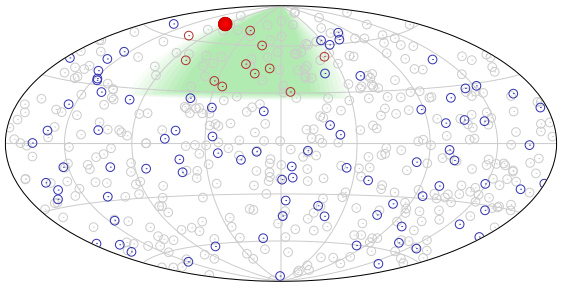

GRB parameters	
Burst time (t_0)	2008-11-02 UT 17:44:39
Burst coordinates	$22^h04^m44^s$ $+52°59'36''$
XRT start	t_0+92 s

Observing conditions at t_0			
Airmass	1.05	Sun distance	116°
Moon distance	95°	Moon phase	20%

GRB 081102 was a 40 s long GRB with complex γ-ray light-curve detected by *Swift*. OPTIMA-Burst reacted and started CCD observations, quickly switching to a long APD observation of the XRT error-circle. However, only an upper limit of 18.5 mag could be derived due to poor November sky conditions. The upper limits of OPTIMA were corroborated by upper limits in the literature [Lipunov et al., 2008a] [Lipunov et al., 2008b] [Khamitov et al., 2008].

5.3.2. GRB 090621B

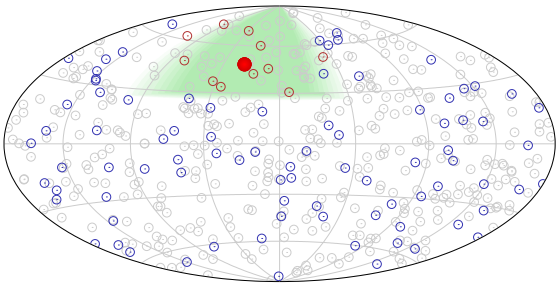

GRB parameters	
Burst time (t_0)	2009-06-21 UT 22:07:25
Burst coordinates	$20^h53^m44^s$ $+69°00'48''$
XRT start	t_0+70.7 s

Observing conditions at t_0			
Airmass	1.35	Sun distance	83°
Moon distance	77°	Moon phase	1%

GRB 090621B was a short GRB detected by *Swift*, consisting of a single spike with a duration of less than 128 ms. OPTIMA-Burst observed the XRT error-circle, starting 91 s after the burst. No optical counterpart could be identified, the limiting magnitude was 20.0 mag. Deeper observations in the literature found OT candidates, but could not establish their status as optical/nIR[12] counterpart [Levan et al., 2009] [Galeev et al., 2009] [Cenko et al., 2009] [Berger et al., 2009].

5.3.3. GRB 090628

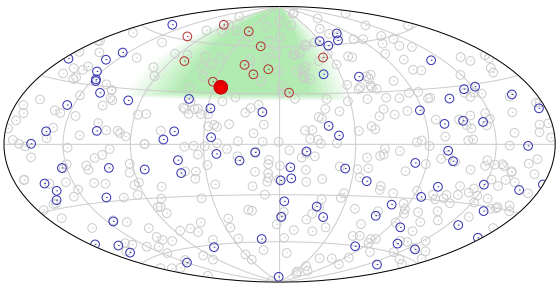

GRB parameters	
Burst time (t_0)	2009-06-28 UT 21:20:12
Burst coordinates	$15^h48^m12^s$ $-15°58'36''$
XRT start	t_0+45 min

Observing conditions at t_0			
Airmass	1.81	Sun distance	141°
Moon distance	60°	Moon phase	44%

GRB 090628 was detected by *Swift* BAT as a $T_{90} = 20.1 \pm 4.6$ s Burst with a weak, 1 s precursor about 7.5 s before the main burst. Due to an Earth limb constraint, *Swift* could not promptly slew and started XRT observations only about 45 minutes after the burst [Mangano et al., 2009].

OPTIMA-Burst could not identify an optical counterpart in the BAT error-circle. Later analysis of the region of the XRT error-circle showed no detectable source, with an upper limit of 20 mag. Upper limits by CAHA ($R > 22$ [Kubanek et al., 2009]), GROND[13] ($g' > 23.7$, $r' > 24.0$, [Kruehler et al., 2009]) and SAORAS (19.3 mag [Moskvitin et al., 2009b]) confirm the OPTIMA non-detection.

[12] Near Infra-Red
[13] Gamma-Ray Burst Optical/Near-Infrared Detector

5.3.4. GRB 090727

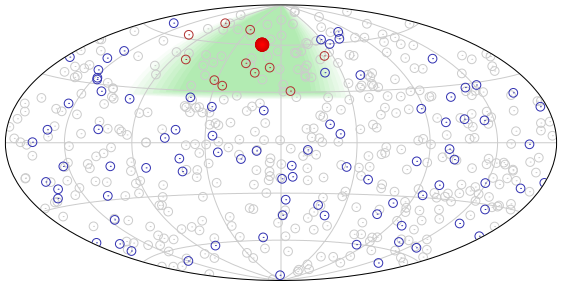

GRB parameters	
Burst time (t_0)	2009-07-27 UT 22:42:18
Burst coordinates	$21^h03^m53^s$ $+64°54'58''$
XRT start	t_0+87.9

Observing conditions at t_0			
Airmass	1.15	Sun distance	96°
Moon distance	114°	Moon phase	40%

GRB 090727 was a 25 s long GRB detected by *Swift*/BAT. The 2 m Liverpool Telescope started robotic observations 2 minutes after the burst and detected the afterglow in a crowded field [Smith and Mundell, 2009]. Within the first 100 minutes, the Liverpool Telescope detected a $r' = 19.4$ flare in the early optical light-curve, with a subsequent plateau phase and break [Smith et al., 2009].

OPTIMA-Bursts reacted promptly to the burst and arrived at the field approximately 90 s after the trigger, and started fibre-fed observations 12 minutes after the burst. Due to the adverse observing conditions (stormy winds in observing direction, bad seeing and high humidity), the OT detection of the Liverpool Telescope could not be reproduced.

5.3.5. Upper Limit Astrophysical Context

Not for all GRBs afterglows can be successfully observed. While this was historically often attributed to observational constraints, in the *Swift* era with its abundance of robotic afterglow observatories, this explanation for these so-called "dark bursts" can be ruled out [Roming et al., 2006]. Between 25 % and 42 % of the observed bursts do not show an optical afterglow [Fynbo et al., 2009].

The reason for the low optical emission of dark bursts is still a mystery, but plausible explanations comprise foreground extinction, dust absorption in the host galaxy or extremely high redshift. In the scope of this work, however, the question of the nature of dark bursts is of less relevance than the question of whether a burst that was not detected by OPTIMA-Burst was a dark burst and thus undetectable, or whether OPTIMA-Burst *should* have been able to observe the burst under more favourable conditions.

For GRB 090727, this case is clear because of successful detection of the OT by the Liverpool Telescope (Chapter 5.3.4). The cases of the other three OPTIMA-Burst upper limits are more interesting, as other observatories have corroborated the OPTIMA-Burst upper limits. Fig. 5.7 shows a comparison of the upper limits of these three bursts as derived by OPTIMA-Burst and as reported in the literature with a large ensemble of GRBs [Kann et al., 2011]. For GRB 090621B and GRB 090628, the upper limits by OPTIMA-Burst and the literature indicate a high probability that they were true dark bursts: If they had an afterglow, it was amongst the very dimmest afterglows ever recorded.

For GRB 081102, the upper limits are less constraining. The November weather conditions over large parts of Europe were unfavourable, explaining why the upper limits reported by OPTIMA-Burst and two other European observatories are of relatively little significance. If GRB 081102 had an undetected afterglow, it could have been as bright as the darkest third of the test ensemble.

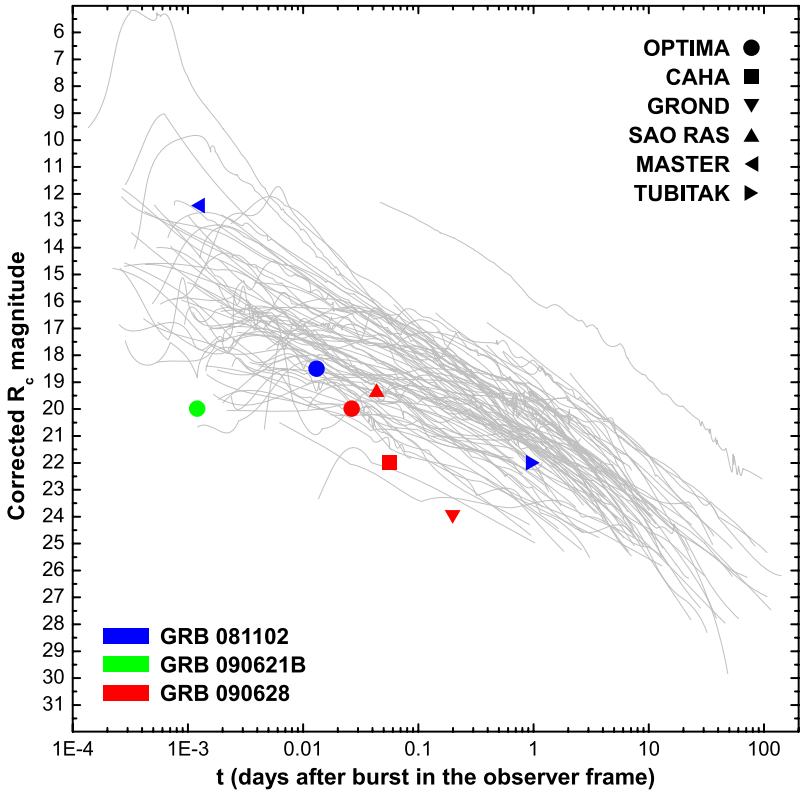

Figure 5.7.: Upper limits as determined by OPTIMA-Burst and other observatories for three burst. While for GRB 090621B and GRB 090628 the upper limits indicate dark bursts, the upper limits for GRB 081102 are not constraining. (Plot adapted from [Kann et al., 2011], references to data in Chapter 5.3.1 to 5.3.4)

For GRB 081102 the weather conditions over SKO and all other observatories reporting upper limits were very unfavourable, explaining the systematic low significance

5.4. Unsuccessful Triggers

Four of the twelve promptly reachable GRB triggers were not reacted to. In three cases, this was due to bad weather conditions, in one case due to a very long delay in sending out the trigger. While 25 % bursts missed due to weather conditions sound like SKO is not at a site well suited to optical astronomy, this number has to be taken with a grain of salt as the number of bursts lost to weather is only three – too low to reliably draw conclusions about the long-term weather statistics.

The four lost triggers will be very briefly described in chronological order below.

5.4.1. GRB 060901

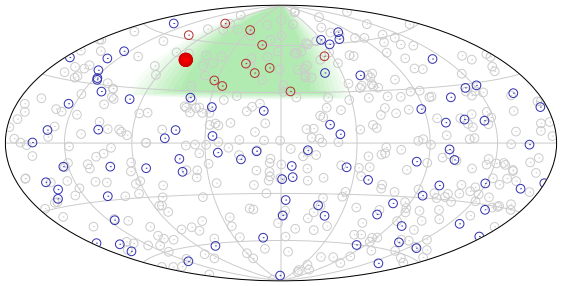

GRB parameters	
Burst time (t_0)	2006-09-01 UT 18:44:00
Burst coordinates	$19^h08^m38^s$ $-6°38'07''$
XRT start	t_0+3^h46^m

Observing conditions at t_0			
Airmass	1.34	Sun distance	127°
Moon distance	36°	Moon phase	59%

GRB 060901 was a 20 s long GRB detected by the IBAS[14] system. The trigger was circulated via GCN Circular at 19:53:34 UT, about 1^h9^m after the burst [Mereghetti et al., 2006]. The initial position error of the burst location as determined by INTEGRAL was 2.5′ and was improved to 4.9″ by XRT at 22:30 UT, 3^h46^m after the burst [Racusin et al., 2006]. Due to unfavourable weather conditions (rain and high humidity), SKO remained closed during the whole night and no data was taken.

5.4.2. GRB 070724B

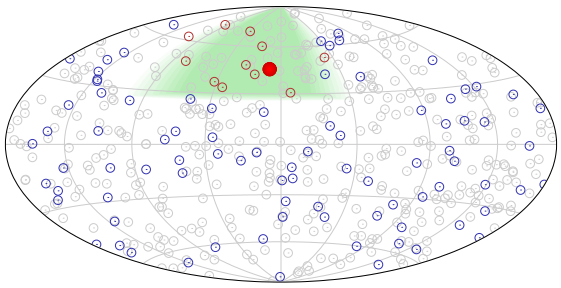

GRB parameters	
Burst time (t_0)	2007-07-24 UT 23:25:09
Burst coordinates	$01^h09^m57^s$ $+57°40'34''$
XRT start	t_0+$19^h7^m30^s$

Observing conditions at t_0			
Airmass	1.4	Sun distance	82°
Moon distance	138°	Moon phase	75%

GRB 070724b was the first ever GRB to be detected by AGILE[15] [Del Monte et al., 2008]. At the time of the burst, however, the on-board identification system of AGILE was still in its commissioning phase, and the burst notice was not automatically generated. The burst notice was distributed more than 19 hours after the burst, rendering the burst uninteresting for OPTIMA-Burst observations.

[14] Integral Burst Alert System
[15] Astro-rivelatore Gamma a Immagini Leggero

5.4.3. GRB 081028

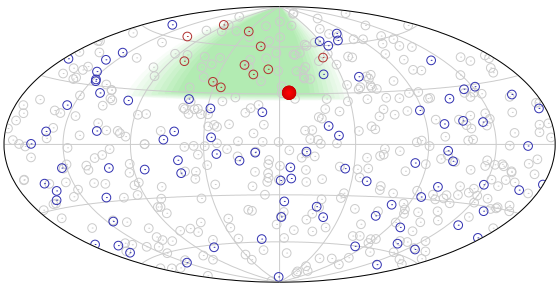

GRB parameters			
Burst time (t_0)	2008-10-28 UT 00:25:00		
Burst coordinates	$08^h07^m34^s$	$+02°18'40''$	
XRT start	t_0+191 s		
Observing conditions at t_0			
Airmass	1.98	Sun distance	91°
Moon distance	80°	Moon phase	1%

GRB 081028 occurred during a 6-night period of bad weather, during which no observations at SKO were possible. Normal operations were continued at SKO one night later.

5.4.4. GRB 090715B

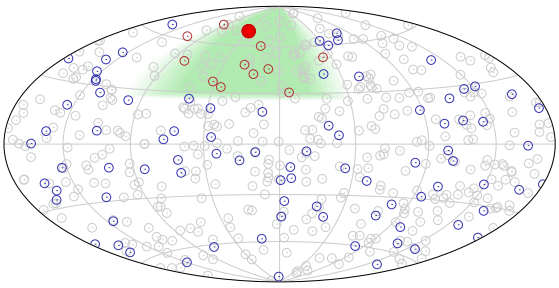

GRB parameters			
Burst time (t_0)	2009-07-15 UT 21:03:14		
Burst coordinates	$16^h45^m23^s$	$+44°49'36''$	
XRT start	t_0+46 s		
Observing conditions at t_0			
Airmass	1.06	Sun distance	103°
Moon distance	107°	Moon phase	45%

GRB 090715B occurred during a bad weather period of three nights duration, and could not be observed. Normal operation at SKO resumed on 2009-07-17.

6. Observations of SWIFT J195509.6+261406

The OPTIMA-Burst instrument (Chapter 3) combines the fast reaction time of a robotic GRB afterglow observatory with the capabilities of a dedicated high time-resolution instrument. Of the 12 prompt triggers in 313 nights of the OPTIMA-Burst campaigns (Chapter 5), the observation of GRB 070610 a.k.a. SWIFT J195509.6+261406 is especially well suited to demonstrate not only the feasibility of the whole OPTIMA-Burst project, but also the benefit offered by the unique combination of properties. In particular, the capability of allowing to dynamically select the time-resolution post-facto in response to the observed light-curve allowed to not only detect, but also resolve the unprecedented optical flaring activity of this source.

6.1. Discovery

At 20:52:26 UT on June 10, 2007, BAT triggered on a possible GRB [Pagani et al., 2007a]. The light-curve of the initial burst consisted of one single burst of approximately 5 seconds duration (Fig. 6.1) Due to an Earth limb constraint, the *Swift* satellite could not slew

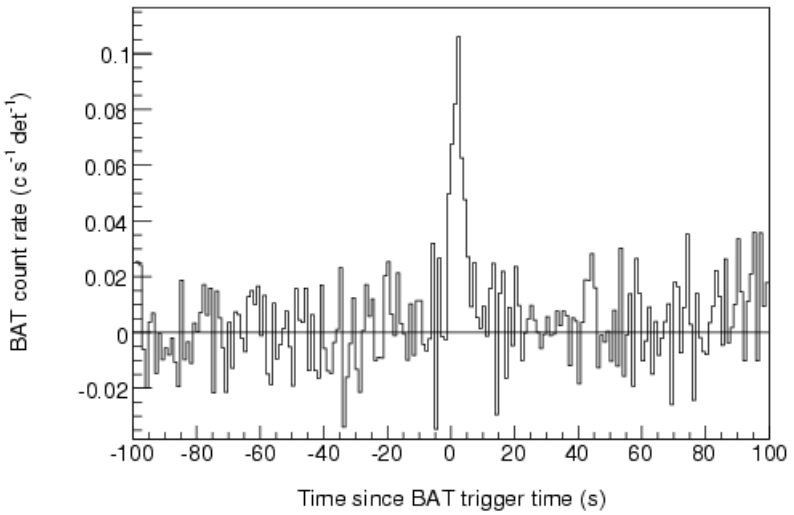

Figure 6.1.: *Swift* BAT light-curve of GRB 070610 [Kasliwal et al., 2008]

promptly to the BAT position, and follow-up observations by XRT and UVOT[1] were delayed by more than 50 minutes.

[1] UV and Optical Telescope

At the time the trigger was received, OPTIMA-Burst had just started to observe the polarimetric standard star VI Cyg 12, located only 17° away from the position of the trigger. Therefore, OPTIMA-Burst was able to begin observations of the field of GRB 070610 at 20:53:23 UT just 57 seconds after the burst, 28 seconds after the trigger notice.

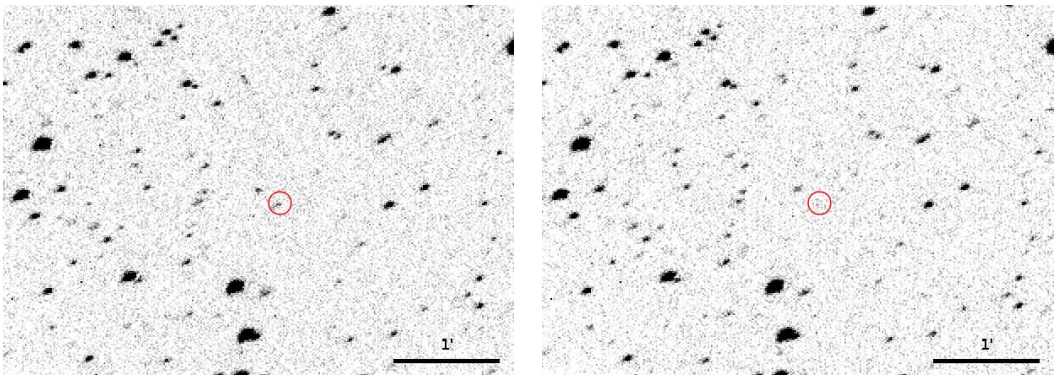

(a) (b)

Figure 6.2.: First detection images of GRB 070610/J1955. In panel (a) the optical transient can be seen near the detection limit within the red circle, in panel (b) it has faded from view 10 s later.

The trigger was located at a galactic latitude of $-1°$, in a field which therefore was very crowded. In the very first 10 s frame, a source was identified near the detection threshold that was not detected any more in subsequent images (Fig. 6.2). CCD-based observations continued for about three more minutes, until it was clear that this was the only candidate for a counterpart and photon-counting mode observations were prepared. At 20:59:27, 421 s after the burst, the good-time of the OPTIMA-Burst photon-counting observation of GRB 070610 began.

Quick-look analysis of the early light-curve of GRB 070610 revealed two bright, short flares very uncharacteristic of typical GRBs (Fig. 6.6). After quick publication of this behaviour as GCN Circular [Stefanescu et al., 2007b], it was soon speculated that GRB 070610 was not a γ-Ray Burst, but in fact a Galactic X-ray transient [Kann et al., 2007]. Later refined analysis [Pagani et al., 2007b, Markwardt et al., 2007] of the behaviour of the X-ray counterpart confirmed this. The source was therefore officially designated the name SWIFT J195509.6+261406 (hereafter abbreviated to J1955).

6.2. X-ray Analysis and Distance Estimates

Although J1955 was observable in the X-rays for 10 days, only one bright X-ray flare on the first day after the burst was observed (Fig. 6.3(b)). This is in stark contrast to the strong flaring activity shown by J1955 in the optical. The X-ray burst was symmetrical in nature, contrasting with the predominantly FRED shaped optical flares. During this 30 s burst, the X-ray flux increased by a factor of ~ 100 (from $\sim 10^{-11}$ erg cm^2 s^{-1} to $\sim 10^{-9}$ erg cm^2 s^{-1} in the XRTs $0.2 - 10$ keV energy band).

In reaction to the proposed galactic X-ray transient nature of J1955, a search for historic X-ray flares was performed in data from the ASM instrument aboard RXTE. The activity in the period around the GRB detected by *Swift* was clearly detected by ASM, and several

Spectrum	Param	value	N_{H} (10^{21} cm^{-2})	χ^2 (dof)
pow	index	1.67 ± 0.12	$9.9(+4.4/-3.1)$	1.055 (91)
brems	kT(keV)	10.4 ± 2.9	$8.3(+1.7/-1.4)$	1.052 (91)
bb+pow	indx/kT	2.6/1.4	$11.4(n/a)$	1.026 (89)
diskbb	Tin(keV)	1.97 ± 0.5	$5.9(+2.6/-1.9)$	1.074 (91)

Table 6.1.: Several X-ray spectral models fit to the combined dataset of J1955 XRT observations.

excesses above 3 σ were detected in the years prior to the 2007 outburst. However, taking into account the number of samples produced by ASM, the number of excesses was well below the 5 σ-level, hence no historic detection can be claimed.

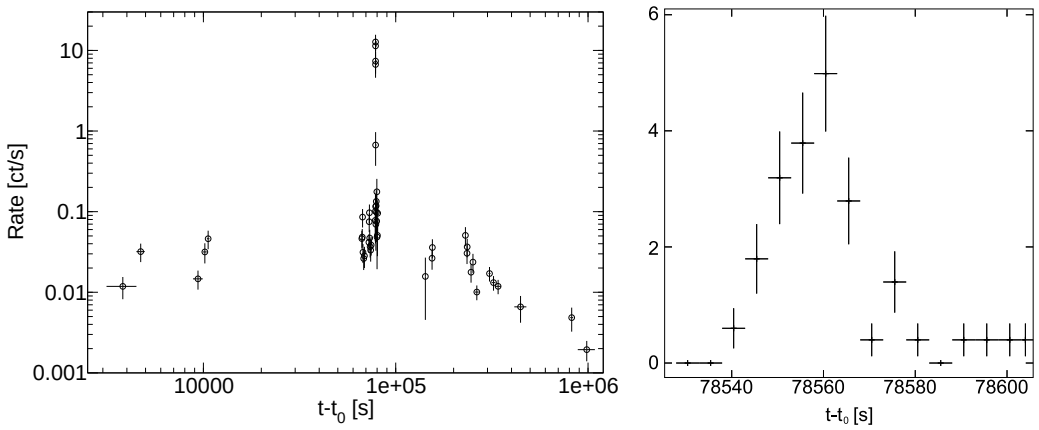

(a) (b)

Figure 6.3.: X-ray light-curve observed with *Swift* XRT.
Panel (a) shows an overview over the total light-curve.
Panel (b) shows the single bright X-ray flare in detail.

While the SNR of the spectrum is sufficient to fit a spectral model, it is not good enough to reliably distinguish between different spectral models. Different models were fit to the combined spectrum of all observations, all fitting equally well (table 6.1). As no model fits the data clearly better than the other models, the X-ray spectrum cannot in itself shed light on the type of object observed in J1955.

Besides interest in the emission process, a spectral fit in the X-ray regime allows to deduce the total absorption column N_{H}. Properly calibrated, this can be used as a distance indicator. While the absorption component of the spectral fits does vary between the different models, they are compatible within errors. In the following, the value for N_{H} derived by a simple power-law emission model is used, as this gives the most conservative distance estimates: $N_{\mathrm{H}} = 9.9^{+4.4}_{-3.1} \cdot 10^{21}$ cm^{-2}

In order to convert the X-ray absorption column to a distance estimate, it is necessary to map the absorbers along the line of sight. Different methods are in widespread use, e.g. directly measuring the density of neutral hydrogen gas clouds by their HI (21 cm) emission, or estimating the molecular hydrogen density by measuring the radio emission of associated CO molecules. For both of these measures, the distance information is

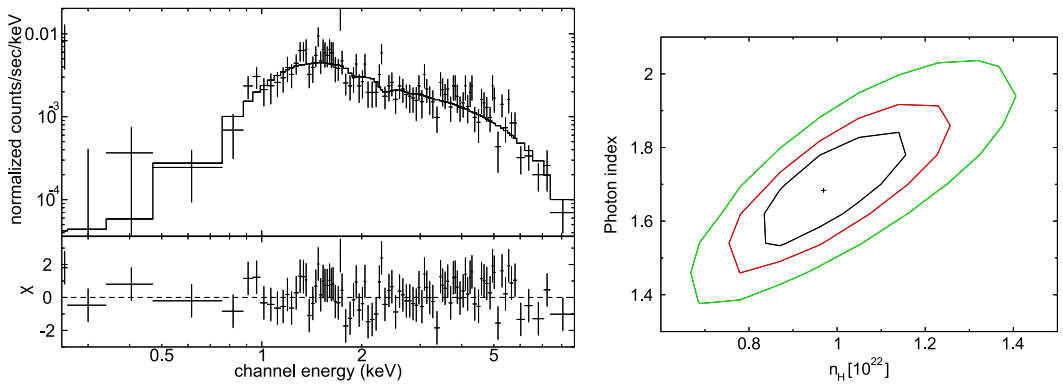

(a) (b)

Figure 6.4.: X-ray spectrum taken by XRT. The SNR is good enough for a reasonable fit, but not good enough to reliably distinguish between different spectral models. Shown here is a fit using a simple power-law spectral model.
Panel (a) shows the spectrum and the fit residuals.
Panel (b) shows the contour levels of the two fit parameters: photon index and absorption column

derived the measured Doppler shift of the radio emission lines and kinematic models of the Galaxy. This method does, however, leave geometric ambiguities in the interpretation of the derived distance.

Another method uses a calibration of optical extinction versus distance based on the so called "red-clump-stars" [Stanek and Garnavich, 1998]. The "red clump" is a feature of the Hertzsprung-Russell diagram, in which a lot of stars with similar magnitude and colour cluster.

The stars clustering in the red clump are Population I giants, the red clump can be considered the metal-rich counterpart of the asymptotic giant branch. While the individual magnitude and colour of the red-clump stars can vary significantly, the mean of the distribution within the red clump is highly predictable. Therefore, the red-clump can be used as a kind of "statistical standard candle", not only for magnitude, but also for colour. As the giant stars involved are quite bright numerous red-clump stars are to be expected in any Galactic field. Moreover, the red clump is readily identified in colour-magnitude diagrams, as soon as there's a sizeable population of stars plotted.

These facts make red-clump stars well suited to estimate the distance – absorption relation in a specific region of the galactic plane: In a colour-magnitude diagram, the distance of a star changes only the magnitude, while absorption changes magnitude and colour, therefore the red clump is smeared out into a skewed arm. Since the direction of the distance and absorption vectors are known, the loci of red clump stars can be decomposed into reddening/distance pairs, and as the red-clump stars are numerous and easy to identify, there is ample statistics in almost every field in the galactic plane [Durant and van Kerkwijk, 2006].

Using the value of $N_{\mathrm{H}} = 9.9^{+4.4}_{-3.1} \cdot 10^{21}\ \mathrm{cm}^{-2}$ derived from fitting a power-law spectral

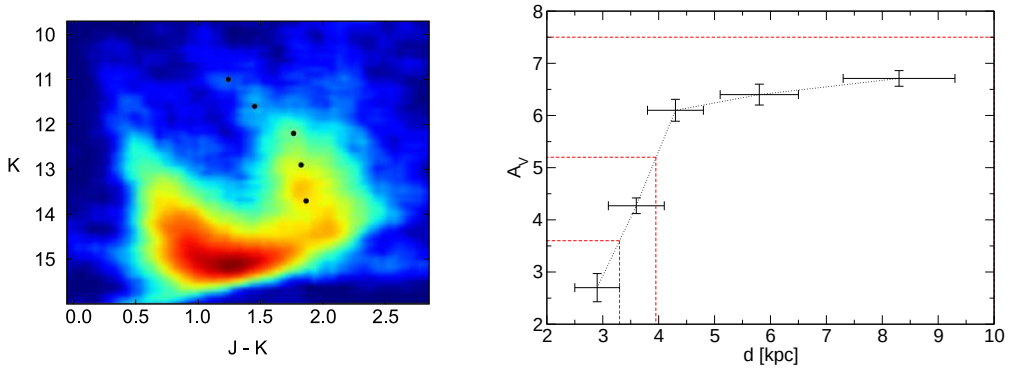

(a) (b)

Figure 6.5.: The red-clump method can be used to constrain the distance to J1955. Panel (a) shows a colour-magnitude diagram of $\sim$ 6000 stars in a 10′ region around J1955. The red clump stars are smeared out into an arm, several loci are marked with dots. In panel (b), the loci are decomposed into distance/absorption pairs. Using the hydrogen column N_{H} from the X-rays to estimate the optical absorption, the distance to J1955 can be constrained. [Castro-Tirado et al., 2008]

model to the X-ray spectra of J1955, an absorption of $A_V = 5.2^{+2.3}_{-1.6}$ can be estimated[2]. As becomes obvious from the absorption-distance plot (Fig. 6.5(b)), the large errors on the X-ray extinction give a poor constraint on the distance. A confident lower limit of 3.5 kpc can be given, the most probable distance lies at $4 - 5$ kpc, but the upper limit on the distance is basically unconstrained [Castro-Tirado et al., 2008].

6.3. Optical Light-Curves

After the two short flares observed in the first night that led to the recognition of J1955 as non-GRB source, OPTIMA-Burst observations in the second night showed more unexpected behaviour: Instead of a declining activity expected from a GRB afterglow, a dramatic increase in the number and brightness of the optical flares was observed [Stefanescu et al., 2007a] (Fig. 6.7). In the third night after the burst, the activity declined roughly to the amount of the first night, and after the fourth night, no further flares were observed with OPTIMA-Burst.

6.4. Flux Calibration

For comparison of OPTIMA light-curves with observations of other groups, the count-rates of the OPTIMA system must be converted to magnitudes. One way of doing this is by observing different photometric standard sources with OPTIMA, thus calibrating

[2]Using the relation between hydrogen column density N_{H} and extinction [Cardelli et al., 1989]

$$E(B-V) = N_{\mathrm{H}}/5.9 \cdot 10^{21}\ \mathrm{cm}^{-2}$$
$$A_V/E(B-V) = 3.1$$

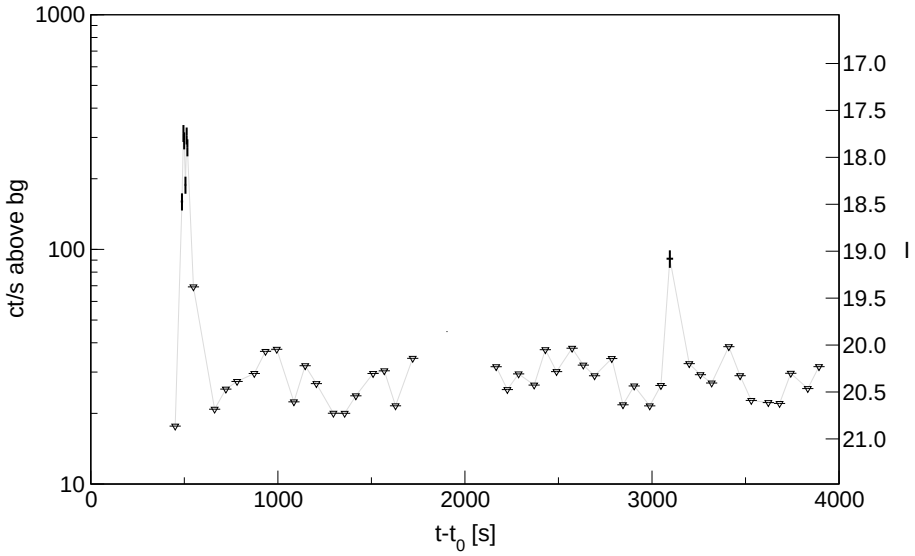

Figure 6.6.: Light-curve of the first night of observations of GRB 070610/J1955 (shown with adaptive bin size, 3-σ upper limits and 1-σ error-bars on detections). Two short, bright flares are observed. The canonical behaviour of a GRB afterglow would be a powerlaw decline.

the count-rates to magnitudes. However, this approach has several downsides, that are apparent stronger in OPTIMA than in standard CCD observations.

Time dependence In CCD based photometry, comparison sources in the same field of view are observed simultaneously to the source. The magnitude of these reference sources is compared to standard stars at photometric observing conditions. As OPTIMA can't observe source and reference star simultaneously, a change in observing conditions between these measurements can introduce systematic errors more easily.

Wavelength dependence Most CCD based photometry observations are performed using one of several standardized filter sets. Photometric standard stars are observed in the same filters as well, making observed magnitudes easily comparable. To maximize sensitivity, OPTIMA observations are performed in white light, i.e. without a filter. Due to colour differences between standard stars, reference stars and the source, this introduces a further source of systematic uncertainty.

In the case of J1955, the fact that a lot of observations by other groups occurred simultaneous to OPTIMA observations, helps alleviate the calibration difficulties often encountered in OPTIMA data.

One dataset with consistent quality and good overlap with the brightest flares recorded by OPTIMA is the dataset taken by the 80 cm telescope of the IAC[3]. For the IAC-80 CCD frames containing flares, the average OPTIMA count-rate during the CCD integration time was determined and compared to the photometry of J1955 in the CCD frames (see Fig. 6.9). This allows to derive as flux calibration $I = 19 \mathrel{\widehat{=}} 98$ ct/s, which is used throughout the J1955 section.[4]

[3]Instituto de Astrofísica de Canarias

[4] N.B. As the IAC-80 data was taken in the I-band, the calibration is not against R-band or V-band magnitudes as it is usually done for OPTIMA, and therefore differs considerably from the canonical

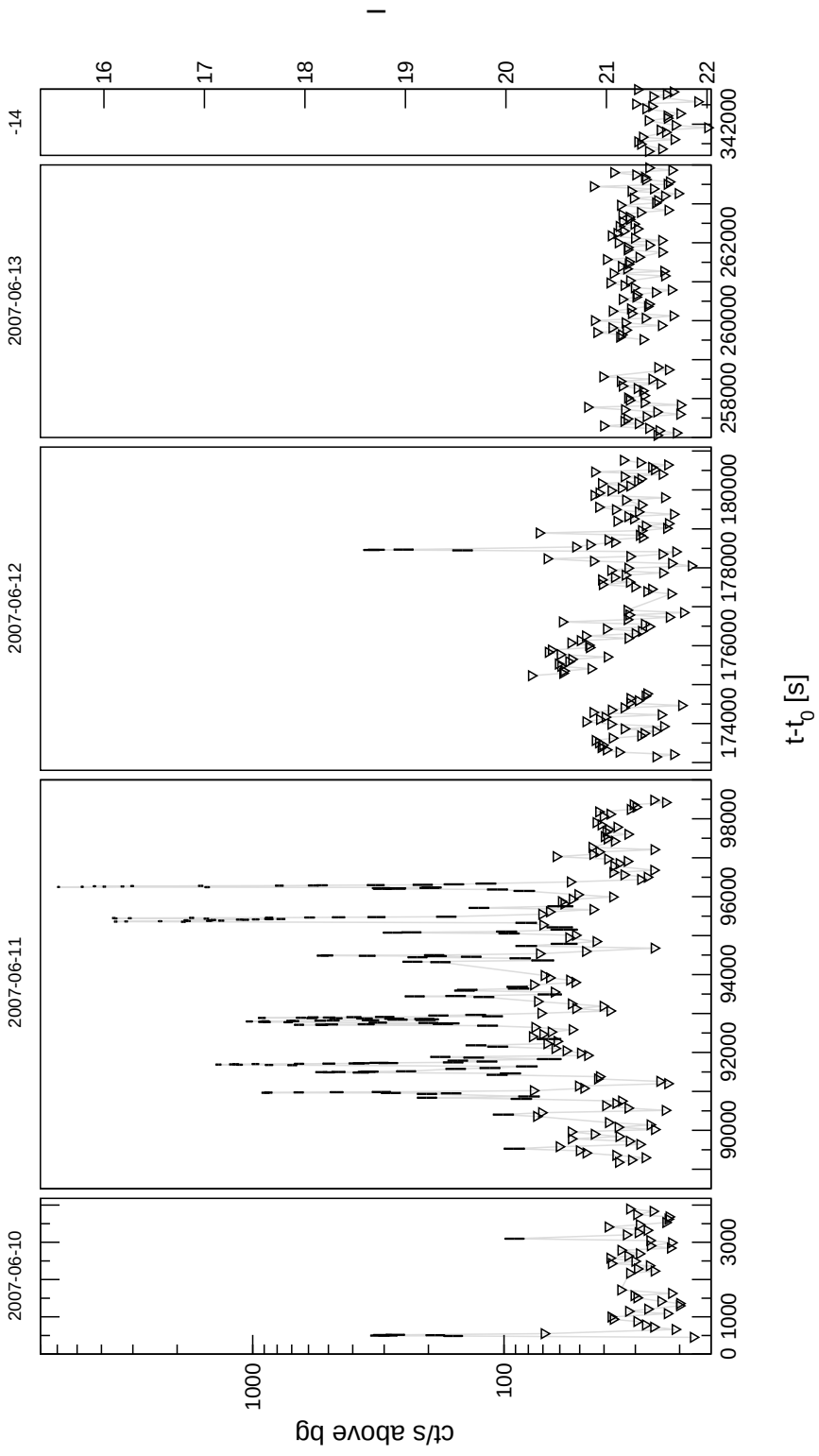

Figure 6.7.: Overview over OPTIMA-Burst high-time-resolution light-curves of J1955. The flaring activity in the second epoch shows a build-up culminating in two very strong flares, more than two orders of magnitude brighter than the upper limits between the flares.

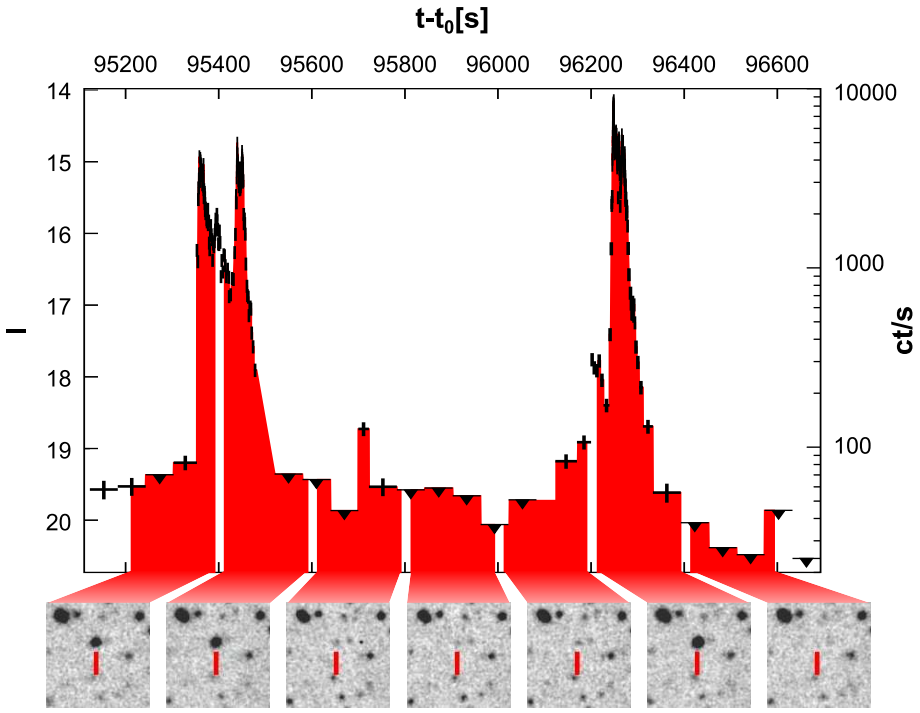

Figure 6.8.: OPTIMA light-curve of several flares of J1955, shown with simultaneous IAC-80 CCD exposures. Exposure intervals of the CCD frames are overplotted in red. In OPTIMA, the light-curve can be automatically binned corresponding to the source count-rate, allowing to resolve fine details in the variability, which remain unresolved in CCD photometry with fixed exposure times.

6.5. Analysis of Individual Flares

The signal to noise ratio in the flares seen in the light-curve of J1955 allows a detailed study of individual flares and sub-flares. Fig. 6.10 shows a detailed light-curve of the two brightest flares observed by OPTIMA-Burst. A distinct FRED structure of the flares is evident. To describe individual flares, a functional approach was chosen. The flares have been modeled as a sum of FRED-shaped sub-flares. For an individual FRED shaped flare, the count-rate R has been modeled as:

$$R = \begin{cases} R_0 \; e^{1/\tau_{\mathrm{rise}} \cdot (t-t_0)} & t < t_0 \\ R_0 \; e^{-1/\tau_{\mathrm{decay}} \cdot (t-t_0)} & t \geq t_0 \end{cases}$$

Appendix A contains a complete listing of all flares of J1955 fitted with sums of FRED functions. From these, especially from the two very bright flares shown also in Fig. 6.10, several interesting features become apparent.

Perhaps the most obvious feature of the light-curve is the extreme violence of the observed flares. The dynamic range between the noise-floor (20 mag) and the peak brightness (16.3 mag) in Fig. 6.10(b) is more than a factor of 200, with a rise-time of only a few seconds. Taking into account deeper optical and near infra-red limits, it could be as high as > 10000 (e.g. [Castro-Tirado et al., 2008] or [Kasliwal et al., 2008]).

OPTIMA value of $R = 19 \mathrel{\widehat{\approx}} 300$ ct/s

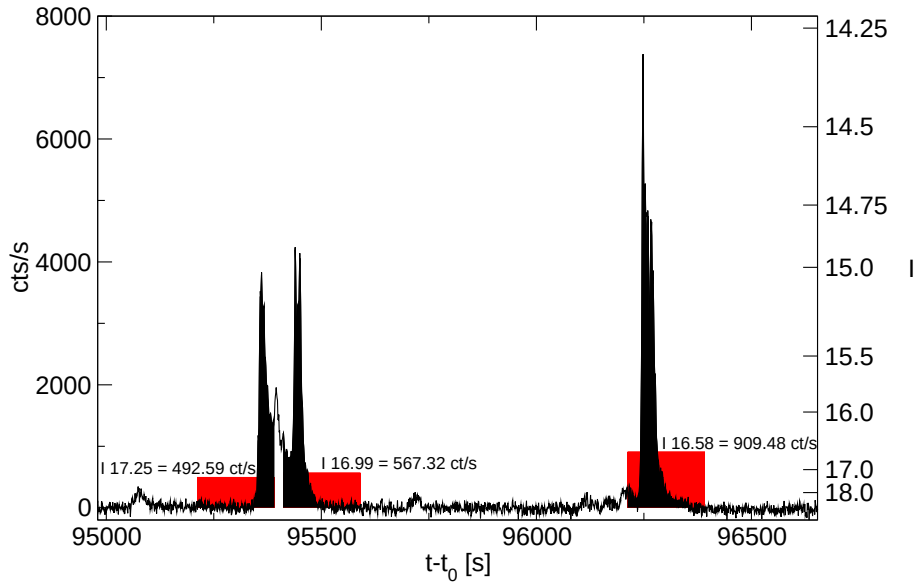

Figure 6.9.: Calibration of OPTIMA counts/s to IAC-80 I-band magnitude. The solid black shading under the light-curve denotes the exposure intervals of the IAC-80 CCD frames used for calibration. The red square underlying these intervals is the average OPTIMA count-rate during the interval.

Another intriguing feature is the timescale of the variability. Several sub-flares with rise-timescales below one second are resolved. Since the light-travel time across the emitting region is finite, variability faster than the light-crossing time $t = d/c$ would be washed out. The quickest variability observed in the flares as shown in Fig. 6.11 is $\approx 0.2 - 0.3$ s, corresponding to smaller than $\approx 10^{10}$ cm as size of the emitting region.

It is also interesting to note that the sub-flares in Fig. 6.10 do not appear to be uncorrelated. Instead, they tend to cluster in a sort of "rhythm" of $6 - 8$ s. This behaviour gives rise to features in the auto-correlation, and especially the power-spectral density.

6.6. Frequency-Domain Analysis

Besides analyzing the light-curves of flares individually, another mode of analysis is analyzing the statistical properties of the light-curves. As the individual flares are well resolved, they lend themselves to a statistical analysis of the timing properties of individual flares using a Fourier analysis.

For the two brightest flares (Fig. 6.10), the time span from 150 s before the peak of the flare to 150 s after the flare was binned to a constant 0.5 ms resolution. Using the *powspec* task of the *Xronos* timing analysis software package[5], the PSD was calculated. The PSD is a periodogram in which the power (i.e. amplitude squared) of variability is plotted against the time-scale of the variability.

The PSD shows a number of interesting properties. The first interesting property is that above a frequency of a few Hertz, the PSD does not contain any features rising significantly above the r.m.s. noise floor. This confirms the finding from the analysis of the individual sub-flares in section 6.5 that the fastest variability time-scale is ~ 0.3 s

[5] `http://heasarc.gsfc.nasa.gov/docs/xanadu/xronos`

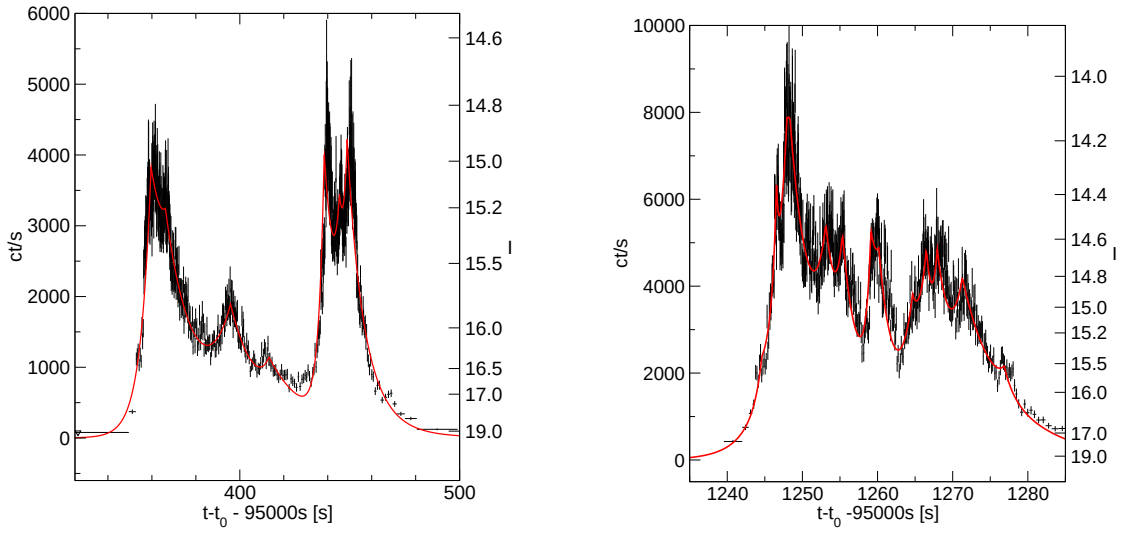

(a) (b)

Figure 6.10.: Detailed light-curve of the two brightest flares shown in the inset of Fig. 6.7. The red lines denote a simple model consisting of several FRED curves to describe the light-curve. The light-curves were binned using adaptive binning.

The most obvious feature also confirms a finding from section 6.5: the "rhythmic" arrival of sub-flares gives rise to a strong feature in the PSD at the rhythm's period. This feature is similar to a quasi-periodic oscillation (often observed in the X-rays), and can be well fit by a Lorentzian. When fitting the PSDs displayed in Fig. 6.12 with a low-frequency Lorentzian to account for the red noise, one Lorentzian for the peak and a constant for the white noise, the Lorentzians of Fig. 6.12(a) and Fig. 6.12(b) overlap within their respective FWHMs and errors, as can be seen from the parameters in table 6.2. In addition to the strong features in the PSDs at around 0.14 Hz, the harmonics of these features can be identified as slight excess over the fitted functions. However, as can be seen from the residuals, the excesses are not statistically significant. Therefore, the harmonics were not included in the fit.

Figure	f_0	FWHM	χ^2/d.o.f.
Fig. 6.12(a)	0.163 ± 0.007 Hz	0.020 ± 0.009 Hz	0.88
Fig. 6.12(b)	0.127 ± 0.006 Hz	0.015 ± 0.007 Hz	0.98

Table 6.2.: Fit parameters for the peaks in Fig. 6.12

Taken by themselves, the $6 - 8$ s features of Fig. 6.12(a) and Fig. 6.12(b) are statistically not extremely significant. This is mainly due to the short durations of the flares, which resulted in a low number of sub-flare beats that contributed to the features. Considering that these features arise in two disjunct time-spans independently, and are not seen as system-frequencies in observations taken before and after the observation of J1955, they very probably arise from the source.

Although it suffers from the same problem of limited flare length / beat number, the X-ray flare shown in Fig. 6.3(b) has a sufficient photon count-rate in the XRT light-curve to search for periodicity on the same time-scales. As was first reported by [Kasliwal et al., 2008],

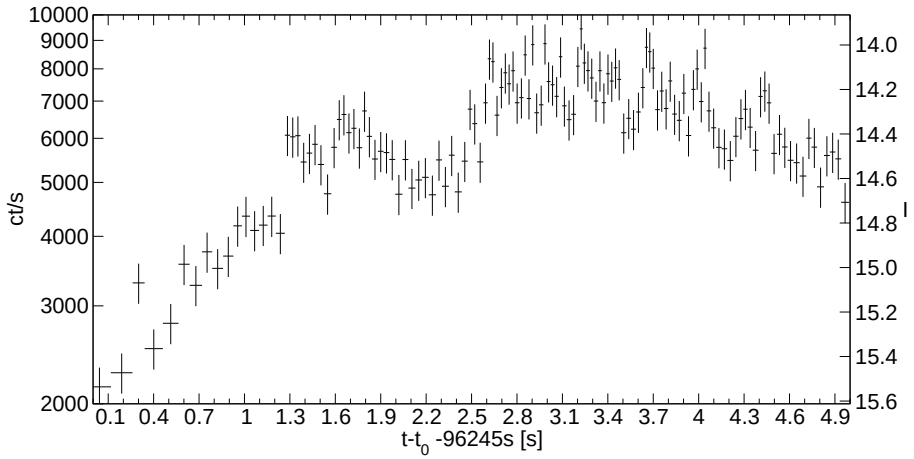

Figure 6.11.: High time-resolution detail of the brightest flare observed in J1955. Using the adaptive binning technique described in Chapter 4.1, a maximum of detail can be extracted from the light-curve. Sub-flares with rise-times down to $0.2 - 0.3$ s are well resolved, indicating a size of the emitting region of $< 10^{10}$ cm

there is a hint of periodicity at a frequency of 0.1446 Hz . The significance of this periodicity is very low: while [Kasliwal et al., 2008] give a significance of $3.4\,\sigma$, the actual significance could be as low as $\sim 1\,\sigma$, depending on the statistical test employed. Taken on its own, this result probably could not be taken as evidence of periodicity. However, the frequency of 0.1446 Hz (shown as a red line in Fig. 6.12) coincides exactly with the features in Fig. 6.12.

The X-ray flare was observed at $\sim 7.86 \cdot 10^4$ s after the initial trigger, whereas the flares shown in Fig. 6.10 were observed at $\sim 9.54 \cdot 10^4$ s and $\sim 9.63 \cdot 10^4$ s. The fact of coincident features at completely different epochs and energy regimes strongly favours an interpretation of these features as physical features, as opposed to systematic effects. Moreover, it is likely that these features do not stem from effects limited to the individual outbursts observed, but are indeed linked to the underlying properties of the astrophysical object giving rise to the outbursts.

6.7. Statistical Analysis

As the total number of recognizable flares and sub-flares is quite large, it is worthwhile to analyze the distribution of flares. Flares most often are not resolved individually in CCD-based astronomy, therefore the widely used approach to generate brightness histograms does not directly plot the distribution of flare peak brightness, but rather a distribution of brightness samples. The sampling is defined by the exposure times and time between exposures and can, for this purpose, be seen as random sampling. To make the analysis compatible with the exposure-time based approach, Fig. 6.13 shows a histogram of the brightness of 10 s-bins.

The distribution can be reasonably well fit ($\chi^2/\text{d.o.f.} = 1.25$) by a zero-mean log-normal distribution

$$f(x,\sigma) = \frac{1}{x\sigma\sqrt{2\pi}}\, e^{-\frac{(\ln x)^2}{2\sigma^2}}$$

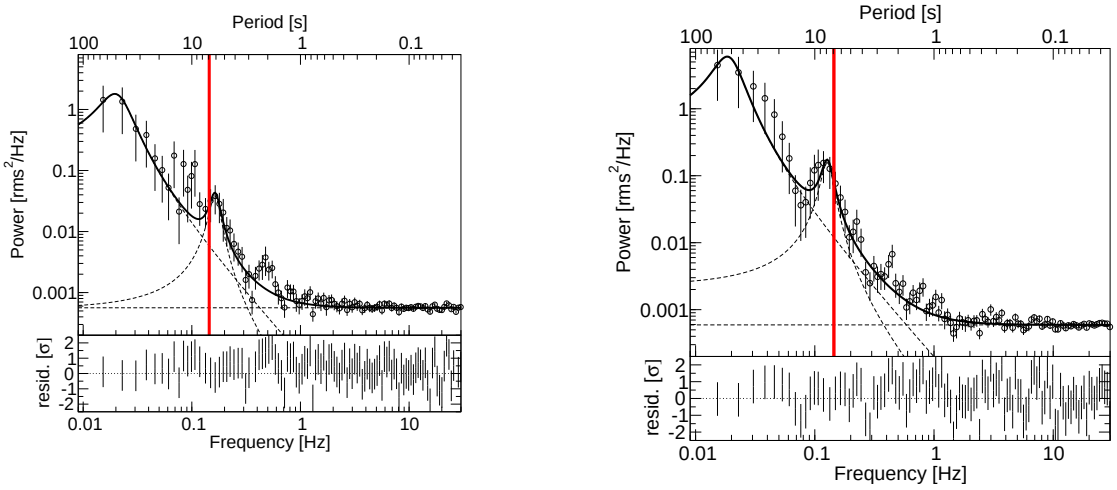

(a) (b)

Figure 6.12.: Power spectral density (PSD) plots of the flares shown in Fig. 6.10. Both PSDs show a similar feature at a period of around $6 - 8$ s. Within their respective FWHMs, both features overlap. Also overlapping (shown in red in both plots) is a marginal $(1 - 3\ \sigma)$ detection of a possible X-ray periodicity, first reported in [Kasliwal et al., 2008].

Log-normal distributions (i.e. the variable's logarithm is normally distributed) can be used to model processes that can be though of as a product of many independent (positive) factors close to 1. Besides the classical examples of stock investment return rates and insurance risk assessment, physical examples include the magnitude of earthquakes or the intensity of Solar flares.

6.8. Astrophysical Interpretation

The answer to the question of what type of object J1955 actually *is*, is not obvious. The easiest way to begin answering this question is by asking the reciprocal question: what is J1955 *not*?

6.8.1. Excluding Several Scenarios

The first possibility that springs to mind is that J1955 is a γ-ray Burst. It was initially detected as GRB trigger by the *Swift* BAT instrument. However, both the X-ray as well as the optical afterglow light-curves are highly unusual for a GRB. The overall light-curve of GRB afterglows usually follows a power-law decline, often with one or more breaks in the decay index (see e.g. [Meszáros, 2007] for a review). In many bursts, re-brightening episodes and flares occur superimposed on top of the power-law decay. One key feature that all non-powerlaw-decay features show is that since the shock wave giving rise to the afterglow is expanding, the variability timescale of the features tends to scale with the time since initial trigger (i.e. $\Delta t/t \approx 1$). For the bright X-ray flare observed by the XRT and the optical flares observed by OPTIMA this is much lower: $\Delta t/t \approx 10^{-4}$. If one considers individual sub-flares, this becomes $\Delta t/t \approx 10^{-5}$. This speaks strongly against

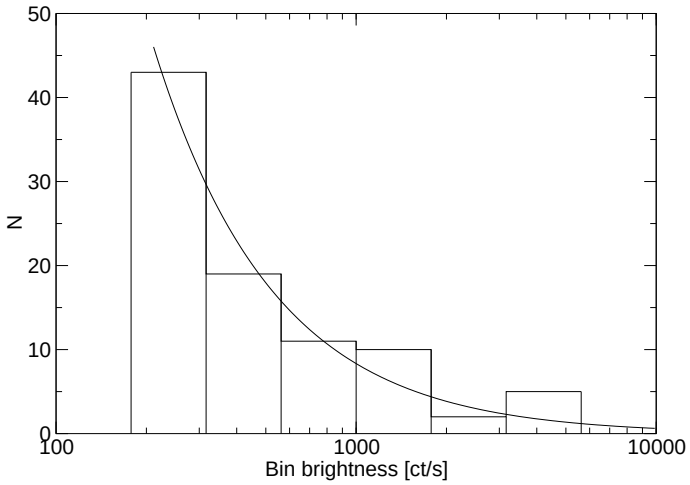

Figure 6.13.: Histogram of flare brightness. Histogram bars are brightness of individual 10 s-bins, for all bins brighter than 5 σ above the background level. The black curve is a log-normal distribution fit to the data.

a GRB origin of J1955. Taken with the position in the Galactic plane, and the X-ray extinction column slightly below the expected Galactic value, J1955 is most probably of Galactic origin. Of course, this does not exclude the possibility that the initial γ-ray burst observed by BAT (GRB 070610) was indeed a GRB, and J1955 is only a chance coincidence with GRB 070610. However, as the discussion in this work is only concerned with J1955 and not GRB 070610, this scenario is of little consequence.

Secondly, two groups have proposed that J1955 and the black hole candidate V4641 Sgr are of similar nature [Kasliwal et al., 2008] [Markwardt et al., 2007]. V4641 Sgr is thought to be a black hole orbiting an intermediate mass companion star, a B9 subgiant, and was suggested as the first member of a new class of objects, the so-called "fast X-ray novae" [Uemura et al., 2002]. However, several lines of evidence speak against this connection. Firstly, the properties of the optical variability of V4641 Sgr are quite different from J1955. V4641 Sgr shows flares of < 1 mag and > 50 s length ([Uemura et al., 2004] [Uemura et al., 2005]), whereas J1955 shows much more extreme variability. As the shortest exposure times used for the observations reported in the literature are 30 s, the more subdued nature of variability in V4641 Sgr is not an observational artefact.

In addition to the incompatible variability behaviour of J1955, the observed multi-wavelength behaviour of J1955 is unexpected if it were the same kind of object as V4641 Sgr. During the outburst phase a few days after the initial trigger, a total lack of γ-ray, mm and cm emission implies a different emission mechanism than the collimated jet assumed in V4641 Sgr [Castro-Tirado et al., 2008].

6.8.2. The J1955 −SGR 1900+14 Connection

The very fast variability with time-scales as short as ≈ 0.3 s implies a very small (10^{10} cm) emitting region. Assuming a distance d and an optical extinction $A_V = 5$, the extinction-corrected I-band isotropic peak luminosity of the flares is $1.0 \cdot 10^{35}\ (d/5\ \mathrm{kpc})^2\,\mathrm{erg\,s^{-1}}$, for the flare shown in Fig. 6.10(a), and $1.8 \cdot 10^{35}\ (d/5\ \mathrm{kpc})^2\,\mathrm{erg\,s^{-1}}$ for the flare shown in Fig. 6.10(b). For a region of 10^{10} cm diameter to produce this luminosity as thermal

radiation, the surface temperature would have to be several 10^7 K. While this is not uncommon, it is not easily seen how a region this size could heat up to such a high temperature in just 4 s, the time it took for the flare to rise from below OPTIMA detection threshold to peak flux. The extreme variability therefore indicates a non-thermal radiation process as most probable source of the observed flares.

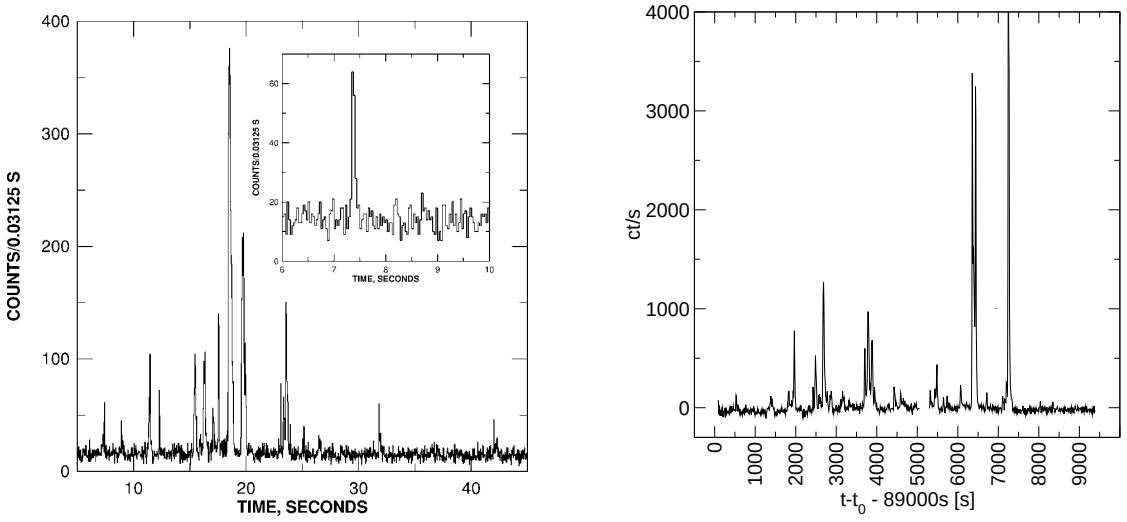

(a) (b)

Figure 6.14.: The optical light-curve of J1955 shows outbursts similar to those observed in Soft γ-ray Repeaters (SGRs) and Anomalous X-ray Pulsars (AXPs) in the high energy regime.
Panel (a) shows a portion of the $25 - 150$ keV light-curve of the May 30 1998 outburst of SGR 1900+14 [Hurley et al., 1999].
Panel (b) shows a cutout of the optical light-curve of J1955. While the time-scales involved are longer, the overall structure of the light-curve is similar.

One interesting non-thermal scenario is suggested by the overall morphology of the optical light-curves. Fig. 6.14 shows a high-energy light-curve of a period of outburst of SGR 1900+14 next to a cut-out of the optical light-curve of J1955 on the second night. It is quite intriguing that both light-curves show a very similar overall morphology, despite their respective energy ranges being separated by more than 4 orders of magnitude. Both light-curves show bursts of flaring activity, with the individual flares consisting of short, sharp spikes of FRED shape. Both light-curves show a marked gradual increase of flaring activity followed with a sharp drop of activity. The most striking *difference* between the two light-curves is the time-scales involved. In J1955, everything appears to happen about two orders of magnitude slower than in SGR 1900+14.

6.8.3. Magnetars

SGR 1900+14 is a SGR[6], a type of source initially detected as GRBs with, like the name implies, a very soft spectrum, and showing repeated activity from the same spot in the sky

[6]Soft γ-ray Repeater

(see e.g. [Kouveliotou, 2003] for a review). SGRs, as well as AXPs[7] have been explained by the *magnetar* model [Duncan and Thompson, 1996].[8]

Magnetars are slowly rotating ($P \sim 5 - 10$ s) neutron stars with an extremely high magnetic field ($B \sim 10^{14} - 10^{15}$ G). Like pulsars, they are formed in a core-collapse supernova. As the core of the progenitor star collapses by a factor of 10^5 during the supernova, the magnetic field of the progenitor is amplified by a factor of 10^{10} . In addition, the field is amplified by a dynamo effect powered by convection. These two effects together give rise to the usual strong magnetic fields of pulsars of order 10^{12} G. If the spin period of the newly formed neutron star is comparable to the convection time-scale (~ 10 ms), the dynamo effect starts to operate globally instead of only locally. This can transfer about 10% of the kinetic energy of the convecting fluid into the magnetic field, boosting the field strength by a factor 1000 to 10^{15} G. Since the field is so strong, the spin-down rate is very large as well, braking the very fast rotation of the young magnetar withing 5000 years down to $P \sim 5 - 10$ s.

The extreme magnetic field strength of a magnetar gives rise to a lot of unusual effects. Photons begin to show more particle-like behaviour, and can split into two photons (or vice versa). The vacuum becomes birefringent, as the propagation speed of an electromagnetic wave becomes dependent on the polarization angle relative to the field vector of the magnetar's field. Scattering processes of a photon on an electron become more complicated, as the electron's movement is confined to one degree of freedom along the field lines, which can suppress scattering. The same effect also pulls electron orbitals of atoms into a long, thin needle shape.

Magnetars are observed as two types of astronomical objects: Anomalous X-ray Pulsars and Soft γ-ray Repeaters. AXPs are X-ray pulsars with a luminosity higher than can be powered by rotational energy. Unlike in normal pulsars, the emission in AXPs is powered by the decay of the extremely strong magnetic field. In SGRs, the magnetic field exerts strong stresses on the crust of the neutron star. The stress on the crust builds up, until at some point the crust breaks, giving rise to a soft γ-ray flare. As the magnetar rotates, the field line configuration changes, putting more and more energy into the field. On rare occasions, the whole field reconfigures releasing this energy in a giant flare that can have a luminosity as high as $\sim 10^{47}$ erg/s (e.g. [Hurley et al., 2005]). After an active life-time of only $\sim 10^4$ years, the magnetic field reaches a final, stable configuration. As the emission processes in SGRs and AXPs are powered by the decay of the magnetic field, at this point AXPs and SGRs cease to be observable.

6.8.4. Is J1955 a Magnetar?

To determine beyond doubt that a source is a magnetar, the magnetic field has to be determined. Usually, this is done by measuring the spin-down rate and determining the magnetic field assuming magnetic braking. In the case of J1955, this is not possible, as the detection of a possible period in the optical and in the X-rays is much too imprecise to allow the deduction of a period derivative. Nevertheless, the hypothesis of J1955 being a magnetar flaring in the optical is consistent with observation.

Besides the overall morphology, the biggest indication comes from the tentative period of $P = 6 - 8$ s. The same period is apparent both in the optical as well as in the X-rays at unrelated observational epochs, speaking against the period being a feature of the flares

[7] Anomalous X-ray Pulsars

[8] There are competing models, explaining AXPs with accretion from a fallback disk [Trümper et al., 2010]

themselves, but rather from the underlying object. The observed period is exactly in the regime of typical magnetar periods.

If this is interpreted as the rotational period of a magnetar, the magnetar's light-cylinder[9] is at $3 \cdot 10^{10}$ cm. This is compatible with the assumption of magnetospheric emission, and locates the emission region of 10^{10} cm in the outer magnetosphere.

The log-normal flare flux distribution is compatible with a magnetar hypothesis as well. Besides the already mentioned examples that typically show log-normal magnitude distributions (earthquakes and solar flares), also SGR flare fluxes follow log-normal distributions (e.g. [Hurley et al., 1994])

The multi-wavelength behaviour of J1955 also is compatible with a magnetar scenario [Castro-Tirado et al., 2008]. However, the X-ray luminosity and flare activity is lower than expected from a SGR scenario. This leads one group [Castro-Tirado et al., 2008] to suggest J1955 is a border-case between a normal, active magnetar, and an older, non-active DINs[10].

Although one SGR (SGR 1806-20, see [Kosugi et al., 2005]) and several AXPs have nIR or optical counterparts, so far no magnetar has ever been observed to flare in the optical like it does in the high-energy regime. Therefore, the bulk of theoretical work on magnetars has focused on the high-energy regime, and not many models can explain the emission processes leading to optical flares from a magnetar. One possible scenario is ion cyclotron emission from radii of $\sim 20 R_{\rm NS}$, where the ion cyclotron frequency in the magnetic field of the magnetar lies in the optical band [Beloborodov and Thompson, 2007]. This mechanism requires a sufficient number of ions in the corona of the magnetar. The number of ions in the corona is sensitive to the ratio of the voltage along the magnetic field lines, and the ion gravitational energy. The ions will act as a filter for the radio and microwave radiation that is emitted by coherent processes near the neutron star. The radiation reaching $r \gtrsim 5 \cdot 10^7$ cm will be partially absorbed by the ions at their cyclotron resonance, pumping their perpendicular energy $E_\perp$. This energy further increases as the ions approach the star, since $E_\perp / B$ is an adiabatic invariant. Most of their energy escapes once their cyclotron cooling and transit times become comparable at a height of roughly $\sim 2 \cdot 10^7$ cm. At this height, the ions emit cyclotron radiation in the optical-IR range.

While this mechanism can in principle explain flaring in the optical, it does have its problems in the context of J1955. Most notably, the region in which the ions emit the cyclotron radiation in the optical is smaller than the emission region as deduced by the optical variability. Of course, it is possible that the variability is intrinsically slower than the light-crossing time across the emitting region.

[9] The light-cylinder is the surface at which the radial velocity of a co-rotating frame reaches the speed of light

[10] Dim Isolated Neutron Stars

7. Conclusions

7.1. OPTIMA-Burst Retrospection

The stated goal of the present work as outlined in the introduction was to develop an instrument capable of performing optical HTRA studies of high-energy transients, a field that shows a great potential for unexpected discoveries but which has seen very little work so far. To this end, the pre-existing configuration of the OPTIMA instrument was upgraded with a polarimeter (Chapter 2.2.3), new data-acquisition electronics (Chapter 2.5.2), and a control-system closely tied into the telescope control system of the Skinakas 1.3 m telescope (SKO), and the GCN trigger network (Chapter 3) to form the novel OPTIMA-Burst system.

For the scope of this work, OPTIMA-Burst was applied in a total of 313 nights at SKO, receiving and reacting to numerous triggers. Two note-worthy events were observed, GRB 090726 (Chapter 5.2.2), and the galactic X-ray transient J1955 (Chapter 6). GRB 090726 was a long GRB with a broken power-law afterglow light-curve. Using OPTIMA-Burst, it was possible to show that the power-law decay of the optical light-curve had no excess variability, disproving some interpretation in the literature.

J1955 was at first thought to be a GRB, but this interpretation could be quickly ruled out using OPTIMA-Burst data. The source showed highly unusual behaviour, with unprecedented extremely bright and fast variability and a tentative hint of periodicity. While it is possible that J1955 would have been marked as unusual without the HTRA observations of OPTIMA-Burst, it is highly unlikely that the unprecedented nature of the source would have been discovered, as currently no competing instrument with quick reaction time to high-energy triggers can adjust the detector integration time *after* the observation. The very high dynamic range and steep rise-times of the flares of this source result in isolated bright frames in conventional systems, but can be adaptively resolved with optimal SNR in OPTIMA data. The true nature of J1955 could not be determined with OPTIMA-Burst with any finality, but the data has led to the speculation that the source may be a magnetar flaring in the optical. The observations of this source and this interpretation of the data have been published independently from this work in a well-received paper [Stefanescu et al., 2008b].

Although no optical/X-ray correlation studies could be performed since no overlap with high-energy observations by *Swift* and RXTE could be achieved, the OPTIMA-Burst project can be considered a success. The very surprising results of J1955 show that indeed, there is great potential in the observation of high-energy transients with high time resolution in the optical. Also, it is clear that the observing strategy employed by OPTIMA-Burst, long-duration campaigns with interrupt-rights for targets of opportunity at relatively small and cheap observatories, is feasible.

7.2. The Way Forward

In the more than 300 nights of operation, several lessons for this type of instrument have been learned. Good background and transparency control is critical to interpretation of data from any aperture photometer. The addition of a moveable fibre for simultaneous observation of a comparison star in the field would help achieve quantitative photometric results at much higher accuracy than now routinely possible, as intrinsic variation in the source flux could then be disentangled from transparency fluctuations and scintillation in a straightforward fashion. Such positioning mechanisms have previously been developed for high-resolution multi-object spectrographs, but are quite complex systems, limiting their use in flexible guest instruments like OPTIMA.

Another possibility to achieve simultaneous comparison star observations at high time-resolution is to use high-speed imaging detectors. Such a detector could be installed relatively easily instead of the field-view CCD camera of OPTIMA, but in this configuration the target and the comparison star would not be observed using the same type of detector, complicating data interpretation.

Alternatively, a new-generation HTRA system could employ high-speed imaging detectors instead of fibre-fed APDs. For a transient-observing instrument, this has the great advantage that the target need not be correctly identified and positioned onto a predefined aperture *before* usable science data can be taken.

On the other hand, as it has become evident in the OPTIMA-Burst project that the independence from conventional exposure-times can be of critical importance for the success of an observation, this would necessitate the high-speed imager to operate at much faster frame-rates than the fastest expected variability time-scales. As each read-out process also adds a noise component, very high frame-rates imply high read noise levels, limiting the achievable sensitivity.

Several detector concepts have been developed to surmount this problem. The technique currently most widely used employs the emCCD[1], a CCD with an embedded stochastical electron multiplication step similar to an APD. The charge multiplication results in a macroscopic signal even for individual electrons signal charge, thereby reducing the effective read-noise to zero. However, due to the stochastical nature of the multiplication step, an excess noise at higher signal levels is introduced, which limits the useful dynamic range. In practice, while the emCCD can detect individual photons, it cannot distinguish 101 photons from 100. Therefore, an emCCD-based detector is best operated at frame-rates high enough to make the probability of two photons hitting the same pixel negligible. See Chapter 4.3 for a discussion of a related effect in OPTIMA.

Another very promising detector development is the DEPFET[2] active pixel matrix. In an active pixel matrix, each individual pixel of an imaging detector contains its own first-stage amplifier. The DEPFET implementation of an active pixel sensor extends this principle by making the first stage transistor act as detector itself, greatly reducing the read-out noise in the process. As the signal charge in a DEPFET can be read out non-destructively, detectors can be built in which the signal charge of each individual pixel is read out repeatedly. Thereby, the read-out noise can be reduced to levels so low that individual signal electrons can be detected. In contrast to the emCCD technology, this does not make use of a stochastic charge multiplication process with its aforementioned downsides. The RNDR[3] DEPFET therefore has a very high dynamic range – it indeed

[1] electron multiplying CCD
[2] Depleted P-channel Field-effect Transistor
[3] Repeated Non-Destructive Read-out

can distinguish 101 from 100 photons, making it a very interesting detector for the next generation of optical HTRA systems.

Another lesson learned during the OPTIMA-Burst campaigns was that even with *Swift* as a dedicated high energy transient "trigger machine", suitable triggers for prompt ground-based follow-up observation remain quite rare events. In almost one cumulated year of OPTIMA-Burst observation, only two events were of prime scientific interest. This is aggravated by the fact that *Swift* will not be operational indefinitely, and most missions currently orbiting or planned will not be able to provide the triggers in the same numbers and with the same localization accuracy as *Swift*.

With the advent of new classes of massively parallel observatories like SKA[4] and its predecessor LOFAR[5] in the radio, and survey telescope projects like LSST[6] and its predecessors PanSTARRS[7] and VISTA[8] in the optical, new "transient factories" are already in advanced planning stages or already commissioned, that will scan the complete sky accessible to their location for transients. While the type of object that triggers these observatories will likely not be the same as for the X-ray observatories, a new exciting wealth of transient triggers can be expected from these novel facilities. Dedicated automated HTRA instruments waiting in interrupt-mode at moderate-sized telescopes will be a great complement to the great observatories of the next fifteen years.

[4]Square Kilometre Array
[5]Low Frequency Array
[6]Large Synoptic Survey Telescope
[7]Panoramic Survey Telescope and Rapid Response System
[8]Visible and Infrared Survey Telescope for Astronomy

A. Table of Individually Fitted Flares of SWIFT J195509.6+261406

The light-curve of J1955 taken by OPTIMA shows numerous bright flares. Most of these flares are of fast-rise, exponential-decay (FRED) form, in some cases consisting of many smaller overlapping flares. The individual flares are modeled as:

$$R = \begin{cases} R_0 \; e^{1/\tau_{\mathrm{rise}} \cdot (t-t_0)} & t < t_0 \\ R_0 \; e^{-1/\tau_{\mathrm{decay}} \cdot (t-t_0)} & t \geq t_0 \end{cases}$$

Each flare reaching more than 3σ excess above quiescent background emission in the 10 s binned light-curve was inspected by eye, setting initial conditions for a Levenberg-Marquardt fit using octave. The results of these fits follow.

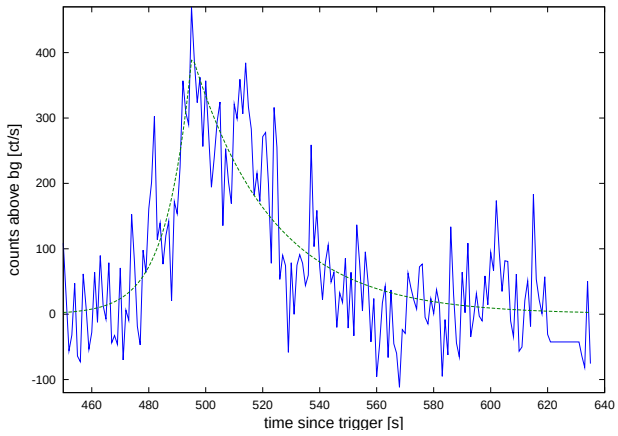

t_0[s]	R_0 [ct/s]	τ_{rise} [s]	τ_{decay} [s]
495.18 ± 0.96	396 ± 24	8.9 ± 1.5	28 ± 2.7

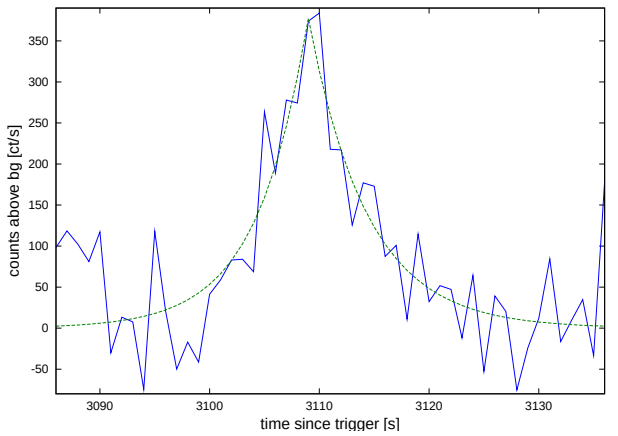

t_0[s]	R_0 [ct/s]	τ_{rise} [s]	τ_{decay} [s]
3109 ± 1.1	379 ± 36	4.6 ± 1.3	5.4 ± 1.4

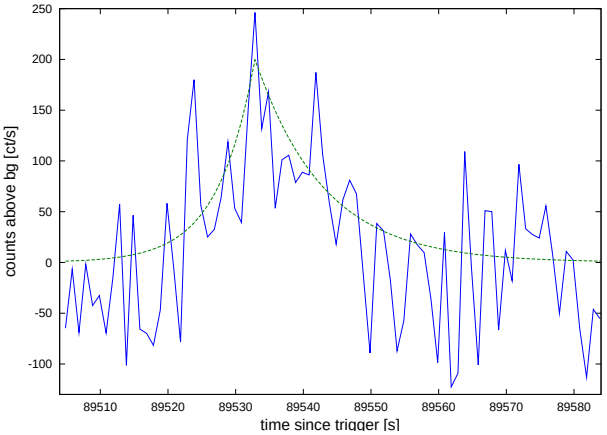

t_0[s]	R_0 [ct/s]	$\tau_{\rm rise}$ [s]	$\tau_{\rm decay}$ [s]
89532.9 ± 1.3	200 ± 31	5.5 ± 2.1	10.1 ± 2.8

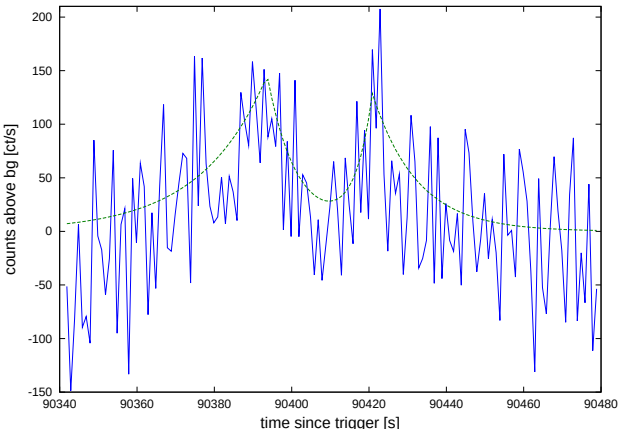

t_0[s]	R_0 [ct/s]	$\tau_{\rm rise}$ [s]	$\tau_{\rm decay}$ [s]
90393.7 ± 2.5	145 ± 25	17.2 ± 5.2	7.6 ± 5.1
90420.9 ± 2.5	125 ± 30	4.5 ± 4.4	11.7 ± 5

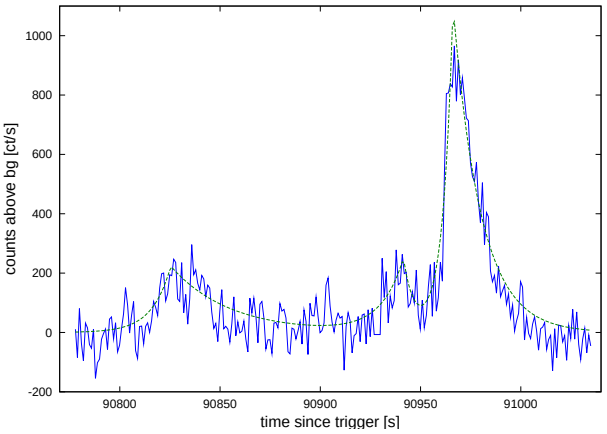

t_0[s]	R_0 [ct/s]	$\tau_{\rm rise}$ [s]	$\tau_{\rm decay}$ [s]
90825.5 ± 2.1	223 ± 24	9.5 ± 3.1	29.1 ± 5.7
90941.5 ± 1.8	240 ± 36	11.5 ± 3.4	5.1 ± 3
90966.2 ± 0.4	1097 ± 34	5 ± 0.66	13.79 ± 0.75

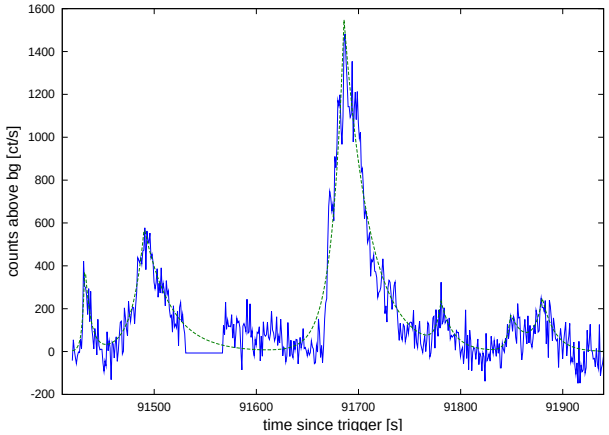

t_0[s]	R_0 [ct/s]	$\tau_{\rm rise}$ [s]	$\tau_{\rm decay}$ [s]
91432.1 ± 1.6	409 ± 65	2.4 ± 1.5	5.7 ± 2.1
91490.2 ± 1.1	578 ± 30	11.6 ± 1.7	25.9 ± 2.3
91685.9 ± 0.42	1548 ± 30	11.74 ± 0.61	25.3 ± 0.92
91780.8 ± 2.9	200 ± 45	5.2 ± 3.7	11.1 ± 4.9
91849 ± 4.3	167 ± 49	4 ± 4.1	14 ± 23
91880 ± 3.1	232 ± 59	8 ± 9.7	12 ± 4.5

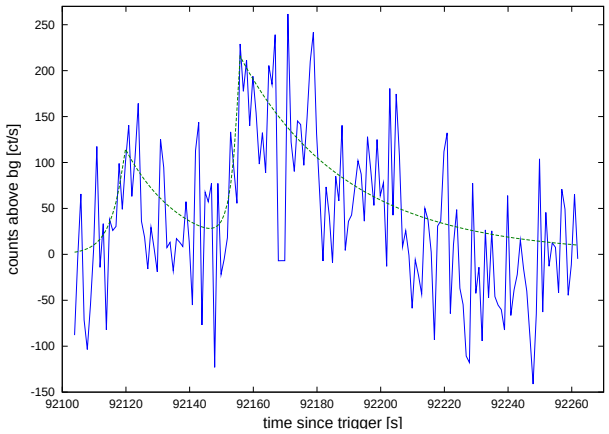

t_0[s]	R_0 [ct/s]	$\tau_{\rm rise}$ [s]	$\tau_{\rm decay}$ [s]
92119.7 ± 4.2	115 ± 32	4.1 ± 4.4	17 ± 11
92155.7 ± 2.1	202 ± 27	2.2 ± 2.1	35.4 ± 6.3

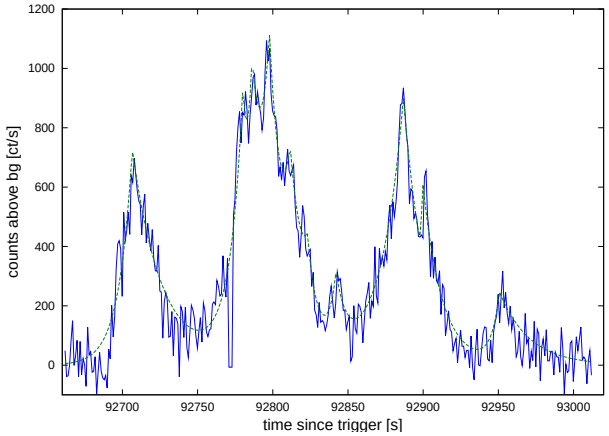

t_0[s]	R_0 [ct/s]	$\tau_{\rm rise}$ [s]	$\tau_{\rm decay}$ [s]
92706.6 ± 0.92	727 ± 33	9 ± 1.1	19.8 ± 2.4
92780.1 ± 1.8	700 ± 580	10 ± 4.6	5 ± 11
92786.2 ± 4.3	600 ± 1100	4.2 ± 9.4	14 ± 68
92797.8 ± 4	700 ± 1200	7 ± 19	8 ± 19
92811.6 ± 6	460 ± 740	8 ± 24	10 ± 35
92823.1 ± 9	200 ± 420	6 ± 25	5 ± 19
92842.1 ± 4.8	230 ± 130	4.6 ± 9.4	6.7 ± 8
92886.9 ± 1.4	899 ± 43	15.2 ± 2.6	14.4 ± 4.9
92899.3 ± 2.1	257 ± 66	0.51 ± 0.5	11 ± 10
92950.8 ± 2.8	234 ± 34	5.4 ± 3.3	20.2 ± 5.3

A. Table of Individually Fitted Flares of SWIFT J195509.6+261406

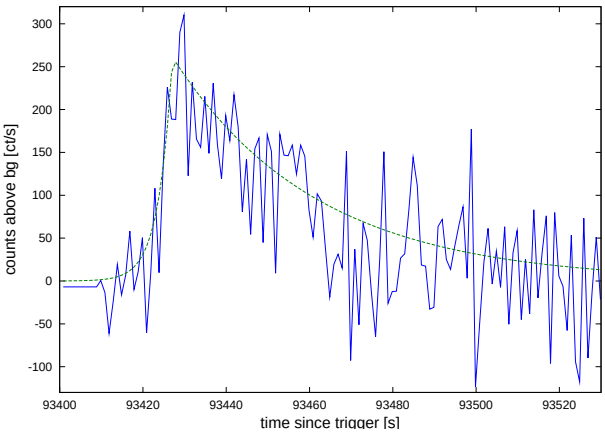

t_0[s]	R_0 [ct/s]	$\tau_{\rm rise}$ [s]	$\tau_{\rm decay}$ [s]
93427.1 ± 1.8	261 ± 20	3.3 ± 1.7	34.4 ± 4.6

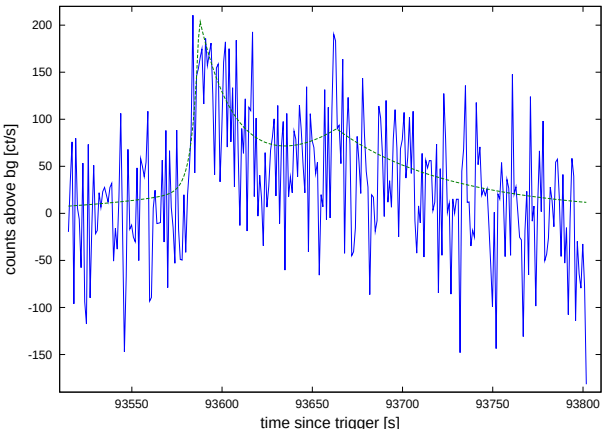

t_0[s]	R_0 [ct/s]	$\tau_{\rm rise}$ [s]	$\tau_{\rm decay}$ [s]
93587.3 ± 3	183 ± 27	3.6 ± 2.8	20.3 ± 7.4
93663 ± 10	86 ± 14	62 ± 23	69 ± 18

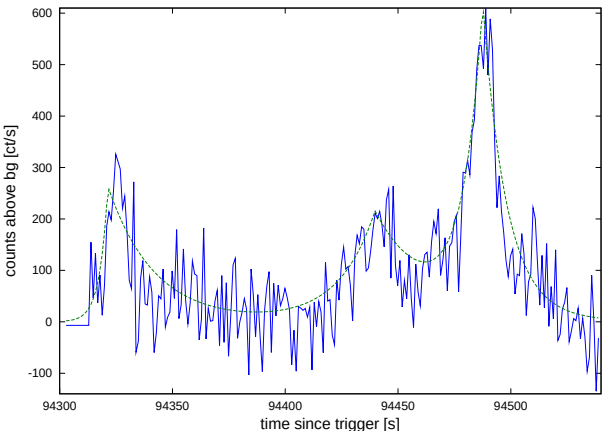

t_0[s]	R_0 [ct/s]	$\tau_{\rm rise}$ [s]	$\tau_{\rm decay}$ [s]
94321.4 ± 2.5	263 ± 28	3.7 ± 2.1	20.5 ± 4.4
94439.8 ± 3.7	212 ± 24	16.3 ± 4.6	24 ± 13
94487.5 ± 1.3	591 ± 34	8.7 ± 2.2	10.3 ± 1.6

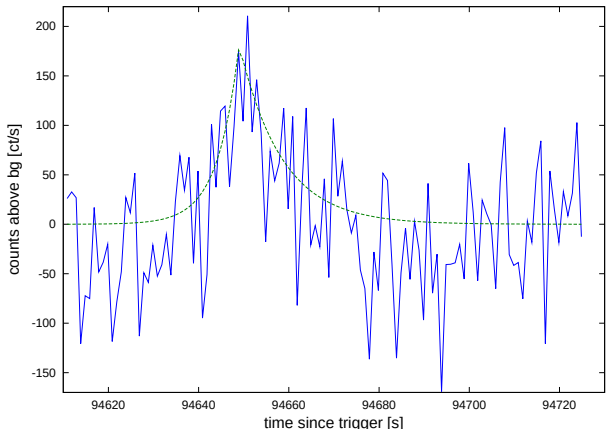

t_0[s]	R_0 [ct/s]	$\tau_{\rm rise}$ [s]	$\tau_{\rm decay}$ [s]
94649 ± 4	182 ± 31	4.8 ± 3.3	9.4 ± 4.3

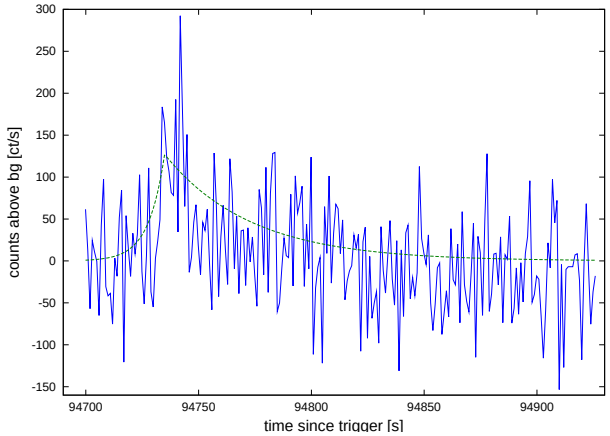

t_0[s]	R_0 [ct/s]	$\tau_{\rm rise}$ [s]	$\tau_{\rm decay}$ [s]
94734.9 ± 4.5	127 ± 19	7.1 ± 4.9	38 ± 11

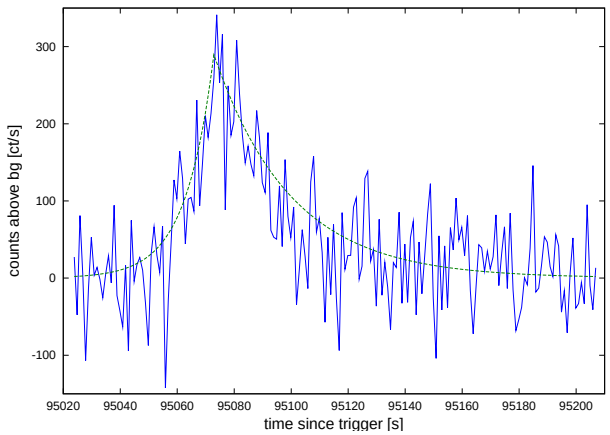

t_0[s]	R_0 [ct/s]	$\tau_{\rm rise}$ [s]	$\tau_{\rm decay}$ [s]
95072.9 ± 1.9	290 ± 19	9.9 ± 2.3	26.9 ± 3.4

A. Table of Individually Fitted Flares of SWIFT J195509.6+261406

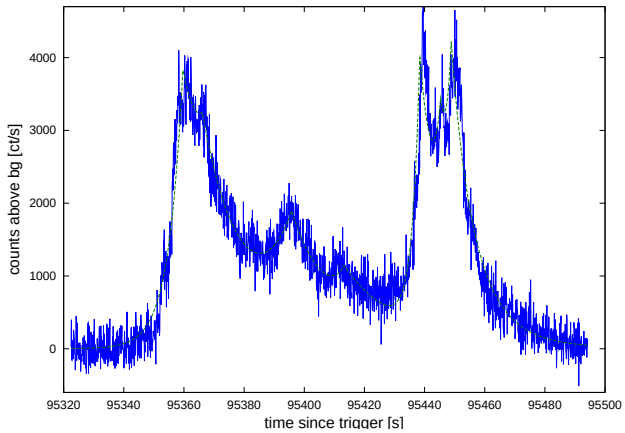

t_0[s]	R_0 [ct/s]	$\tau_{\rm rise}$ [s]	$\tau_{\rm decay}$ [s]
95359.6 ± 0.87	3400 ± 1100	4.6 ± 1.4	13 ± 11
95366.1 ± 3.1	1100 ± 1600	5.7 ± 8.2	13 ± 26
95395.8 ± 2.3	1560 ± 180	11 ± 5.8	14.5 ± 7.5
95413.3 ± 2.9	600 ± 270	5.3 ± 5	26 ± 12
95438.4 ± 0.42	3500 ± 400	2.46 ± 0.29	6.2 ± 2.4
95445.3 ± 1.5	1400 ± 1200	3.3 ± 3.4	3.3 ± 5.7
95448.9 ± 0.71	2900 ± 980	2.4 ± 1.5	9.1 ± 2

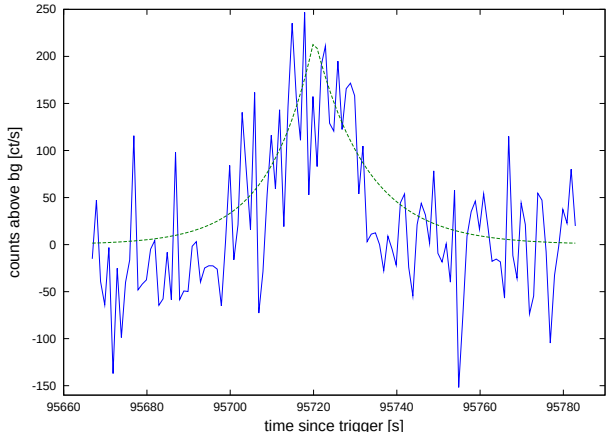

t_0[s]	R_0 [ct/s]	$\tau_{\rm rise}$ [s]	$\tau_{\rm decay}$ [s]
95720.2 ± 3	220 ± 24	10.7 ± 3.4	12.5 ± 3.6

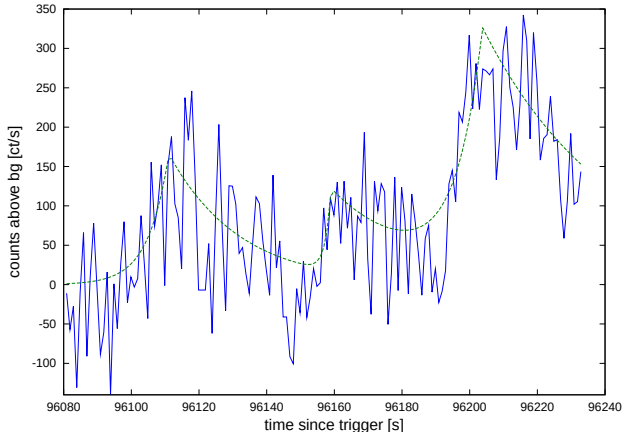

t_0[s]	R_0 [ct/s]	$\tau_{\rm rise}$ [s]	$\tau_{\rm decay}$ [s]
96111.1 ± 5.3	166 ± 29	6.1 ± 4.6	21 ± 9.3
96159 ± 5.7	104 ± 41	1.6 ± 2.5	27 ± 41
96203.8 ± 3.8	304 ± 54	7.8 ± 5.3	39 ± 16

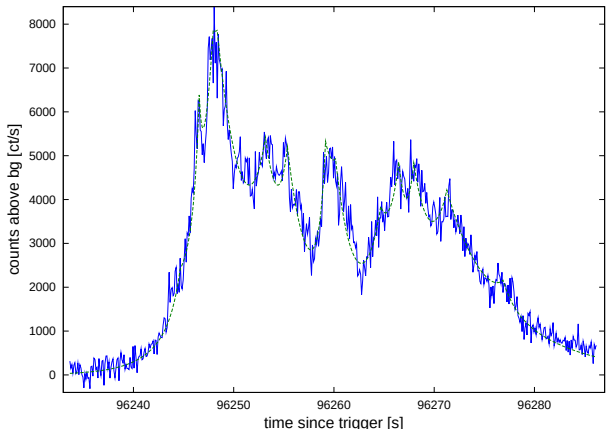

t_0[s]	R_0 [ct/s]	$\tau_{\rm rise}$ [s]	$\tau_{\rm decay}$ [s]
96244.7 ± 3.7	650 ± 740	0.7 ± 1.3	1.8 ± 6.9
96246.6 ± 1.2	2170 ± 380	0.42 ± 0.27	0.33 ± 0.17
96248 ± 2.4	4000 ± 5800	1.6 ± 1.4	3 ± 11
96248.4 ± 3.9	3900 ± 6900	3.1 ± 2.3	3 ± 11
96253.2 ± 6.7	3400 ± 2400	2.1 ± 1.3	2.1 ± 2.1
96255.4 ± 2.4	3000 ± 1700	1.1 ± 1	2.2 ± 1.9
96259.2 ± 2.2	2600 ± 1400	0.56 ± 0.42	1.7 ± 2.6
96260 ± 12	2600 ± 3400	2.1 ± 2.9	2.2 ± 2.4
96264.7 ± 4.5	2100 ± 3400	2.2 ± 2.6	2 ± 5.5
96266.5 ± 2	2800 ± 3500	1.7 ± 3.5	1.1 ± 1.8
96268 ± 2.4	3000 ± 2600	1 ± 1.7	3.1 ± 3.8
96271.3 ± 2.8	3000 ± 1400	2.1 ± 1.7	7.4 ± 3.4
96276.9 ± 4.3	560 ± 300	1.2 ± 2.3	1.2 ± 1.4

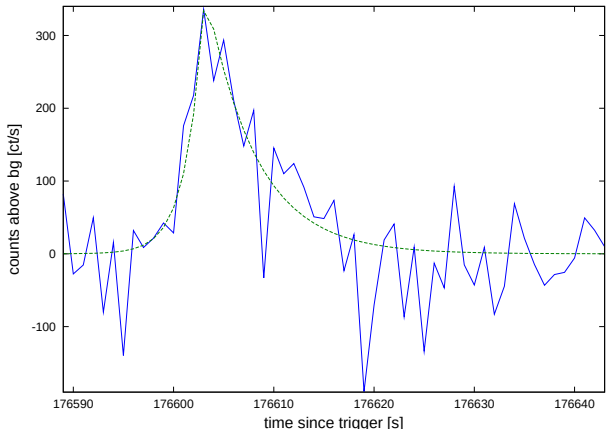

t_0[s]	R_0 [ct/s]	$\tau_{\rm rise}$ [s]	$\tau_{\rm decay}$ [s]
176603 ± 1.7	365 ± 52	1.8 ± 1.1	5 ± 1.8

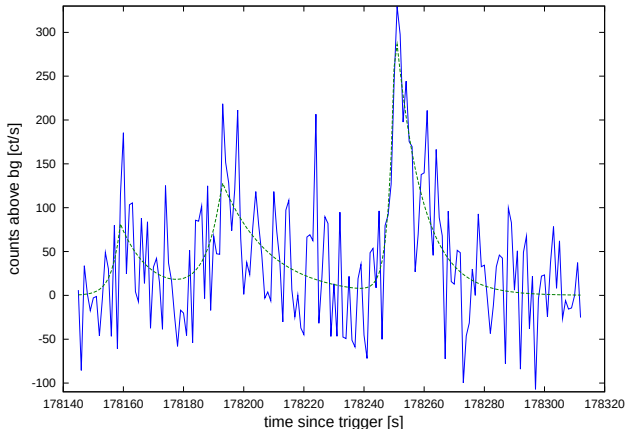

t_0[s]	R_0 [ct/s]	$\tau_{\rm rise}$ [s]	$\tau_{\rm decay}$ [s]
178159 ± 9	81 ± 39	2.8 ± 5.7	10 ± 14
178193 ± 5	127 ± 27	5.1 ± 5.8	16 ± 7.1
178250 ± 1.7	305 ± 38	1.99 ± 0.99	8.8 ± 2.2

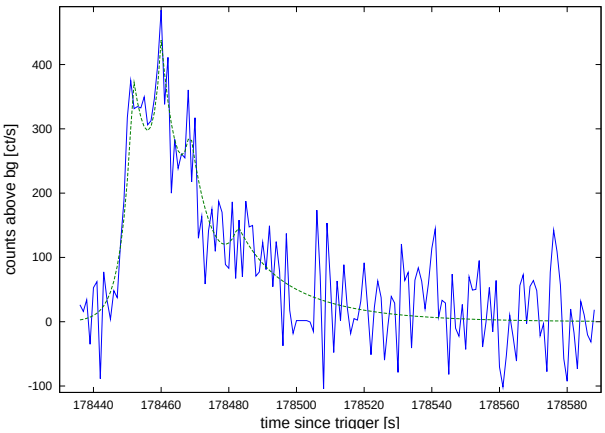

t_0[s]	R_0 [ct/s]	$\tau_{\rm rise}$ [s]	$\tau_{\rm decay}$ [s]
178452 ± 4.1	360 ± 240	3.2 ± 2.6	9 ± 37
178460 ± 11	280 ± 480	2.8 ± 7.6	6 ± 21
178469 ± 11	170 ± 410	3 ± 17	8 ± 33
178483 ± 7.8	100 ± 140	4 ± 14	21 ± 20

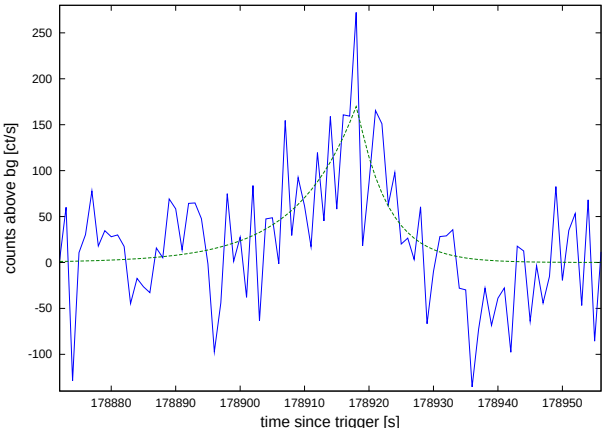

t_0[s]	R_0 [ct/s]	$\tau_{\rm rise}$ [s]	$\tau_{\rm decay}$ [s]
178918 ± 4.3	171 ± 30	9.1 ± 4.5	4.8 ± 3.5

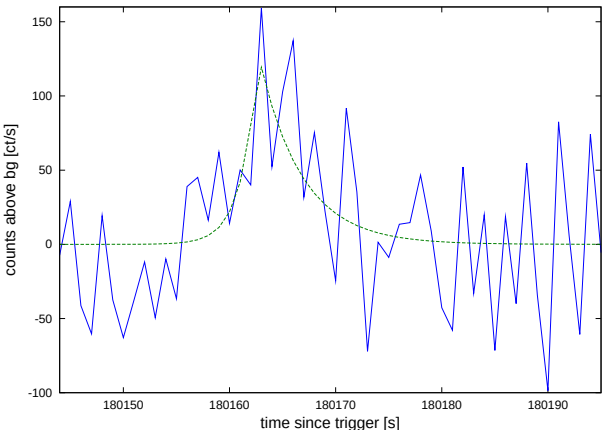

t_0[s]	R_0 [ct/s]	$\tau_{\rm rise}$ [s]	$\tau_{\rm decay}$ [s]
180163 ± 3.1	128 ± 43	1.5 ± 1.1	4 ± 2.4

List of Figures

1.1. Optical/X-ray cross-correlation of XTE J1118+480 6

2.1. OPTIMA instrument overview 8
2.2. OPTIMA at SKO 10
2.3. OPTIMA optical configuration 11
2.4. OPTIMA apertures 12
2.5. Wollaston prism 14
2.6. Linear polarization measurement principle 15
2.7. OPTIMA twin Wollaston schematic 15
2.8. OPTIMA polarimeter technical drawing 16
2.9. Fibre optical coupling 18
2.10. Tapered fibre optical coupling 19
2.11. QE of Perkin-Elmer APDs 20
2.12. Photo multiplier schematic 20
2.13. APD concept 21
2.14. Conventional OPTIMA DAQ 26
2.15. Event-based OPTIMA DAQ 27

3.1. Screenshot: XEphem 34
3.2. Screenshot: Autofocus 35
3.3. Fiducual lights 36
3.4. Screenshot: OPTIMA-Burst session 39
3.5. GCN Overview 41

4.1. Adaptive binning light-curve compared to constant binning 46
4.2. Pile-up effects 51
4.3. Pile-up correction 54
4.4. Monte-Carlo validation of pile-up correction 55
4.5. Normalization factors of fibre-bundle 56

5.1. Swift GRB all-sky map 61
5.2. OPTIMA light-curve of GRB 090726 64
5.3. Overview over all observations of GRB 090726 66
5.4. Comparison of OPTIMA and literature light-curve of GRB 090726 67
5.5. Light-curve of GRB 060904b 68
5.6. Light-curve of GRB 060926 70
5.7. OPTIMA-Burst GRB upper limits in context 73

6.1. BAT light-curve of GRB 070610 76
6.2. OPTIMA detection of J1955 77
6.3. XRT lightcurve of J1955 78
6.4. XRT spectrum of J1955 79

6.5. The red-clump distance estimation method 80
6.6. First OPTIMA light-curve of J1955 81
6.7. Overview over total OPTIMA light-curve of J1955 82
6.8. Comparison of flares in IAC-80 CCD and OPTIMA 83
6.9. Flux calibration of OPTIMA light-curve using IAC-80 84
6.10. Detailed light-curve of flares 85
6.11. High time-resolution detail of bright flare 86
6.12. PSD of bright flares 87
6.13. Histogram of flare brightness 88
6.14. Morphological similarity of optical and X-ray light-curves 89

Acronyms

AGILE Astro-rivelatore Gamma a Immagini Leggero.

APD Avalanche Photo-Diode.

ASM All-Sky Monitor.

AXP Anomalous X-ray Pulsar.

BACODINE BATSE Coordinate Distribution Network.

BAT Burst Alert Telescope.

BATSE Burst and Transient Source Experiment.

CAHA Centro Astronómico Hispano-Alemán.

CCD Charge-Coupled Device.

CGRO Compton Gamma-ray Observatory.

CPU Central Processing Unit.

CrAO Crimean Astrophysical Observatory.

DAQ Data Acquisition System.

DEPFET Depleted P-channel Field-effect Transistor.

DIN Dim Isolated Neutron Star.

DIO Digital Input/Output.

DMA Direct Memory Access.

DSS Digitized Sky Survey.

EGNOS European Geostationary Navigation Overlay Service.

emCCD electron multiplying CCD.

FC Ferrule Connector.

FFT Fast Fourier Transform.

fits Flexible Image Transfer Format.

FORTH Foundation for Research and Technology – Hellas.

FoV Field of View.

FPGA Field-Programmable Gate Array.

FRED Fast Rise, Exponential Decay.

FWHM Full Width at Half Maximum.

GAM Guider Acquisition Module.

GCN GRB Coordinate Network.

GHO Guillermo Haro Observatory.

GLAST Gamma-Ray Large-Area Space Telescope.

GPS Global Positioning System.

GRB γ-Ray Burst.

GROND Gamma-Ray Burst Optical/Near-Infrared Detector.

HTRA High Time Resolution Astronomy.

IAC Instituto de Astrofísica de Canarias.

IBAS Integral Burst Alert System.

INTEGRAL International Gamma-Ray Astrophysics Laboratory.

IPC Inter-Process Communication.

IR Infra-Red.

LED Light Emitting Diodes.

LOFAR Low Frequency Array.

LOTIS Livermore Optical Transient Imaging System.

LSB Least Significant Bit.

LSSA Least-squares spectral analysis.

LSST Large Synoptic Survey Telescope.

MASTER Mobile Astronomical System of the TElescope-Robots.

MPE Max-Planck-Institut für extraterrestrische Physik.

nIR Near Infra-Red.

NOT Nordic Optical Telescope.

OCXO Oven-Controlled Crystal Oscillator.

OPTIMA Optical Pulsar Timing Analyzer.

OS Operating System.

OT Optical Transient.

PanSTARRS Panoramic Survey Telescope and Rapid Response System.

PDF Probability Density Function.

PIN p-i-n Diode.

PMT Photo Multiplier Tube.

POSIX Portable Operating System Interface for Unix.

ppm parts per million.

PSD Power Spectral Density.

PSF Point-Spread Function.

RAPTOR Rapid Telescopes for Optical Response.

RNDR Repeated Non-Destructive Read-out.

ROTSE Robotic Transient Search Experiment.

RTOS Real-Time Operating System.

RXTE Rossi X-ray Timing Explorer.

SAAO South African Astronomical Observatory.

SAORAS Special Astrophysical Observatory of the Russian Academy of Science.

SGR Soft γ-ray Repeater.

SKA Square Kilometre Array.

SKO Skinakas Observatory.

SNR Signal to Noise Ratio.

SPAD Single Photon Sensitive APD.

TAROT Télescopes à Action Rapide pour les Objets Transitoires.

TCS Telescope Control System.

TCXO Temperature Compensated Crystal Oscillator.

TDRSS Tracking and Data Relay Satellite System.

TTL Transistor-Transistor Logic.

UoC University of Crete.

USB Universal Serial Bus.

USNO US Naval Observatory.

UT Universal Time.

UTC Coordinated Universal Time.

UVOT UV and Optical Telescope.

VISTA Visible and Infrared Survey Telescope for Astronomy.

WAAS Wide Area Augmentation System.

WCS World Coordinate System.

WWW World Wide Web.

XO Crystal Oscillator (from Xtal).

XRT X-Ray Telescope.

Bibliography

[Akerlof et al., 2000] Akerlof, C., Balsano, R., Barthelmy, S., Bloch, J., Butterworth, P., Casperson, D., Cline, T., Fletcher, S., Frontera, F., Gisler, G., Heise, J., Hills, J., Hurley, K., Kehoe, R., Lee, B., Marshall, S., McKay, T., Pawl, A., Piro, L., Szymanski, J., and Wren, J. (2000). Prompt Optical Observations of Gamma-Ray Bursts. ApJ, 532:L25–L28. [ADS].

[Barbieri et al., 2009] Barbieri, C., Naletto, G., Capraro, I., Occhipinti, T., Verroi, E., Zoccarato, P., Facchinetti, C., Germanà, C., Parrazzani, M., Zaccariotto, M., Anzolin, G., Tamburini, F., di Paola, A., Giro, E., Bonanno, G., Billotta, S., Pernechele, C., Bolli, P., Zampieri, L., Possenti, A., and Cadez, A. (2009). Very fast photon counting photometers for astronomical applications: IquEYE for the ESO 3.5m New Technology Telescope. In *Society of Photo-Optical Instrumentation Engineers (SPIE) Conference Series*, volume 7355 of *Society of Photo-Optical Instrumentation Engineers (SPIE) Conference Series*. [ADS].

[Barthelmy, 2005] Barthelmy, S. D. (2005). Swift Burst Data Products in GCN. In *American Astronomical Society Meeting Abstracts*, volume 37 of *Bulletin of the American Astronomical Society*, pages 151.08–+. [ADS].

[Bay et al., 2006] Bay, T. J., Burney, J. A., Barral, J., Brink, P. L., Cabrera, B., Castle, J. P., Miller, A. J., Nam, S. W., Romani, R. W., and Tomada, A. (2006). The optical imaging TES detector array: Considerations for a cryogenic imaging instrument. *Nuclear Instruments and Methods in Physics Research A*, 559:506–508. [ADS].

[Beloborodov and Thompson, 2007] Beloborodov, A. M. and Thompson, C. (2007). Corona of Magnetars. ApJ, 657:967–993. [ADS].

[Berger et al., 2009] Berger, E., Cucchiara, A., Fox, D. B., and Levan, A. J. (2009). GRB 090621B: Gemini spectrum of afterglow candidate. *GRB Coordinates Network*, 9559:1–+. [ADS].

[Bertin and Arnouts, 1996] Bertin, E. and Arnouts, S. (1996). SExtractor: Software for source extraction. A&AS, 117:393–404. [ADS].

[Burnham, 1978] Burnham, R. (1978). *Burnham's celestial handbook: an observer's guide to the Universe beyond the solar system*. Burnham's Celestial Handbook: An Observer's Guide to the Universe Beyond the Solar System. Dover Publications.

[Cardelli et al., 1989] Cardelli, J. A., Clayton, G. C., and Mathis, J. S. (1989). The relationship between infrared, optical, and ultraviolet extinction. ApJ, 345:245–256. [ADS].

[Castro-Tirado et al., 2008] Castro-Tirado, A. J., de Ugarte Postigo, A., Gorosabel, J., Jelínek, M., Fatkhullin, T. A., Sokolov, V. V., Ferrero, P., Kann, D. A., Klose, S., Sluse, D., Bremer, M., Winters, J. M., Nuernberger, D., Pérez-Ramírez, D., Guerrero,

M. A., French, J., Melady, G., Hanlon, L., McBreen, B., Leventis, K., Markoff, S. B., Leon, S., Kraus, A., Aceituno, F. J., Cunniffe, R., Kubánek, P., Vítek, S., Schulze, S., Wilson, A. C., Hudec, R., Durant, M., González-Pérez, J. M., Shahbaz, T., Guziy, S., Pandey, S. B., Pavlenko, L., Sonbas, E., Trushkin, S. A., Bursov, N. N., Nizhelskij, N. A., Sánchez-Fernández, C., and Sabau-Graziati, L. (2008). Flares from a candidate Galactic magnetar suggest a missing link to dim isolated neutron stars. Nature, 455:506–509. [ADS].

[Cenko et al., 2009] Cenko, S. B., Levan, A. J., Kasliwal, M. M., and Kulkarni, S. R. (2009). GRB 090621B: P60 observations. *GRB Coordinates Network*, 9557:1–+. [ADS].

[Cocke et al., 1969] Cocke, W. J., Disney, M. J., and Taylor, D. J. (1969). Discovery of Optical Signals from Pulsar NP 0532. Nature, 221:525–527. [ADS].

[Costa et al., 2008] Costa, E., Bellazzini, R., Bregeon, J., Brez, A., Frutti, M., Di Cosimo, S., Latronicio, L., Lazzarotto, F., Matt, G., Minuti, M., Morelli, E., Muleri, F., Pinchera, M., Razzano, M., Rubini, A., Soffitta, P., and Spandre, G. (2008). XPOL: a photoelectric polarimeter onboard XEUS. In *Society of Photo-Optical Instrumentation Engineers (SPIE) Conference Series*, volume 7011 of *Presented at the Society of Photo-Optical Instrumentation Engineers (SPIE) Conference*. [ADS].

[Cucchiara et al., 2011] Cucchiara, A., Levan, A. J., Fox, D. B., Tanvir, N. R., Ukwatta, T. N., Berger, E., Krühler, T., Küpcü Yoldaş, A., Wu, X. F., Toma, K., Greiner, J., Olivares, F. E., Rowlinson, A., Amati, L., Sakamoto, T., Roth, K., Stephens, A., Fritz, A., Fynbo, J. P. U., Hjorth, J., Malesani, D., Jakobsson, P., Wiersema, K., O'Brien, P. T., Soderberg, A. M., Foley, R. J., Fruchter, A. S., Rhoads, J., Rutledge, R. E., Schmidt, B. P., Dopita, M. A., Podsiadlowski, P., Willingale, R., Wolf, C., Kulkarni, S. R., and D'Avanzo, P. (2011). A Photometric Redshift of z ˜ 9.4 for GRB 090429B. ApJ, 736:7–+. [ADS].

[Cummings et al., 2006] Cummings, J., Barbier, L., Barthelmy, S. D., Fenimore, E., Gehrels, N., Holland, S. T., Hullinger, D., Krimm, H., Markwardt, C., Palmer, D., Parsons, A., Sakamoto, T., Sato, G., Stamatikos, M., and Tueller, J. (2006). GRB 060926, Swift-BAT refined analysis. *GRB Coordinates Network*, 5621:1–+. [ADS].

[Davis, 1957] Davis, G. A. (1957). Why Did the Arabs Call Beta Persei "al-Ghul"? S&T, 16:177–+. [ADS].

[Del Monte et al., 2008] Del Monte, E., Costa, E., Donnarumma, I., Evangelista, Y., Feroci, M., Lapshov, I., Lazzarotto, F., Rapisarda, M., Soffitta, P., Argan, A., Barbiellini, G., Basset, M., Bulgarelli, A., Caraveo, P., Chen, A., Di Cocco, G., Foggetta, L., Fuschino, F., Galli, M., Gianotti, F., Giuliani, A., Labanti, C., Lipari, P., Longo, F., Marisaldi, M., Mauri, F., Mereghetti, S., Morselli, A., Pellizzoni, A., Perotti, F., Picozza, P., Prest, M., Pucella, G., Tavani, M., Trifoglio, M., Trois, A., Vallazza, E., Vercellone, S., Vittorini, V., Zambra, A., Romano, P., Burrows, D. N., Chincarini, G., Gehrels, N., La Parola, V., O'Brien, P. T., Osborne, J. P., Preger, B., Pittori, C., Antonelli, L. A., Verrecchia, F., Giommi, P., and Salotti, L. (2008). GRB 070724B: the first Gamma Ray Burst localized by SuperAGILE. In M. Galassi, D. Palmer, & E. Fenimore, editor, *American Institute of Physics Conference Series*, volume 1000 of *American Institute of Physics Conference Series*, pages 105–108. [ADS].

[Dhillon et al., 2007] Dhillon, V. S., Marsh, T. R., Stevenson, M. J., Atkinson, D. C., Kerry, P., Peacocke, P. T., Vick, A. J. A., Beard, S. M., Ives, D. J., Lunney, D. W., McLay, S. A., Tierney, C. J., Kelly, J., Littlefair, S. P., Nicholson, R., Pashley, R., Harlaftis, E. T., and O'Brien, K. (2007). ULTRACAM: an ultrafast, triple-beam CCD camera for high-speed astrophysics. MNRAS, 378:825–840. [ADS].

[Downey, 2005] Downey, E. (2005). XEphem – the serious interactive astronomical software ephemeris. *http://www.clearskyinstitute.com/xephem/*. [LINK].

[Duncan and Thompson, 1996] Duncan, R. C. and Thompson, C. (1996). Magnetars. In R. E. Rothschild & R. E. Lingenfelter, editor, *High Velocity Neutron Stars*, volume 366 of *American Institute of Physics Conference Series*, pages 111–117. [ADS].

[Durant and van Kerkwijk, 2006] Durant, M. and van Kerkwijk, M. H. (2006). Distances to Anomalous X-Ray Pulsars Using Red Clump Stars. ApJ, 650:1070–1081. [ADS].

[Duscha, 2007] Duscha, S. (2007). Software design and development of the improved OPTIMA data acquisition system. Master's thesis, National University of Ireland, Galway.

[Evans et al., 2009] Evans, P. A., Beardmore, A. P., Page, K. L., Osborne, J. P., O'Brien, P. T., Willingale, R., Starling, R. L. C., Burrows, D. N., Godet, O., Vetere, L., Racusin, J., Goad, M. R., Wiersema, K., Angelini, L., Capalbi, M., Chincarini, G., Gehrels, N., Kennea, J. A., Margutti, R., Morris, D. C., Mountford, C. J., Pagani, C., Perri, M., Romano, P., and Tanvir, N. (2009). Methods and results of an automatic analysis of a complete sample of Swift-XRT observations of GRBs. MNRAS, 397:1177–1201. [ADS].

[Evans et al., 2007] Evans, P. A., Beardmore, A. P., Page, K. L., Tyler, L. G., Osborne, J. P., Goad, M. R., O'Brien, P. T., Vetere, L., Racusin, J., Morris, D., Burrows, D. N., Capalbi, M., Perri, M., Gehrels, N., and Romano, P. (2007). An online repository of Swift/XRT light curves of γ-ray bursts. A&A, 469:379–385. [ADS].

[Fabian et al., 1982] Fabian, A. C., Guilbert, P. W., Motch, C., Ricketts, M., Ilovaisky, S. A., and Chevalier, C. (1982). GX 339-4 - Cyclotron radiation from an accretion flow. A&A, 111:L9+. [ADS].

[Fatkhullin et al., 2009] Fatkhullin, T., Gorosabel, J., de Ugarte Postigo, A., Moskvitin, A., Valeev, A., Fabrika, S., Sholukhova, O., Castro-Tirado, A., and Sokolov, V. (2009). GRB090726: 6-meter telescope redshift. *GRB Coordinates Network*, 9712:1–+. [ADS].

[Fynbo et al., 2009] Fynbo, J. P. U., Jakobsson, P., Prochaska, J. X., Malesani, D., Ledoux, C., de Ugarte Postigo, A., Nardini, M., Vreeswijk, P. M., Wiersema, K., Hjorth, J., Sollerman, J., Chen, H.-W., Thöne, C. C., Björnsson, G., Bloom, J. S., Castro-Tirado, A. J., Christensen, L., De Cia, A., Fruchter, A. S., Gorosabel, J., Graham, J. F., Jaunsen, A. O., Jensen, B. L., Kann, D. A., Kouveliotou, C., Levan, A. J., Maund, J., Masetti, N., Milvang-Jensen, B., Palazzi, E., Perley, D. A., Pian, E., Rol, E., Schady, P., Starling, R. L. C., Tanvir, N. R., Watson, D. J., Xu, D., Augusteijn, T., Grundahl, F., Telting, J., and Quirion, P.-O. (2009). Low-resolution Spectroscopy of Gamma-ray Burst Optical Afterglows: Biases in the Swift Sample and Characterization of the Absorbers. ApJS, 185:526–573. [ADS].

[Galeev et al., 2009] Galeev, A., Bikmaev, I., Sakhibullin, N., Burenin, R., Pavlinsky, M., Sunyaev, R., Khamitov, I., Eker, Z., Kiziloglu, U., and Gogus, E. (2009). GRB 090621B: RTT150 optical observations. *GRB Coordinates Network*, 9549:1–+. [ADS].

[Ghisellini et al., 2009] Ghisellini, G., Nardini, M., Ghirlanda, G., and Celotti, A. (2009). A unifying view of gamma-ray burst afterglows. MNRAS, 393:253–271. [ADS].

[Goodricke, 1784] Goodricke, J. (1784). On the Periods of the Changes of Light in the Star Algol. in a Letter from John Goodricke, Esq. to the Rev. Anthony Shepherd, D. D. F. R. S. Professor of Astronomy at Cambridge. *Royal Society of London Philosophical Transactions Series I*, 74:287–292. [ADS].

[Goodricke and Bayer, 1786] Goodricke, J. and Bayer, J. (1786). a Series of Observations on, and a Discovery of, the Period of the Variation of the Light of the Star Marked δ by Bayer, Near the Head of Cepheus. in a Letter from John Goodricke, Esq. to Nevil Maskelyne, D. D. F. R. S. and Astronomer Royal. *Royal Society of London Philosophical Transactions Series I*, 76:48–61. [ADS].

[Grupe et al., 2006] Grupe, D., Barthelmy, S. D., Chester, M. M., Cummings, J. R., Holland, S. T., Hunsberger, S. D., Kennea, J. A., Krimm, H. A., Markwardt, C. B., Marshall, F. E., Palmer, D. M., Stamatikos, M., and Stroh, M. C. (2006). GRB 060904B: Swift detection of a burst with optical counterpart. *GRB Coordinates Network*, 5505:1–+. [ADS].

[Gösch et al., 2004] Gösch, M., Serov, A., Anhut, T., Lasser, T., Rochas, A., Besse, P.-A., Popovic, R. S., Blom, H., and Rigler, R. (2004). Parallel single molecule detection with a fully integrated single-photon 2x2 cmos detector array. *Journal of Biomedical Optics*, 9(5):913–921.

[Helene, 1983] Helene, O. (1983). Upper limit of peak area. *Nuclear Instruments and Methods in Physics Research*, 212(1-3):319 – 322.

[Helene, 1984] Helene, O. (1984). Errors in experiments with small numbers of events. *Nuclear Instruments and Methods in Physics Research Section A: Accelerators, Spectrometers, Detectors and Associated Equipment*, 228(1):120 – 128.

[Hewish et al., 1968] Hewish, A., Bell, S. J., Pilkington, J. D. H., Scott, P. F., and Collins, R. A. (1968). Observation of a Rapidly Pulsating Radio Source. Nature, 217:709–713. [ADS].

[Holland et al., 2006] Holland, S. T., Barthelmy, S. D., Burrows, D. N., Capalbi, M., Conciatore, M. L., Cummings, J. R., Gehrels, N., Guidorzi, C., Kennea, J. A., Krimm, H. A., Mangano, V., Markwardt, C. B., Marshall, F. E., Osborne, J. P., Page, K. L., Palmer, D. M., Romano, P., Sato, G., Stamatikos, M., vanden Berk, D. E., and Ziaeepour, H. (2006). GRB 060926: Swift detection of a burst. *GRB Coordinates Network*, 5612:1–+. [ADS].

[Hubble, 1925] Hubble, E. P. (1925). Cepheids in spiral nebulae. *The Observatory*, 48:139–142. [ADS].

[Hurley et al., 2005] Hurley, K., Boggs, S. E., Smith, D. M., Duncan, R. C., Lin, R., Zoglauer, A., Krucker, S., Hurford, G., Hudson, H., Wigger, C., Hajdas, W., Thompson, C., Mitrofanov, I., Sanin, A., Boynton, W., Fellows, C., von Kienlin, A., Lichti, G., Rau, A., and Cline, T. (2005). An exceptionally bright flare from SGR 1806-20 and the origins of short-duration γ-ray bursts. Nature, 434:1098–1103. [ADS].

[Hurley et al., 1999] Hurley, K., Kouveliotou, C., Woods, P., Cline, T., Butterworth, P., Mazets, E., Golenetskii, S., and Frederics, D. (1999). Reactivation and Precise Interplanetary Network Localization of the Soft Gamma Repeater SGR 1900+14. ApJ, 510:L107–L109. [ADS].

[Hurley et al., 1994] Hurley, K. J., McBreen, B., Rabbette, M., and Steel, S. (1994). The lognormal properties of the soft gamma-ray repeater SGR 1806-20 and the VELA pulsar. A&A, 288:L49–L52. [ADS].

[Hynes et al., 1998] Hynes, R. I., O'Brien, K., Horne, K., Chen, W., and Haswell, C. A. (1998). Echoes from an irradiated disc in GRO J1655-40. MNRAS, 299:L37–L41. [ADS].

[Joye and Mandel, 2003] Joye, W. A. and Mandel, E. (2003). New Features of SAOImage DS9. In H. E. Payne, R. I. Jedrzejewski, & R. N. Hook, editor, *Astronomical Data Analysis Software and Systems XII*, volume 295 of *Astronomical Society of the Pacific Conference Series*, pages 489–+. [ADS].

[Kanbach et al., 2003] Kanbach, G., Kellner, S., Schrey, F. Z., Steinle, H., Straubmeier, C., and Spruit, H. C. (2003). Design and results of the fast timing photo-polarimeter OPTIMA. In M. Iye & A. F. M. Moorwood, editor, *Society of Photo-Optical Instrumentation Engineers (SPIE) Conference Series*, volume 4841 of *Society of Photo-Optical Instrumentation Engineers (SPIE) Conference Series*, pages 82–93. [ADS].

[Kanbach et al., 2001] Kanbach, G., Straubmeier, C., Spruit, H. C., and Belloni, T. (2001). Correlated fast X-ray and optical variability in the black-hole candidate XTE J1118+480. Nature, 414:180–182. [ADS].

[Kann et al., 2011] Kann, D. A., Klose, S., Zhang, B., Covino, S., Butler, N. R., Malesani, D., Nakar, E., Wilson, A. C., Antonelli, L. A., Chincarini, G., Cobb, B. E., D'Avanzo, P., D'Elia, V., Della Valle, M., Ferrero, P., Fugazza, D., Gorosabel, J., Israel, G. L., Mannucci, F., Piranomonte, S., Schulze, S., Stella, L., Tagliaferri, G., and Wiersema, K. (2011). The Afterglows of Swift-era Gamma-Ray Bursts. II. Type I GRB versus Type II GRB Optical Afterglows. ApJ, 734:96–+. [ADS].

[Kann et al., 2007] Kann, D. A., Wilson, A. C., Schulze, S., Klose, S., Henze, M., Ludwig, F., Laux, U., and Greiner, J. (2007). GRB 070610: TLS RRM sees flaring behaviour - galactic transient? *GRB Coordinates Network*, 6505:1–+. [ADS].

[Kasliwal et al., 2008] Kasliwal, M. M., Cenko, S. B., Kulkarni, S. R., Cameron, P. B., Nakar, E., Ofek, E. O., Rau, A., Soderberg, A. M., Campana, S., Bloom, J. S., Perley, D. A., Pollack, L. K., Barthelmy, S., Cummings, J., Gehrels, N., Krimm, H. A., Markwardt, C. B., Sato, G., Chandra, P., Frail, D., Fox, D. B., Price, P. A., Berger, E., Grebenev, S. A., Krivonos, R. A., and Sunyaev, R. A. (2008). GRB 070610: A Curious Galactic Transient. ApJ, 678:1127–1135. [ADS].

[Khamitov et al., 2008] Khamitov, I., Parmaksizoglu, M., Alis, S., Hudaverdi, M., Eker, Z., Kiziloglu, U., Gogus, E., Burenin, R., Pavlinsky, M., Sunyaev, R., Bikmaev, I., and Sakhibullin, N. (2008). GRB 081102: RTT150 optical observations. *GRB Coordinates Network*, 8520:1–+. [ADS].

[Klotz et al., 2008] Klotz, A., Gendre, B., Stratta, G., Galli, A., Corsi, A., Preger, B., Cutini, S., Pélangeon, A., Atteia, J. L., Boër, M., and Piro, L. (2008). Early emission of

rising optical afterglows: the case of GRB 060904B and GRB 070420. A&A, 483:847–855. [ADS].

[Kosugi et al., 2005] Kosugi, G., Ogasawara, R., and Terada, H. (2005). A Variable Infrared Counterpart to the Soft Gamma-Ray Repeater SGR 1806-20. ApJ, 623:L125–L128. [ADS].

[Kouveliotou, 2003] Kouveliotou, C. (2003). A Review of Soft Gamma Repeaters (SGRs). In van den Heuvel, E. P., Kaper, L., Rol, E., and Wijers, R. A. M. J., editors, *Astronomical Society of the Pacific Conference Series*, volume 308 of *Astronomical Society of the Pacific Conference Series*, pages 413–+. [ADS].

[Kraft et al., 1991] Kraft, R. P., Burrows, D. N., and Nousek, J. A. (1991). Determination of confidence limits for experiments with low numbers of counts. ApJ, 374:344–355. [ADS].

[Krimm et al., 2009] Krimm, H. A., Barthelmy, S. D., Baumgartner, W. H., Cummings, J. R., Fenimore, E. E., Gehrels, N., Markwardt, C. B., Page, K. L., Palmer, D. M., Parsons, A. M., Sakamoto, T., Sato, G., Stamatikos, M., Tueller, J., and Ukwatta, T. N. (2009). GRB 090726, Swift-BAT refined analysis. *GRB Coordinates Network*, 9716:1–+. [ADS].

[Kruehler et al., 2009] Kruehler, T., Klose, S., and Greiner, J. (2009). GRB 090628: GROND upper limits. *GRB Coordinates Network*, 9591:1–+. [ADS].

[Kubanek et al., 2009] Kubanek, P., Morales, N., Ortiz, J. L., de Ugarte Postigo, A., Gorosabel, J., Castro-Tirado, A. J., and Jelinek, M. (2009). GRB 090628: 1.23m CAHA optical observations. *GRB Coordinates Network*, 9589:1–+. [ADS].

[Kyne et al., 2010] Kyne, G., Sheehan, B., Collins, P., Redfern, M., and Shearer, A. (2010). GASP-Galway astronomical Stokes polarimeter. *API'09 - First NanoCharM Workshop on Advanced Polarimetric Instrumentation, Palaiseau, France, Edited by E. Garcia-Caurel; A. de Martino; EPJ Web of Conferences, Volume 5, id.05003*, 50:5003–+. [ADS].

[Leavitt and Pickering, 1912] Leavitt, H. S. and Pickering, E. C. (1912). Periods of 25 Variable Stars in the Small Magellanic Cloud. *Harvard College Observatory Circular*, 173:1–3. [ADS].

[Levan et al., 2009] Levan, A. J., Curran, P., Wiersema, K., and Groot, P. (2009). GRB 090621B: optical observations. *GRB Coordinates Network*, 9547:1–+. [ADS].

[Lipunov et al., 2008a] Lipunov, V., Kornilov, V., Gorbovskoy, E., Belinski, A., Shatskiy, N., Tyurina, N., Kuvshinov, D., Balanutsa, P., Tlatov, A., Golubov, I., Krushinski, V., Zalognikh, I., Yazev, S., and Ivanov, K. (2008a). GRB 081102: MASTER VWF promt observation. *GRB Coordinates Network*, 8464:1–+. [ADS].

[Lipunov et al., 2008b] Lipunov, V., Kornilov, V., Gorbovskoy, E., Belinski, A., Shatskiy, N., Tyurina, N., Kuvshinov, D., Balanutsa, P., Tlatov, A., Parkhomenko, A., Krushinski, V., Zalognikh, I., Yazev, S., and Ivanov, K. (2008b). GRB 081102: MASTER prompt optical limit. *GRB Coordinates Network*, 8471:1–+. [ADS].

[Lipunov et al., 2008c] Lipunov, V. M., Kornilov, V. G., Gorbovskoy, E. S., Krylov, A. V., Tyurina, N. V., Kuvshinov, D. A., Belinski, A. A., Gritsyk, P. A., Sankovich, A. V., and Vladimirov, V. V. (2008c). Discovery of an optical flare from GRB 060926 by the MASTER robotic telescope: Possible formation of a marginally rotating black hole. *Astronomy Letters*, 34:145–151. [ADS].

[Lomb, 1976] Lomb, N. R. (1976). Least-squares frequency analysis of unequally spaced data. Ap&SS, 39:447–462. [ADS].

[Loredo, 1990] Loredo, T. (1990). From laplace to supernova sn 1987a: Bayesian inference in astrophysics. *Maximum entropy and Bayesian methods*, 39:81–142.

[Mangano et al., 2009] Mangano, V., Sbarufatti, B., Palmer, D. M., Hoversten, E. A., Siegel, M. H., Barthelmy, S. D., Burrows, D. N., Roming, P., and Gehrels, N. (2009). Swift observations of GRB 090628. *GCN Report*, 226:1–+. [ADS].

[Markwardt et al., 2006] Markwardt, C., Barbier, L., Barthelmy, S. D., Cummings, J., Fenimore, E., Gehrels, N., Grupe, D., Hullinger, D., Krimm, H., Palmer, D., Parsons, A., Sakamoto, T., Sato, G., Stamatikos, M., and Tueller, J. (2006). GRB 060904B: Swift-BAT refined analysis. *GRB Coordinates Network*, 5520:1–+. [ADS].

[Markwardt et al., 2007] Markwardt, C. B., Pagani, C., Evans, P., Gavriil, F. P., Kennea, J. A., Krimm, H. A., Landsman, W., and Marshall, F. E. (2007). SWIFT J195509.6+261406 / GRB 070610: A Potential Galactic Transient. *The Astronomer's Telegram*, 1102:1–+. [ADS].

[Maticic and Skvarc, 2009] Maticic, S. and Skvarc, J. (2009). GRB 090726: afterglow candidate photometryfrom crni vrh. *GRB Coordinates Network*, 9715:1–+. [ADS].

[McClintock et al., 2001] McClintock, J. E., Garcia, M. R., Caldwell, N., Falco, E. E., Garnavich, P. M., and Zhao, P. (2001). A Black Hole Greater Than 6 M_{solar} in the X-Ray Nova XTE J1118+480. ApJ, 551:L147–L150. [ADS].

[Mereghetti et al., 2006] Mereghetti, S., Paizis, A., Gotz, D., Shaw, S., Beck, M., and Borkowski, J. (2006). GRB 060901: a long GRB detected by INTEGRAL. *GRB Coordinates Network*, 5491:1–+. [ADS].

[Meszáros, 2007] Meszáros, P. (2007). Gamma-Ray Bursts in the Light of Swift. In di Salvo, T., Israel, G. L., Piersant, L., Burderi, L., Matt, G., Tornambe, A., and Menna, M. T., editors, *The Multicolored Landscape of Compact Objects and Their Explosive Origins*, volume 924 of *American Institute of Physics Conference Series*, pages 3–16. [ADS].

[Mink, 2002] Mink, D. J. (2002). WCSTools 3.0: More Tools for Image Astrometry and Catalog Searching. In D. A. Bohlender, D. Durand, & T. H. Handley, editor, *Astronomical Data Analysis Software and Systems XI*, volume 281 of *Astronomical Society of the Pacific Conference Series*, pages 169–+. [ADS].

[Montanari, 1671] Montanari, G. (1671). Sopra la sparizione d'alcune stelle et altre novità celesti. In Zani, V., editor, *Prose de' Signori Accademici Gelati di Bologna distinte ne' seguenti trattati ...* Per li Manolessi.

[Moskvitin et al., 2009a] Moskvitin, A., Fatkhullin, T., and Valeev, A. (2009a). GRB 090726: optical transient candidate. *GRB Coordinates Network*, 9709:1–+. [ADS].

[Moskvitin et al., 2009b] Moskvitin, A., Spiridonova, O., Valeev, A., and Fatkhullin, T. (2009b). GRB080628: SAO RAS optical observations. *GRB Coordinates Network*, 9594:1–+. [ADS].

[Motch et al., 1983] Motch, C., Ricketts, M. J., Page, C. G., Ilovaisky, S. A., and Chevalier, C. (1983). Simultaneous X-ray/optical observations of GX339-4 during the May 1981 optically bright state. A&A, 119:171–176. [ADS].

[Mühlegger, 2006] Mühlegger, M. (2006). Entwicklung und Einsatz eines Wollaston–Polarimeters für die Hochgeschwindigkeitsastronomie mit OPTIMA–Burst. Master's thesis, Technische Universität München.

[Nather et al., 1969] Nather, R. E., Warner, B., and Macfarlane, M. (1969). Optical Pulsations in the Crab Nebula Pulsar. Nature, 221:527–529. [ADS].

[Pagani et al., 2007a] Pagani, C., Barthelmy, S. D., Cummings, J. R., Gehrels, N., Grupe, D., Holland, S. T., Kennea, J. A., Markwardt, C. B., Marshall, F. E., O'Brien, P. T., Palmer, D. M., Parsons, A. M., Stamatikos, M., and Vetere, L. (2007a). GRB 070610: Swift detection of a burst. *GRB Coordinates Network*, 6489:1–+. [ADS].

[Pagani et al., 2007b] Pagani, C., Markwardt, C. B., Evans, P., Gavriil, F., Kennea, J. A., Falcone, A. D., Landsman, W., and Marshall, F. E. (2007b). SWIFT J195509.6+261406 / GRB 070610: Swift continued observations. *GRB Coordinates Network*, 6520:1–+. [ADS].

[Panaitescu, 2007a] Panaitescu, A. (2007a). Jet breaks in the X-ray light-curves of Swift gamma-ray burst afterglows. MNRAS, 380:374–380. [ADS].

[Panaitescu, 2007b] Panaitescu, A. (2007b). Swift gamma-ray burst afterglows and the forward-shock model. MNRAS, 379:331–342. [ADS].

[Panaitescu and Kumar, 2000] Panaitescu, A. and Kumar, P. (2000). Analytic Light Curves of Gamma-Ray Burst Afterglows: Homogeneous versus Wind External Media. ApJ, 543:66–76. [ADS].

[Panaitescu et al., 2006] Panaitescu, A., Mészáros, P., Burrows, D., Nousek, J., Gehrels, N., O'Brien, P., and Willingale, R. (2006). Evidence for chromatic X-ray light-curve breaks in Swift gamma-ray burst afterglows and their theoretical implications. MNRAS, 369:2059–2064. [ADS].

[Perkin-Elmer, 1997] Perkin-Elmer (1997). *Single Photon Counting Module, SPCM-AQ Series*. Laser Components GmbH, Werner-von-Siemens-Str. 15, D-82140 Olching.

[Racusin et al., 2006] Racusin, J., Grupe, D., Hunsberger, S., and Gehrels, N. (2006). GRB 060901: Swift/XRT position. *GRB Coordinates Network*, 5494:1–+. [ADS].

[Racusin et al., 2008] Racusin, J. L., Karpov, S. V., Sokolowski, M., Granot, J., Wu, X. F., Pal'Shin, V., Covino, S., van der Horst, A. J., Oates, S. R., Schady, P., Smith, R. J., Cummings, J., Starling, R. L. C., Piotrowski, L. W., Zhang, B., Evans, P. A., Holland, S. T., Malek, K., Page, M. T., Vetere, L., Margutti, R., Guidorzi, C., Kamble, A. P.,

Curran, P. A., Beardmore, A., Kouveliotou, C., Mankiewicz, L., Melandri, A., O'Brien, P. T., Page, K. L., Piran, T., Tanvir, N. R., Wrochna, G., Aptekar, R. L., Barthelmy, S., Bartolini, C., Beskin, G. M., Bondar, S., Bremer, M., Campana, S., Castro-Tirado, A., Cucchiara, A., Cwiok, M., D'Avanzo, P., D'Elia, V., Della Valle, M., de Ugarte Postigo, A., Dominik, W., Falcone, A., Fiore, F., Fox, D. B., Frederiks, D. D., Fruchter, A. S., Fugazza, D., Garrett, M. A., Gehrels, N., Golenetskii, S., Gomboc, A., Gorosabel, J., Greco, G., Guarnieri, A., Immler, S., Jelinek, M., Kasprowicz, G., La Parola, V., Levan, A. J., Mangano, V., Mazets, E. P., Molinari, E., Moretti, A., Nawrocki, K., Oleynik, P. P., Osborne, J. P., Pagani, C., Pandey, S. B., Paragi, Z., Perri, M., Piccioni, A., Ramirez-Ruiz, E., Roming, P. W. A., Steele, I. A., Strom, R. G., Testa, V., Tosti, G., Ulanov, M. V., Wiersema, K., Wijers, R. A. M. J., Winters, J. M., Zarnecki, A. F., Zerbi, F., Mészáros, P., Chincarini, G., and Burrows, D. N. (2008). Broadband observations of the naked-eye γ-ray burst GRB080319B. Nature, 455:183–188. [ADS].

[Remillard et al., 2000] Remillard, R., Morgan, E., Smith, D., and Smith, E. (2000). XTE J1118+480. IAU Circ., 7389:2–+. [ADS].

[Roming et al., 2006] Roming, P. W. A., Schady, P., Fox, D. B., Zhang, B., Liang, E., Mason, K. O., Rol, E., Burrows, D. N., Blustin, A. J., Boyd, P. T., Brown, P., Holland, S. T., McGowan, K., Landsman, W. B., Page, K. L., Rhoads, J. E., Rosen, S. R., Vanden Berk, D., Barthelmy, S. D., Breeveld, A. A., Cucchiara, A., De Pasquale, M., Fenimore, E. E., Gehrels, N., Gronwall, C., Grupe, D., Goad, M. R., Ivanushkina, M., James, C., Kennea, J. A., Kobayashi, S., Mangano, V., Mészáros, P., Morgan, A. N., Nousek, J. A., Osborne, J. P., Palmer, D. M., Poole, T., Still, M. D., Tagliaferri, G., and Zane, S. (2006). Very Early Optical Afterglows of Gamma-Ray Bursts: Evidence for Relative Paucity of Detection. ApJ, 652:1416–1422. [ADS].

[Scargle, 1982] Scargle, J. D. (1982). Studies in astronomical time series analysis. II - Statistical aspects of spectral analysis of unevenly spaced data. ApJ, 263:835–853. [ADS].

[Schlegel et al., 1998] Schlegel, D. J., Finkbeiner, D. P., and Davis, M. (1998). Maps of Dust Infrared Emission for Use in Estimation of Reddening and Cosmic Microwave Background Radiation Foregrounds. ApJ, 500:525–+. [ADS].

[Słowikowska et al., 2009] Słowikowska, A., Kanbach, G., Kramer, M., and Stefanescu, A. (2009). Optical polarization of the Crab pulsar: precision measurements and comparison to the radio emission. MNRAS, 397:103–123. [ADS].

[Smith and Mundell, 2009] Smith, R. J. and Mundell, C. G. (2009). GRB 090727: Liverpool telescope possible OT candidate. *GRB Coordinates Network*, 9719:1–+. [ADS].

[Smith et al., 2009] Smith, R. J., Mundell, C. G., Steele, I. A., Melandri, A., Kobayashi, S., Mottram, C. J., Bersier, D. F., Cano, Z., Gomboc, A., and Guidorzi, C. (2009). GRB 090727: Liverpool telescope afterglow confirmation and optical flare. *GRB Coordinates Network*, 9722:1–+. [ADS].

[Sparks and Axon, 1999] Sparks, W. B. and Axon, D. J. (1999). Panoramic Polarimetry Data Analysis. PASP, 111:1298–1315. [ADS].

[Spruit and Kanbach, 2002] Spruit, H. C. and Kanbach, G. (2002). Correlated X-ray and optical variability in KV UMa. A&A, 391:225–233. [ADS].

[Staelin and Reifenstein, 1968] Staelin, D. H. and Reifenstein, III, E. C. (1968). Pulsating Radio Sources near the Crab Nebula. *Science*, 162:1481–1483. [ADS].

[Stanek and Garnavich, 1998] Stanek, K. Z. and Garnavich, P. M. (1998). Red Clump Stars - New, Improved Distance Indicator. In *Bulletin of the American Astronomical Society*, volume 30 of *Bulletin of the American Astronomical Society*, pages 1409–+. [ADS].

[Stebbins, 1910] Stebbins, J. (1910). The measurement of the light of stars with a selenium photometer, with an application to the variations of Algol. ApJ, 32:185–214. [ADS].

[Stefanescu et al., 2008a] Stefanescu, A., Kanbach, G., Słowikowska, A., Duscha, S., and Mühlegger, M. (2008a). OPTIMA-Burst: Observing GRB Afterglows and other Fast Transients with High Time Resolution. In D. Phelan, O. Ryan, & A. Shearer, editor, *High Time Resolution Astrophysics: The Universe at Sub-Second Timescales*, volume 984 of *American Institute of Physics Conference Series*, pages 124–131. [ADS].

[Stefanescu et al., 2008b] Stefanescu, A., Kanbach, G., Słowikowska, A., Greiner, J., McBreen, S., and Sala, G. (2008b). Very fast optical flaring from a possible new Galactic magnetar. Nature, 455:503–505. [ADS].

[Stefanescu et al., 2007a] Stefanescu, A., Słowikowska, A., Kanbach, G., Duscha, S., Schrey, F., Steinle, H., and Ioannou, Z. (2007a). GRB 070610: OPTIMA-burst detection of continued strong flaring activity. *GRB Coordinates Network*, 6508:1–+. [ADS].

[Stefanescu et al., 2007b] Stefanescu, A., Słowikowska, A., Kanbach, G., Duscha, S., Schrey, F., Steinle, H., and Ioannou, Z. (2007b). GRB 070610: OPTIMA-burst high-time-resolution optical observations. *GRB Coordinates Network*, 6492:1–+. [ADS].

[Straubmeier, 2001] Straubmeier, C. (2001). *OPTIMA - Entwicklung und erste astronomische Messungen eines optischen Hochgeschwindigkeitsphotometers*. PhD thesis, Technische Universität München.

[Straubmeier et al., 2001] Straubmeier, C., Kanbach, G., and Schrey, F. (2001). OPTIMA: A Photon Counting High-Speed Photometer. *Experimental Astronomy*, 11:157–170. [ADS].

[Trümper et al., 2010] Trümper, J. E., Zezas, A., Ertan, Ü., and Kylafis, N. D. (2010). The energy spectrum of anomalous X-ray pulsars and soft gamma-ray repeaters. A&A, 518:A46+. [ADS].

[Uemura et al., 2004] Uemura, M., Kato, T., Ishioka, R., Imada, A., Nogami, D., Monard, B., Cook, L. M., Stubbings, R., Kiyota, S., Nelson, P., Beninger, J.-Y., Bolt, G., and Heathcote, B. (2004). Optical Observation of the 2003 Outburst of a Black Hole X-Ray Binary, V4641 Sagittarii. PASJ, 56:823–829. [ADS].

[Uemura et al., 2002] Uemura, M., Kato, T., Watanabe, T., Stubbings, R., Monard, B., and Kawai, N. (2002). The 1999 Optical Outburst of the Fast X-Ray Nova, V4641 Sagittarii. PASJ, 54:95–101. [ADS].

[Uemura et al., 2005] Uemura, M., Mennickent, R., Stubbings, R., Bolt, G., Monard, B., Cook, L. M., Williams, P., Ishioka, R., Imada, A., Kato, T., Nogami, D., Starkey, D., Maehara, H., Nakajima, K., Meszaros, S., Szekely, P., Kiss, L. L., Lindstrom, C., and

Griffin, J. (2005). Outburst of a Black Hole X-ray Binary V4641 Sgr in 2004 July. *Information Bulletin on Variable Stars*, 5626:1–+. [ADS].

[Šimon et al., 2010] Šimon, V., Polášek, C., Jelínek, M., Hudec, R., and Trobl, J. Å. (2010). Complicated variations in the early optical afterglow of GRB 090726. A&A, 510:A49+. [ADS].

[Verhoeve et al., 2006] Verhoeve, P., Martin, D. D. E., Hijmering, R. A., Verveer, J., van Dordrecht, A., Sirbi, G., Oosterbroek, T., and Peacock, A. (2006). S-Cam 3: Optical astronomy with a STJ-based imaging spectrophotometer. *Nuclear Instruments and Methods in Physics Research A*, 559:598–601. [ADS].

[Vestrand et al., 2005] Vestrand, W. T., Wozniak, P. R., Wren, J. A., Fenimore, E. E., Sakamoto, T., White, R. R., Casperson, D., Davis, H., Evans, S., Galassi, M., McGowan, K. E., Schier, J. A., Asa, J. W., Barthelmy, S. D., Cummings, J. R., Gehrels, N., Hullinger, D., Krimm, H. A., Markwardt, C. B., McLean, K., Palmer, D., Parsons, A., and Tueller, J. (2005). A link between prompt optical and prompt γ-ray emission in γ-ray bursts. Nature, 435:178–180. [ADS].

[Vogel, 1890] Vogel, H. C. (1890). Spectrographische Beobachtungen an Algol. *Astronomische Nachrichten*, 123:289–+. [ADS].

[Volnova et al., 2009] Volnova, A., Pavlenko, E., Sklyanov, A., Antoniuk, O., and Pozanenko, A. (2009). GRB 090726: optical observation. *GRB Coordinates Network*, 9741:1–+. [ADS].

[Wagner et al., 2001] Wagner, R. M., Foltz, C. B., Shahbaz, T., Casares, J., Charles, P. A., Starrfield, S. G., and Hewett, P. (2001). The Halo Black Hole X-Ray Transient XTE J1118+480. ApJ, 556:42–46. [ADS].

[Young, 1994] Young, A. T. (1994). Air mass and refraction. Appl. Opt., 33:1108–1110. [ADS].

[Zacharias et al., 2004] Zacharias, N., Urban, S. E., Zacharias, M. I., Wycoff, G. L., Hall, D. M., Monet, D. G., and Rafferty, T. J. (2004). The Second US Naval Observatory CCD Astrograph Catalog (UCAC2). AJ, 127:3043–3059. [ADS].

Acknowledgements

As usual, this work would not have been possible without the help and support of a great many people. First and foremost, I wish to express my gratitude to *Jochen Greiner* and his fine group for creating a great place to work and be creative and for welcoming me into the fold.

Without the unending supply of great ideas of my supervisor *Gottfried Kanbach*, this thesis would not have been possible. When everybody told me my idea to build this kind of instrument will never work, Gottfried was the one to tell me it surely will – as he had the very same plan. I know that if he had not kept faith in our idea in the beginning, and in me in the end, I would never have finished this thesis.

All great ideas come to nothing when there's no one around like *Fritz Schrey*, who can see through all the fluff and can just build the stuff. Whenever one of us had another crazy idea, he was the one who made it reality, sometimes by reminding us what will and won't work.

The diploma-students I supervised, *Martin Mühlegger* and *Sven Duscha* not only helped me with my thesis by doing an excellent job with theirs, but they also became really good friends (or even better friends than they were before) in the process.

During my stay at the MPE, I think I never learned so much so quickly as in the months following the discovery of SWIFT J1955. Special thanks go out to *Sheila McBreen* and *Gloria Sala*, who taught me so much about X-ray data analysis and interpretation. Whenever I felt overwhelmed by the task of writing a high-profile paper, they were the ones that nudged me on and kept me pointed in the right direction.

Without the group of *Jannis Papamastorakis* on Crete, the OPTIMA-Burst project would not have been possible. In particular *Tassos Kougentakis* and *Georgios Paterakis*, the heart and soul of all things technical at SKO deserve praise. They not only keep the place running, they keep it alive. Also *Anton Strigachev* and *Evgenii Semkov* who spend three months in a row on a remote mountaintop, year after year, in photometric nights and in thunderstorms, have my gratitude. For all their sometimes grumpiness, they are always great chums.

Speaking of chums, this section cannot be complete without the mention of all the other PhD students in the Gamma group, first and foremost *Karsten Kretschmer*, *Robert Andritschke* and *Christian "Clemi" Clemens*. Never was geeking out so much fun as with you guys at the Vintage Computer Festival, or at late-time movie nights.

Finally, I'd like to yell out a big thank you to all my friends, my parents *Andrei* and *Lena* and to my lovely wife *Mirjam*. Your love and patience kept me going through the years. I love you!